The suitability of Ni-Co catalysts in the dry reforming reaction

By

Bongani Leslie Mtetwa

BSc (Hons) Eng. Chemical Engineering, University of Cape Town (2017)

Dissertation submitted to the University of Cape Town
in partial fulfilment of the requirements
for the degree of

Master of Science in Engineering

Centre for Catalysis Research
Department of Chemical Engineering
University of Cape Town
South Africa

August 2021

“Unless the Lord builds the house, the builders labour in vain. Unless the Lord watches over the city, the guards stand watch in vain.”

Psalms 127:1 (NIV)

Declaration

I know the meaning of plagiarism and declare that all the work in the document, save for that which is properly acknowledged, is my own. This thesis/dissertation has been submitted to the Turnitin module (or equivalent similarity and originality checking software) and I confirm that my supervisor has seen my report and any concerns revealed by such have been resolved with my supervisor.

Signature: Signed by candidate

Acknowledgements

Firstly, I would like to thank my supervisors, Professor Michael Claeys and Associate Professor Nico Fischer for giving me the opportunity to further my studies under their supervision. Their support, guidance and advice were invaluable during this project. A special thanks goes to Professor Michael Claeys for always availing himself to answer any questions that I had working on this project.

Many thanks go to the National Research Foundation (NRF) for awarding me with the Innovation Masters scholarship, UCT for awarding me the International Students scholarship and the DSI-NRF Centre of Excellence in Catalysis (c*change) for their financial support throughout this project.

I would like to thank Dr Mohamed Fadlalla for his help in carrying out the H_2-TPR, BET analysis, Miranda Waldron for carrying out Raman spectroscopy as well as Mohamed Jaffer and Nasheeta Hanief for the TEM analysis. Special thanks also go to Professor Patricia Kooyman for carrying out HR-STEM analysis carried out at Nelson Mandela University (NMU). I would also like to thank Imaad Davies, for his assistance and insights during the thermodynamic analysis as well as Farhana Allie who I had the pleasure of working with as a vacation student when I was still synthesising catalysts for the study. Lastly, I would like to thank the Analytical laboratory staff for carrying out ICP-OES analysis.

I would also like to thank everyone in the Catalysis Institute as well as all the members of our research group for their support during my studies. Special thanks go to Wijnand, Shaine, Veroushia, Thulani, Danielle, Mohamed, and Dominic for all their help during my laboratory work.

I would also like to parents, Leslie, and Sarah Mtetwa for their unwavering support along with the rest of my family in Zimbabwe. I would also like to thank Mrs Louise De Koker, the late Dr Tadiwa Sunmore Chikwete, Mrs Effort Chikwete, my uncle Edgar Chikwete and his family, Malcolm, Tafadzwa, Naomi, Jono, Sibongile, Tita, Lesedi, Sinethemba, Khanyi, Tlaleng, Veroushia and Christopher for all their support and encouragement. And finally, I would like to thank God for providing me the strength and wisdom to see this project to its completion. Apart from Him, I can do nothing.

Synopsis

In recent times, the dry reforming of methane has received significant interest as an alternative process through which synthesis gas can be produced. This is because dry reforming combines methane and carbon dioxide which are both greenhouse gases into synthesis gas which is used in the production of synthetic fuels and chemicals. The main problem faced by the dry reforming reaction is the formation carbon which causes catalyst deactivation. Noble metal catalysts such as ruthenium and rhodium have shown great promise as dry reforming catalysts because of their resistance to carbon formation, but they are expensive making their use on an industrial scale unlikely. This has led to non-noble metals such as nickel and cobalt being considered as potential catalysts. Bimetallic nickel-cobalt (Ni-Co) catalysts have garnered a lot of interest as dry reforming catalysts as combining these two metals is believed to produce catalysts that would be more stable than monometallic nickel and cobalt catalysts.

The objectives of the project were to investigate the suitability of nickel-cobalt (Ni-Co) alloy catalysts with different compositions as well as monometallic nickel and cobalt catalysts as dry reforming catalysts. In doing so, special emphasis was placed on understanding the effect of the Ni-Co ratio on catalyst activity, stability, and deactivation mechanisms. In the study, seven catalysts with varying Ni-Co ratios were prepared. The catalysts had a 10 wt.% active metal (nickel and cobalt combined) loading and were supported on magnesium aluminate ($MgAl_2O_4$).

Catalyst testing was carried out on all the catalysts at 700 °C for a period of 12 hours to compare their performance in the dry reforming reaction. The results from catalyst testing showed that the Ni-Co catalysts that were nickel rich (70% and 90% nickel in terms of active metal) were the most active catalysts. This was because these catalysts achieved higher methane and carbon dioxide conversions in comparison to the rest of the catalysts. The most surprising result from catalyst testing was that the monometallic nickel catalyst showed very limited activity and was unstable.

Post run catalyst characterisation using Raman spectroscopy showed that the Ni-Co composition of the catalysts influenced the type of carbon deposited on the catalysts during catalyst testing. This was because the carbon deposits on the cobalt rich Ni-Co

catalysts were found to be more graphitic in nature compared to those on the nickel rich Ni-Co catalysts. However, the Ni-Co composition of the catalysts was found to have no influence on the amount of carbon deposited on the catalysts based on the results obtained from TGA analysis.

In addition, post run catalyst characterisation showed that there was carbon formation on all the catalysts studied except for the monometallic nickel catalyst. This showed that there is a need to investigate additional means through which the carbon formation can be limited during catalyst testing. The co-feeding of water in the dry reforming of methane is one such measure that should be investigated.

Contents

List of Figures

List of Tables

Nomenclature

°	Degree
°C	Degrees Celsius
2WNV	Two-way needle valve
3WV	Three-way valve
Å	Angstrom
A3WV	Three-way actuator valve
Al	Aluminium
$Al(NO_3)_3.9H_2O$	Aluminium nitrate nonahydrate
Al_2O_3	Alumina
Ar	Argon
BET	Brunauer-Emmett-Teller
CAPEX	Capital expenditure
CeO_2	Ceria
CH_4	Methane
CH_x	Dehydrogenated carbon species
CO	Carbon monoxide
$Co(NO_3)_2.6H_2O$	Cobalt nitrate hexahydrate
CO_2	Carbon dioxide
CO_3^{2-}	Carbonate
Co_3O_4	Cobalt (II, III) oxide
$CoTiO_3$	Cobalt titanite
DF	Dilution factor
DRM	Dry reforming of methane
DTG	Differential thermogravimetry
E_a	Activation energy
fcc	Face centred cubic
GC	Gas chromatogram
H	Magnetic field
H_2	Hydrogen
H_2/CO	Hydrogen to carbon monoxide ratio
H_2O	Water/Steam
H_2-TPR	Hydrogen temperature programmed reduction

HCO_2^-	Formate
HCO_3^-	Bicarbonate
HR-STEM	High-resolution scanning transmission electron microscopy
ICP-OES	Inductively coupled plasma optical emission spectrometry
K_a	Equilibrium constant
kV	Kilovolt
m	Metre
mA	Milliamp
mbar	Millibar
MFC	Mass flow controller
Mg	Magnesium
$Mg(NO_3)_2.6H_2O$	Magnesium nitrate hexahydrate
$MgAl_2O_4$	Magnesium aluminate
MgO	Magnesium oxide
$MgO\text{-}Al_2O_3$	Magnesium oxide modified alumina
min	Minute
mL	Millilitre
mm	Millimetres
M_{rem}	Remnant magnetisation
M_{sat}	Saturation magnetisation
MSI	metal support interactions
N_2	Nitrogen
N_2	Nitrogen
NH_4OH	Ammonia solution
$Ni(NO_3)_2.6H_2O$	Nickel nitrate hexahydrate
$NiAl_2O_4$	Nickel aluminate
Ni-Co	Nickel-Cobalt
Ni-Cu	Nickel-copper
Ni-Fe	Nickel-iron
Ni-Mn	Nickel-manganese
NiO	Nickel oxide
NiO-MgO	Nickel and magnesium oxide
O_2	Oxygen

Opex	Operating expenditure
OSC	Oxygen storage capacity
PXRD	Powder X-ray diffraction
rpm	Revolutions per minute
s	Seconds
SiC	Silicon carbide
SiO_2	Silica
SMR	Steam methane reforming
SMSI	Strong metal support interactions
T_C	Curie temperature
TCD	Thermal conductivity detector
TEM	Transmission electron microscopy
TGA	Thermogravimetric analysis
$T_{Hüttig}$	Hüttig temperature
TiO_2	Titania
$T_{melting}$	Melting temperature
TOF	Turnover frequency
T_{Tamman}	Tamman temperature
wt.%	Weight percent
ZrO_2	Zirconia
θ	Theta angle
λ	Wavelength
µm	Micrometre

1 Introduction

1.1 Background

Dry reforming is a process through which methane and carbon dioxide are reacted to produce synthesis gas (made up of carbon monoxide and hydrogen). The dry reforming process is especially attractive from an environmental standpoint. This is because it provides a way to convert two greenhouse gases, methane and carbon dioxide, into synthesis gas which is the feedstock to produce synthetic fuels through Fischer-Tropsch synthesis. Currently, synthesis gas production from methane is mostly carried out via partial oxidation and/or steam reforming rather than through dry reforming. This is mainly because dry reforming catalysts tend to suffer from deactivation caused by coke formation which makes them less stable in comparison to the catalysts used in alternative processes.

1.2 Context

A variety of noble and non-noble metals have been considered as catalysts for the dry reforming process. In general, noble metal catalysts such as platinum, ruthenium, rhodium, and palladium have been found to be suitable for the process in comparison to non-noble metal catalysts. This is because they display higher catalytic activity and resistance to coke formation (Aramouni *et al.*, 2018). However, implementing these catalysts industrially may not be feasible due to their high cost and limited availability (Aramouni *et al.*, 2018). This has led to the consideration of non-noble metals such as nickel and cobalt as they are cheaper and are more available. Bimetallic catalysts, especially nickel-cobalt bimetallic alloys have been determined to be promising catalysts in the dry reforming process due to their high resistance to coke formation (Abdullah *et al.*, 2017).

1.3 Scope of project

In this project a variety of nickel-cobalt (Ni-Co) alloy catalysts with different compositions as well as monometallic nickel and cobalt catalysts were investigated for their suitability as dry reforming catalysts. Emphasis was placed on understanding the effect of the Ni-Co ratio on catalyst stability and deactivation mechanisms.

1.4 Overall objectives

The overall objectives of this project were to gain new insights about the behaviour of nickel-cobalt alloy catalysts as well as monometallic cobalt and nickel catalysts during dry reforming. The threshold conditions for stable operation for these catalysts was also determined.

2 Literature review

2.1 Dry reforming of methane

2.1.1 Overview

Dry reforming of methane (DRM) is a process through which methane (CH_4) and carbon dioxide (CO_2) are combined to produce synthesis gas which is made up of carbon monoxide (CO) and hydrogen (H_2) (San-José-Alonso *et al.*, 2009). The dry reforming of methane follows Equation (2.1).

$$\boldsymbol{CH_4 + CO_2 \rightleftharpoons 2CO + 2H_2} \quad (\Delta \boldsymbol{H_{298K} = +247\ kJ/mol}) \qquad \text{Equation (2.1)}$$

The dry reforming reaction is an endothermic reaction ($\Delta H_{rxn}>0$), thus it is favoured at high temperatures (Aramouni *et al.*, 2018). According to Aramouni *et al.* (2018), the optimum reaction temperatures lies between 627–1000 °C as these high temperatures allow higher conversions to be achieved. In terms of pressure, the reaction is favourable at low pressures. This is because the forward reaction will lead to the formation of more moles of gas, so it will be favoured according to Le Chatelier's principle.

DRM is also attractive from an environmental standpoint. This is because it provides a way to convert two greenhouse gases into synthesis gas which is valuable industrially (Luisetto *et al.*, 2012). Synthesis gas is utilised as a feedstock in a variety of processes such as ammonia synthesis, methanol production as well as liquid fuel production using Fischer-Tropsch synthesis (Ay & Üner, 2015). Additionally, dry reforming also offers a pathway to potentially utilise biogas (mainly composed of CO_2 and CH_4) that is cost effective. This is because the need for complicated and expensive separation processes that are associated with the current methods of reforming would be eliminated (Ay & Üner, 2015).

2.1.2 Alternative methane reforming processes

The main alternative methane reforming processes to produce synthesis gas are steam reforming (Equation (2.2)), partial oxidation (Equation (2.3)) and autothermal reforming. The main difference in these reforming processes is the oxidant that is used. Steam (H_2O) and oxygen (O_2) are the oxidants in steam reforming and partial

oxidation respectively whilst in autothermal reforming both oxidants are utilised. This is because autothermal reforming combines steam reforming and partial oxidation in the production of synthesis gas. An overview of these individual reforming processes is provided in Table 2.1.

$$\boldsymbol{CH_4 + H_2O \rightleftharpoons CO + 3H_2 \quad (\Delta H_{298K} = +225\ kJ/mol)}$$ Equation (2.2)

$$\boldsymbol{CH_4 + \frac{1}{2}O_2 \rightleftharpoons CO + 2H_2 \quad (\Delta H_{298K} = -225.4\ kJ/mol)}$$ Equation (2.3)

Table 2.1: Overview of the main alternative methane reforming processes to DRM. Adapted from the review articles of Abdullah et al. (2017) and Abdulrasheed et al. (2019)

Method of methane reforming	Advantages	Disadvantages	H_2/CO ratio	Operating conditions
Steam reforming	1. High H_2 concentration in product 2. Industrially mature	1. High emissions of CO_2 associated with steam generation 2. Sensitive to methane quality (i.e., desulphurization required)	3:1	P: 3 – 25 atm T: 700 – 1000 °C CH_4:H_2O: 1:1
Partial oxidation	1. Less sensitive to methane quality (i.e., sulphur impurities can be tolerated) 2. Residence time is short	1. Expensive because pure oxygen is required meaning a cryogenic separation unit is needed 2. Risk of explosion from CH_4/O_2 mixture 3. Possibility of hotspots on the catalyst as reaction is exothermic	2:1	P: 100 atm T: 950 – 1000 °C CH_4:O_2: 1:1
Autothermal reforming	1. Flexible as feed composition can be varied. 2. Combining steam reforming and partial oxidation conserves energy	1. Hydrogen yield is lower 2. Increasing H_2O:O_2 ratio limits the reaction	Varies	Varies depending on feed

2.1.3 Current commercial DRM processes

The commercial implementation of DRM has only recently been realised (Wittich *et al.*, 2020). One of these processes that is now commercially available arose from a collaboration between Linde and BASF (Linde, 2019). In this collaboration, Linde designed the process whilst BASF designed the catalyst used in the process. The commercial names for the process and catalyst are DRYREF™ and SYNSPIRE™ G-110, respectively. A schematic of the DRYREF™ process is available in Figure 2.1. From the schematic it can be seen the DRYREF™ process is similar to conventional steam reforming processes with the main difference being that it uses CO_2 alongside H_2O as the oxidants in the reforming process. This difference leads to capital expenditure (CAPEX) and operating expenditure (OPEX) savings that make the DRYREF™ process commercially attractive. From a CAPEX standpoint, the use of CO_2 is beneficial in that it makes the units responsible for CO_2 recycling and removal smaller (Linde, 2019). This is because the amount of CO_2 that is processed in these units is reduced through its use during reforming. In terms of OPEX, the use of CO_2 in reforming leads to significant savings due to the reduction in the usage of steam. This is because steam generation is energy intensive making it expensive. The lowering of the steam requirements of the process could also lead to reduction in the CAPEX of the process if the size of the units used in steam generation are reduced. Lastly, the use of CO_2 in the reforming process is attractive in that it provides the process with flexibility to alter the H_2/CO ratio achieved by the process and also provides an opportunity to reduce the carbon footprint of the process if CO_2 imports are utilised.

The aforementioned benefits are a in large part able to be realised because of the SYNSPIRE™ G-110 catalyst. The catalyst is comprised of nickel oxides supported on metal oxide carriers (Linde, 2019). The metal oxide carriers are reported to have the ability to react with carbon deposits thereby creating a self-cleaning mechanism. This limits the carbon that can be deposited on the catalyst which ensures that it can retain its stability in the dryer conditions brought about by using CO_2 in reforming. Carbon deposition is more significant in dryer reforming conditions. The exact mechanisms through which the catalyst maintains its stability are unknown due to the commercial nature of the catalyst.

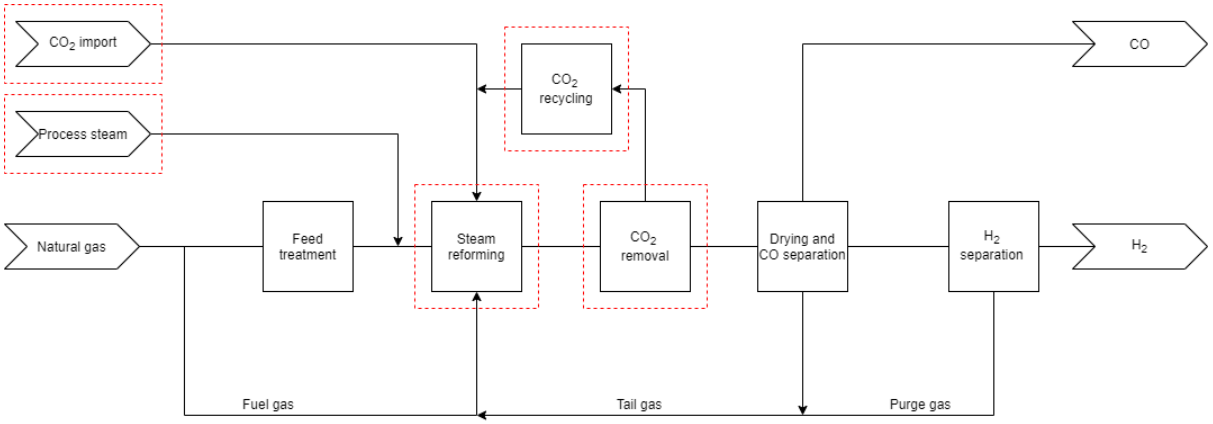

Figure 2.1: Schematic of the DRYREF™ process designed by Linde. The red dotted lines highlight the areas of innovation in the process. Adapted from Linde (2019)

Haldor Topsøe also has a commercially available reforming process called ReShift™ which utilises CO_2 during reforming (Mortensen *et al.*, 2020). A schematic of the ReShift™ process is available in Figure 2.2. The ReShift™ technology differs from other reforming processes in that it includes an additional unit called the adiabatic post converter (APOC) which facilitates the addition of CO_2 into the process. The APOC utilises the high temperature of the gas exiting steam reforming (e.g., above 900 °C) to ensure that the limits for carbon formation at a lower steam/carbon resulting from the addition of CO_2 are not approached when the temperature drops because of the adiabatic reaction. The ReShift™ technology can be utilised by either building a new plant based on the technology or retrofitting it to existing steam methane reforming (SMR) plants. When the ReShift™ technology is utilised on a new plant, the size of the SMR reformer can be reduced by up to 30% whilst CO_2 emissions can be reduced by up to 10% compared to a conventional SMR plant producing the same amount of synthesis gas product (Mortensen *et al.*, 2020). Mortensen *et al.* (2020) also reported that when the ReShift™ technology is retrofitted to an existing plant without altering the SMR process, net CO_2 emissions could be reduced by up to 80% whilst the CO product can be increased by up to 40%. These benefits all arise from the addition of CO_2 to the process.

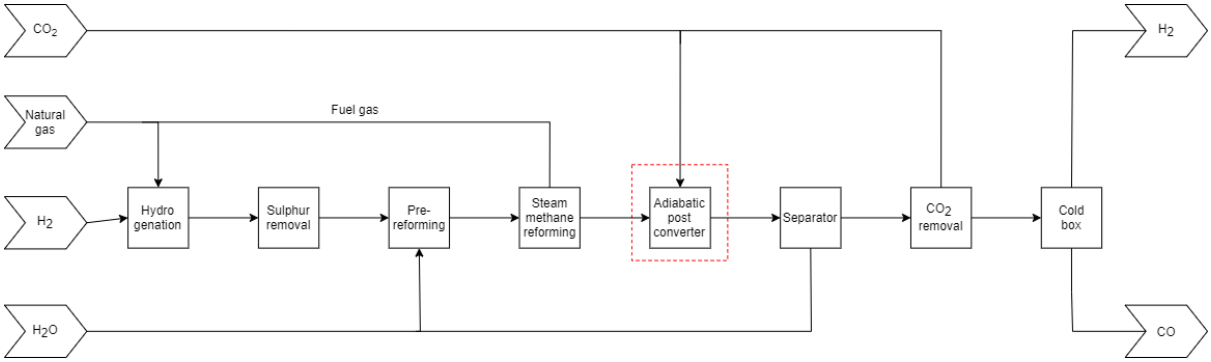

Figure 2.2: Schematic of the ReShift™ process designed by Haldor Topsøe. The red dotted lines highlight the innovation in the process. Adapted from Mortensen et al. (2020)

Commercial processes such as DRYREF™ and Reshift™ show that the use of CO_2 in reforming processes is promising. However, it must be noted that these processes do not implement DRM in the strictest sense because they use steam as an additional oxidant which improves the stability of the catalysts in the processes. This shows that the cofeeding of water will continue to be necessary in DRM to make it commercially viable until catalysts that are stable in pure DRM conditions are developed.

2.2 Thermodynamics

Several thermodynamic equilibrium analyses carried out to better understand the DRM point to two main approaches being utilised to determine the equilibrium concentration of compounds. These are; the use of equilibrium constants (K_a) of reactions and the minimisation of the Gibbs free energy (Istadi *et al.*, 2005). When the equilibrium constant approach is used, a set of reactions that will be considered is first chosen. Afterwards, individual K_a's are calculated for each of these reactions and the equilibrium concentrations of the compounds considered in the reactions are then calculated based on them. A flaw to this approach is that the equilibrium calculated is limited by the reactions considered. The Gibbs free energy minimisation approach differs from the equilibrium constant approach in that it calculates equilibrium based on a system made up of compounds rather than reactions. In this approach, equilibrium is calculated by minimising the sum of the Gibbs free energies of the individual compounds chosen as part of the system. An elemental balance of the compounds in the system is included in the calculations to ensure that the mass balance before and after the equilibrium calculations is maintained (Aramouni *et al.*, 2017). Most of the papers considered in the section to follow utilised the Gibbs free energy approach. Those that used an alternative approach will be highlighted.

2.2.1 Feasible reactions

According to Zhang *et al.* (2007), the dry reforming of methane is not spontaneous below 633 °C at 1 atm. This is because the reaction is highly endothermic and will be favoured at high temperatures. Zhang *et al.* (2007) went on to suggest that the main side reactions that occur alongside dry reforming are the reverse water gas shift (RWGS) reaction (Equation (2.4)), methane decomposition (Equation (2.5)), the Boudouard reaction (Equation (2.6)) and the reverse gasification of carbon reaction (Equation (2.7)).

$$\boldsymbol{H_2 + CO_2 \rightleftharpoons CO + H_2O} \quad (\Delta \boldsymbol{H_{298K} = +41\ kJ/mol}) \qquad \text{Equation (2.4)}$$

$$\boldsymbol{CH_4 \rightleftharpoons C + 2H_2} \quad (\Delta \boldsymbol{H_{298K} = +75\ kJ/mol}) \qquad \text{Equation (2.5)}$$

$$\boldsymbol{2CO \rightleftharpoons C + CO_2} \quad (\Delta \boldsymbol{H_{298K} = -171\ kJ/mol}) \qquad \text{Equation (2.6)}$$

$$\boldsymbol{CO + H_2 \rightleftharpoons C + H_2O} \quad (\Delta \boldsymbol{H_{298K} = -131\ kJ/mol}) \qquad \text{Equation (2.7)}$$

Furthermore, Zhang *et al.* (2007) also carried out calculations to determine how the equilibrium constants (K_a's) of the individual reactions are affected by temperature. The results of these calculations are given in Figure 2.3. Since the equilibrium conversion for a reaction increases as K_a increases, the K_a values are a good indicator to determine which reaction is most likely to dominate at a given temperature. From Figure 2.3, it can be deduced that the exothermic reactions i.e., the Boudouard and the reverse gasification of carbon reaction are favoured at lower temperatures (below 600 °C). Conversely, the endothermic reactions i.e., DRM, RWGS and methane decomposition are favoured at higher temperatures (above 700 °C). The interplay between the DRM and methane decomposition reactions between 600 to 700 °C is particularly of interest when deciding the temperature to carry out catalyst testing. This is because neither reaction is likely to be significantly favoured over the other because the K_a values for the reactions are similar. Based on this, DRM should ideally be carried out above 700 °C. This is because above 700 °C the equilibrium conversion achievable for DRM would be significantly higher in comparison to those of the

competing side reactions such as methane decomposition and the RWGS can achieve. However, the temperature chosen must not be too high. A balance must be struck between favouring the DRM reaction, minimising the impact of side reactions, and operating at temperatures that would be industrially competitive.

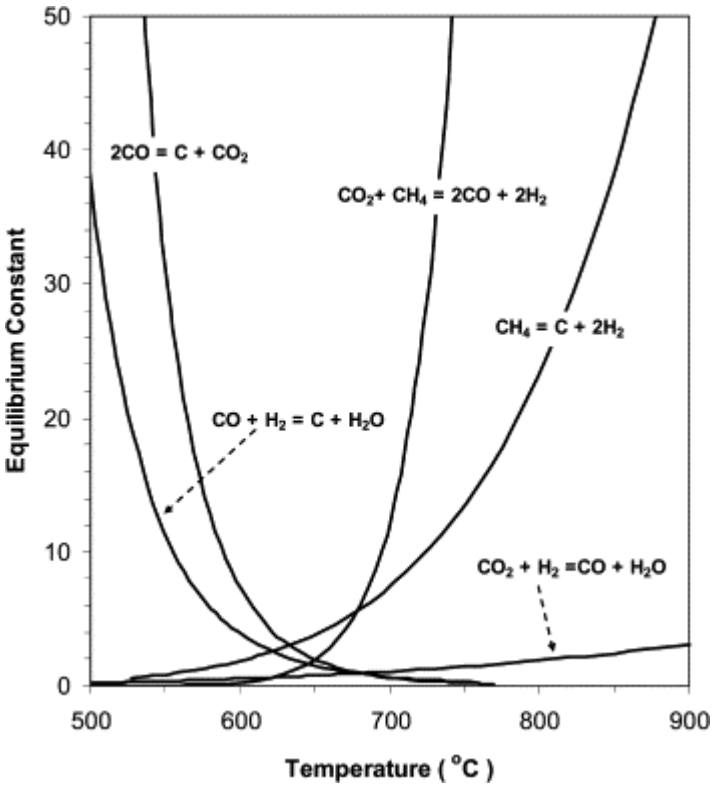

Figure 2.3: Equilibrium constants of the DRM reaction and the side reactions that occur alongside it as a function of temperature [from Zhang et al. (2007)]

The work done by Zhang *et al.* (2007), was also supported by the findings of Wang *et al.* (1996) and Nikoo & Amin (2011). By using standard free energy change calculations for individual reactions, Wang *et al.* (1996) determined the minimum feasible operating temperatures for DRM and methane decomposition to be 640 °C and 557 °C respectively. Additionally, the maximum feasible operating temperatures for the Boudouard and RWGS reactions were determined to be 700 °C and 820 °C respectively. Apart from the results for the RWGS reaction, all the limits presented in the study are in agreement with the findings of Zhang *et al.* (2007). This is because according to Zhang *et al.* (2007), the K_a value for the RWGS reaction would still be increasing at 820 °C which would imply that the reaction would still be feasible above the temperature limit set by Wang *et al.* (1996). Nikoo & Amin (2011) also carried out a study similar to that of Zhang *et al.* (2007). The major difference between the studies

was that Nikoo & Amin (2011) considered the possibility of the methanation reactions occurring which are given in Equations (2.8) and (2.9). The impact of these reactions under the conditions where dry reforming occurs was found to be minimal. This is because they are unlikely to be favoured at high temperatures as they are exothermic reactions. Therefore, the findings of Nikoo & Amin (2011) and Zhang *et al.* (2007) regarding which side reactions are likely ended up being similar.

$$\boldsymbol{CO_2 + 4H_2 \rightleftharpoons CH_4 + 2H_2O} \quad (\Delta \boldsymbol{H_{298K}} = \boldsymbol{-165\ kJ/mol}) \qquad \text{Equation (2.8)}$$

$$\boldsymbol{CO + 3H_2 \rightleftharpoons CH_4 + H_2O} \quad (\Delta \boldsymbol{H_{298K}} = \boldsymbol{-206\ kJ/mol}) \qquad \text{Equation (2.9)}$$

2.2.2 Effect of temperature

In DRM the equilibrium conversions of CO_2 and CH_4 both increase with increasing temperature (Nikoo & Amin, 2011). This phenomenon occurs because the DRM reaction that primarily consumes both these reactants is endothermic. Additionally, the RWGS and methane decomposition reactions which also consume the same reactants are also endothermic. This provides further support for the observed trends. However, disagreements exist about which of the two compounds achieves a higher equilibrium conversion in dry reforming. For example, a study carried out by Nikoo & Amin (2011) reported that the equilibrium conversion of CH_4 was higher than that of CO_2 whilst Bradford & Vannice (1999) reported the opposite. Nikoo & Amin (2011) attributed the higher CH_4 conversion achieved to be a result of the methane decomposition reaction having a more pronounced effect than the RWGS reaction in their equilibrium calculations. On the other hand, Bradford & Vannice (1999) put forward the occurrence of the RWGS reaction as the reason why their calculations found the CO_2 equilibrium conversion to be higher. In general, the RWGS and methane decomposition reactions play a significant role in determining whether the CH_4 or CO_2 conversion is higher in dry reforming.

2.2.3 Effect of pressure

The CH_4 and CO_2 conversions were found to decrease when pressure is increased at constant temperature. This is in line with Le Chatelier's principle because higher pressure would lead to the reverse of the dry reforming reaction in which they are

primarily consumed being favoured (Aramouni *et al.*, 2017). The work carried out by Wang *et al.* (1996) and Nikoo & Amin (2011) also supported these findings. Additionally, Nikoo & Amin (2011) determined that increasing the pressure at a constant temperature resulted in higher amounts of carbon formed. The increase in carbon formation observed was attributed to the Boudouard reaction rather than the decomposition of methane. This is because a study carried out by Shamsi & Johnson (2003) found that carbon formation through methane decomposition decreases with increasing pressure whilst the opposite was true for the Boudouard reaction. These findings are in agreement with the Le Chatelier's principle. In general, the highest CH_4 and CO_2 conversions are achieved at high temperature and low pressure (Aramouni *et al.*, 2017).

2.2.4 Effect of feed gas ratio

Varying the CO_2/CH_4 ratio in the feed was also found to influence the CO_2 and CH_4 conversions as well as the concentration of compounds at equilibrium. For example, having a feed gas ratio of $CO_2/CH_4 > 1$ (excess CO_2) at constant temperature was found to increase the CH_4 conversion (Nikoo & Amin, 2011). This result is plausible because CH_4 will be the limiting reagent in the system. Having excess CO_2 in the feed was also determined to reduce the amount of carbon formed with increasing temperature (Nikoo & Amin, 2011). This was because the methane decomposition reaction which is the primary cause of carbon deposition at higher temperatures was suppressed by having less CH_4 in the feed. Additionally, the Boudouard and hydrogenation of CO and CO_2 reactions which become the primary causes of carbon deposition under conditions of excess CO_2 are exothermic reactions. This means that their contribution to carbon deposition decreases as the temperature becomes higher which further supports the findings. Finally, having excess CO_2 in the feed was also determined to increase the amount of water formed during dry reforming above 1000 K. This is because having excess CO_2 available increases the likelihood of the RWGS reaction occurring.

The effects of having a feed gas ratio of $CO_2/CH_4 < 1$ (excess CH_4) were found to be the opposite of having excess CO_2. For example, decreasing the CO_2/CH_4 ratio in the feed at a constant temperature led to a decrease in the equilibrium conversion of CO_2

(Nikoo & Amin, 2011). This is because CO_2 conversion becomes lower when it is in excess. Additionally, the amount of carbon formed was found to increase with increasing temperature when CH_4 was in excess (Nikoo & Amin, 2011). This is because methane decomposition occurs without much hinderance when CH_4 is in excess. Lastly, despite more H_2 being formed via the methane decomposition reaction when CH_4 was in excess, less water was formed as the CO_2/CH_4 ratio was decreased. This is because CO_2 becomes a limiting reagent in the RWGS reaction when CH_4 is in excess.

2.2.5 H_2/CO ratio

The hydrogen to carbon monoxide ratio (H_2/CO) observed at equilibrium is often a good metric to determine the occurrence of side reactions during dry reforming. This is because the amounts of H_2 and CO at equilibrium are affected by the interplay of side reactions such as the Boudouard reaction, RWGS and methane decomposition. As such, the H_2/CO is generally used as a measure of selectivity in DRM. In an ideal case where only dry reforming of methane occurs, a H_2/CO ratio of 1 is to be expected for an equimolar feed of CO_2 and CH_4. Deviation from this expected outcome will be used as the basis to determine the occurrence of side reactions during dry reforming.

According to Aramouni *et al.* (2017), the Boudouard reaction is the most likely cause for a H_2/CO ratio > 1 at lower temperatures. This is because the reaction is exothermic and consumes CO which would lead to a higher H_2/CO ratio. However, a H_2/CO ratio > 1 at higher temperatures would likely be due to the methane decomposition reaction (Aramouni *et al.*, 2018). This result is plausible because this reaction is endothermic and produces H_2. Based on similar observations, Pakhare & Spivey (2014) concluded that having a H_2/CO ratio > 1 is often an indicator of carbon formation. This is because both the Boudouard and methane decomposition reaction lead to the formation of carbon.

In addition, Pakhare & Spivey (2014) also concluded that the occurrence of the RWGS reaction was the most likely cause of a H_2/CO ratio < 1 at high temperatures. This is because the reaction is endothermic which makes it the mostly likely reaction through which H_2 produced via dry DRM is consumed at high temperatures. This reasoning

was also supported in the work carried out by Aramouni *et al.* (2017) and Nikoo & Amin (2011). The study by Nikoo & Amin (2011), also concluded that a H_2/CO ratio of 1 from an equimolar feed of CH_4 and CO_2 could be achieved at temperatures above 900 °C. The reason for this was that the DRM reaction is more thermodynamically favoured than the side reactions competing with it at those temperatures.

2.2.6 Carbon formation

According to Aramouni *et al.* (2017) and Bradford & Vannice (1999), methane decomposition and the Boudouard reaction are the primary causes of carbon formation during the dry reforming reaction. The Boudouard reaction was found to be more dominant at lower temperatures and higher pressures. This is because the reaction is exothermic and results in the formation of less moles of gas making it more favourable at higher pressures according to Le Chatelier's principle. On the other hand, methane cracking was found to be more dominant at higher temperatures and lower pressures. This is because it is endothermic and leads to the formation of more moles of gas.

2.2.7 Mixed reforming

The effect of adding additional oxidants such CO_2 and O_2 in DRM has also been studied in what is termed mixed reforming. According to Bradford & Vannice (1999) this could be quite beneficial because it has benefits such as greater control of the H_2/CO ratio, minimising energy usage (through combining partial oxidation which is mildly exothermic occurring alongside DRM) and the reduction of carbon deposits through their gasification. Wang *et al.* (1996), also found that the addition of steam during DRM led to carbon formation being supressed. Nikoo & Amin (2011) and Nematollahi *et al.* (2012) both carried out studies to investigate the effect of feeding O_2 in DRM. From their studies they both concluded that feeding O_2 in DRM led to a decrease in carbon formation. Both studies also found that the CO_2 conversion decreased whilst the CH_4 conversion increased with increasing O_2 content in the feed. Additionally, the yield of both H_2 and CO was found to decrease with increasing O_2 content in the feed. These results were attributed to the increased likelihood of full oxidation of CH_4, H_2 and CO occurring at high O_2 content in the feed. To balance the benefits of reducing carbon formation offered by the feeding of O_2 without adversely

affecting the yield of synthesis gas in DRM, Nikoo & Amin (2011) recommended that a CH_4:CO_2:O_2 feed ratio of 1:1:0.1 and a reaction temperature of 1073 K would be optimum. Nematollahi *et al.* (2012) also reached a similar conclusion as they suggested that a CH_4:CO_2:O_2 feed ratio of 1:0.5-1:0.2-0.4 and a reaction temperature above 627 °C would be optimum.

2.3 Catalyst deactivation

2.3.1 Coking

Coking of the catalyst in DRM occurs mainly due to the high operating temperatures used. This is because they provide enough energy to cleave C-H bonds (Aramouni *et al.*, 2018). According to Aramouni *et al.* (2018), the three main forms of coke caused by carbon deposition are pyrolytic, whisker and gum (encapsulating carbon). Pyrolytic coke is mainly formed by exposure of hydrocarbons to high temperatures (above 600°C) (Abdullah *et al.*, 2017). Whisker carbon occurs when a hydrocarbon reaction leads to the nucleation of graphitic carbon on the sides of active metal particles (Abdullah *et al.*, 2017). This process usually occurs at temperatures above 450°C. Gum tends to be formed when the feed contains heavy hydrocarbons or aromatic compounds. It also tends to occur at lower temperatures in comparison to the other two types of coke (below 500°C) (Abdullah *et al.*, 2017).

Of the types of coke mentioned, whisker (filamentous) carbon is the most undesirable especially in nickel catalysts (Aramouni *et al.*, 2018). This is because whisker carbon has been reported to be able to push nickel out of the catalyst structure as well as cause catalyst pellets to break. The breaking of the catalyst pellets can cause an increase in pressure drop in reactors as well as deactivation of the catalyst surface (Abdullah *et al.*, 2017).

According to Abdullah *et al.* (2017), coking in dry reforming occurs through a variety of side reactions. These include the decomposition of methane, hydrogenation of CO_2 and CO as well as the Boudouard reaction (Abdullah *et al.*, 2017). Of these reactions, the hydrogenation of CO and CO_2 and the Boudouard reaction are exothermic ($\Delta H<0$) whilst the decomposition of methane is endothermic ($\Delta H>0$). It is likely that coking at

lower temperatures can be attributed to the exothermic reactions whilst at higher temperatures the endothermic reactions are responsible.

2.3.2 Sintering

According to Moulijn *et al.* (2001), sintering is defined as, “the loss of catalyst active surface area due to crystallite growth of either the support or the active phase.” In this process small particles grow into larger ones via a variety of mechanisms such as surface migration, coalescing and volatilisation. Moulijn *et al.* (2001), also stated that the most significant mechanism of sintering small particles was the movement of atoms rather than particles. These movements are dependent on conditions such as the type of surface as well as temperature.

In addition, Moulijn *et al.* (2001) also highlighted that sintering is strongly dependent on temperature. This is because its underlying mechanisms such as surface diffusion or mobility of larger particles are influenced by temperature. Therefore, having correlations based on temperature to predict sintering would be useful. The Tamman and Hüttig temperatures are two such correlations (semi-empirical) that indicate the temperature at which sintering might occur. The equations defining these correlations are given in Equation (2.10) and (2.11).

$$\boldsymbol{T_{Hüttig} = 0.3T_{melting}} \qquad \text{Equation (2.10)}$$

$$\boldsymbol{T_{Tamman} = 0.5T_{melting}} \qquad \text{Equation (2.-11)}$$

The definitions of the Tamman and Hüttig temperatures are based on the melting points of the solids being considered. This is because solid-state diffusion is strongly related to the melting points of solids (Moulijn *et al.*, 2001). Solid-state diffusion is also believed to become faster as the temperature approaches the melting point. At the Hüttig temperature, atoms at defects become mobile whilst at the Tamman temperature, atoms from the bulk will exhibit mobility.

It must be noted that the temperature at which solids become mobile is also dependent on other factors such as morphology, size, and texture. To illustrate this, Moulijn *et al.* (2001) found the γ-Al_2O_3 support which is highly porous to more sensitive to sintering

than α-Al_2O_3 support. Additionally, it was determined that mobility for small particles might occur at temperatures below the Hüttig and Tamman temperatures. Therefore, the Hüttig and Tamman temperatures are good as a guide to predict particle mobility, but they may not exactly define it in all scenarios.

Due to the high temperatures that catalyst testing will be carried out at (600 – 800 °C), sintering is likely to play a role in catalyst deactivation.

2.3.3 Active metal oxidation

The oxidation of active metal has also been reported to cause catalyst deactivation. According to a study carried out by Takanabe *et al.* (2005), Co/TiO_2 catalysts displayed poor catalytic activity in comparison to nickel and bimetallic nickel-cobalt (Ni-Co) catalysts. This deactivation was attributed to the formation of a cobalt titanite ($CoTiO_3$) resulting from the interaction between the support and active metal. The $CoTiO_3$ phase is catalytically inactive. Additionally, in the work done by Guo *et al.* (2004), Ni supported on γ-Al_2O_3 catalysts were also found to have significant losses in activity during the dry reforming reaction. These were attributed to the metallic Ni forming $NiAl_2O_4$. These two studies illustrate the potential of active metal oxidation to cause loss in catalytic activity.

2.4 Catalysts

2.4.1 Overview

To promote the DRM reaction, noble and non-noble metal catalysts have been extensively investigated (Aramouni *et al.*, 2018). The activity and stability of the catalysts investigated were found to be influenced by the choice of active metal, support material and promoters (Aramouni *et al.*, 2018). The pros and cons for both noble and no-noble metal catalysts will be discussed in the sections to follow.

2.4.2 Noble metal catalysts

The use of noble metal catalysts in DRM is attractive because they tend to have better stability in comparison to non-noble metal catalysts (Aramouni *et al.*, 2018). Their stability arises from the fact that they tend to be less susceptible to carbon deposition, sintering and the formation of metal-support compounds. To illustrate this, a study

carried out by Hou *et al.* (2006) found that noble metal catalysts such as ruthenium, rhodium, palladium, platinum and iridium had higher resistance to coke deposition in comparison to nickel and cobalt catalysts. Rostrup-Nielsen & Hansen (1993) also had similar findings as they determined that rhodium and ruthenium catalysts had lower selectivity for carbon formation compared to nickel catalysts. According to Aramouni *et al.* (2018), the high resistance to coke deposition exhibited by noble metal catalysts arises from their ability to be well dispersed on catalyst supports and retaining small particle sizes during reactions.

Despite their stability, the use of noble metal catalysts at an industrial scale would not be feasible from a practical standpoint. This is mainly due to their high cost and limited availability (Aramouni *et al.*, 2018). However, they could still be useful as promoters in non-noble metal catalysts. For example Pawelec *et al.* (2007), and Steinhauer *et al.* (2009) found that the addition of platinum and palladium to nickel catalysts enhanced catalyst stability in DRM in comparison to having pure nickel catalysts. García-Diéguez *et al.* (2011) and Hou & Yashima (2003) had similar findings when rhodium was used as a promoter in nickel catalysts. The improvements in coke resistance during DRM that were observed in the study carried out by Hou & Yashima (2003), were attributed to the improvement in dispersion in the catalyst caused by the presence of rhodium. Nagaoka *et al.* (2004), also found that the use of platinum and ruthenium improved the stability of cobalt catalysts in DRM.

2.4.3 Non-noble metal catalysts

To address the issues around cost and availability that affect the use of noble metal catalysts in DRM, non-noble metal catalysts have been considered. This is because they are cheaper and are more readily available. Amongst the non-noble metal catalysts, nickel catalysts have been widely considered due to their low cost, availability and their relatively high catalytic activity (Aramouni *et al.*, 2018). However, these catalysts mostly tend to suffer deactivation due to coking (Guo *et al.*, 2004). Cobalt catalysts have also received consideration for use in DRM, but they tend to succumb to similar flaws to the nickel catalysts (Hou *et al.*, 2006).

To overcome the deactivation problems seen in non-noble metal catalysts, alloyed catalysts (in particular bimetallic catalysts) have also been considered (Aramouni *et al.*, 2018). This is because there is a theory that bimetallic catalyst systems can lead to catalysts that have better activity and stability compared to monometallic catalysts by increasing the dispersion and reducing the size of the active metal in the catalysts (Aramouni *et al.*, 2018). Zhang *et al.* (2007), carried out a study in which the activity and stability in DRM of nickel-cobalt (Ni-Co), nickel-copper (Ni-Cu), nickel-iron (Ni-Fe) and nickel-manganese (Ni-Mn) bimetallic catalysts supported on aluminium magnesium oxides were compared. In the study, it was determined that the order of the catalysts in terms of catalytic activity was as follows: Ni-Co > Ni-Mn > Ni-Fe > Ni-Cu. On the other hand, the order of the catalysts in terms of resistance to carbon formation was as follows: Ni-Co > Ni-Cu > Ni-Mn > Ni-Fe. This study concluded that of the bimetallic catalyst systems that were considered, Ni-Co performed the best in terms of activity and stability. As of such, Ni-Co catalysts have generated a significant amount of consideration as catalysts in DRM.

Horlyck *et al.* (2018), carried out an investigation to elucidate why Ni-Co bimetallic catalysts perform better than monometallic nickel and cobalt catalysts in DRM. This was done by analysing the performance of nickel, cobalt, and Ni-Co catalysts in the DRM reaction as well as the methane cracking, Boudouard and RWGS side reactions. The study was unique in that it used the performance of the catalysts (in terms of activity, stability, and selectivity) in the side reactions to explain the performance of the catalysts in the DRM reaction. All the catalysts considered in the study were supported on alumina prepared by flame spray pyrolysis.

From the results in the methane cracking and RWGS reactions, it was determined that the nickel catalyst had higher initial CH_4, and CO_2 conversions compared to the cobalt catalyst. However, in the methane cracking reaction the activity of the nickel catalyst decreased significantly as the reaction proceeded. This decrease in activity was attributed to the deposition of carbon on the nickel catalyst. These results were used to show that the nickel catalyst was more selective and active towards the conversion of CH_4 and CO_2 than the cobalt catalyst (Horlyck *et al.*, 2018). In addition, the carbon deposited on nickel was deemed to lead to catalyst deactivation.

In the Boudouard reaction, the cobalt catalyst was found to have a higher initial CO conversion than the nickel catalyst. The cobalt catalyst also managed to maintain this activity whilst a sharp decrease in activity was observed for the nickel catalyst as the reaction proceeded. Surprisingly, when the catalysts were analysed after the reaction the cobalt catalyst was found to have more carbon deposited on it than the nickel catalyst. This result was used to show that the carbon deposits on the cobalt catalyst because of the Boudouard reaction did not lead to a loss in activity as was the case with the carbon deposits on the nickel catalyst from the methane cracking reaction.

In the DRM reaction, Horlyck *et al.* (2018) found that the bimetallic Ni-Co catalysts were the most active followed by the monometallic nickel catalyst. The monometallic cobalt catalyst was the least active of all the catalysts. However, the activity of the nickel catalyst dropped with increasing time on stream whilst that of the cobalt catalyst remained stable. In terms of carbon deposition, the cobalt catalyst performed best with the least amount of carbon deposited, followed by the bimetallic Ni-Co catalysts with the nickel catalyst having the most carbon deposits. These findings led Horlyck *et al.* (2018) to conclude that in bimetallic Ni-Co catalysts, the activity displayed arises from the presence of nickel in the catalyst whilst cobalt ensures that the catalysts are more resistant to carbon deposition. This conclusion was in line with the performance displayed by the catalysts in the side reactions where it was shown that nickel is better at activating CO_2 and CH_4 whilst the carbon deposits on the cobalt catalysts did not lead to catalyst deactivation.

Studies carried out by Gao *et al.* (2017) and Luisetto *et al.* (2012) also had findings that were similar to those of Horlyck *et al.* (2018). This was because in their studies Ni-Co catalysts proved to be more active in comparison to monometallic nickel and cobalt catalysts in DRM. Luisetto *et al.* (2012) also reported that the Ni-Co and cobalt catalysts had less carbon deposited on them which further supported the conclusion reached by Horlyck *et al.* (2018) that cobalt provides more resistance to carbon formation in DRM than nickel. However, Gao *et al.* (2017) attributed the better performance of the Ni-Co catalyst to be due to their ability to maintain smaller size and high dispersion compared to monometallic cobalt and nickel catalysts. The catalysts studied by Gao *et al.* (2017) were supported on silica whilst those studied by Luisetto *et al.* (2012) were supported on ceria.

Studies carried out by Takanabe *et al.* (2005) and Ay & Üner (2015) for the most part had similar findings to those by Horlyck *et al.* (2018), Gao *et al.* (2017) and Luisetto *et al.* (2012). The studies agreed on the fact that nickel catalysts are more active than cobalt catalysts in DRM. This was because the cobalt catalysts had the lowest conversions during catalyst testing. This poor performance was attributed to be due to strong metal-support interactions (SMSI) by Ay & Üner (2015) and active metal oxidation through the formation of metal-support compounds by Takanabe *et al.* (2005). However, the findings by Takanabe *et al.* (2005) and Ay & Üner (2015) differed from those obtained by Horlyck *et al.* (2018), Gao *et al.* (2017) and Luisetto *et al.* (2012) in that they found out that nickel catalysts slightly outperformed the Ni-Co catalysts in terms conversion in DRM. In terms of catalyst stability, the studies by Ay & Üner (2015) and Takanabe *et al.* (2005) also found that carbon deposition was more significant on the nickel catalysts compared to the cobalt catalysts. The findings in terms of stability were also in agreement to those by Horlyck *et al.* (2018), Gao *et al.* (2017) and Luisetto *et al.* (2012). The catalysts studied by Takanabe *et al.* (2005) were supported on titania whilst those studied by Ay & Üner (2015) were supported on ceria.

Disagreements regarding the superiority of bimetallic Ni-Co and nickel catalysts over cobalt catalysts in terms of performance also exist in the field of DRM. For example, a study carried out by San-José-Alonso *et al.* (2009) determined that cobalt catalysts performed better than bimetallic Ni-Co and nickel catalysts. Furthermore, the study also found that the cobalt and cobalt rich Ni-Co catalysts had more carbon deposited on them in comparison to the nickel and nickel rich Ni-Co catalysts. Despite having more carbon deposits, the cobalt catalyst was more active and stable in comparison to its nickel counterpart. To explain their findings, San-José-Alonso *et al.* (2009) attributed the presence of large particles in the cobalt catalysts to be behind their stability. This is because larger particles are unlikely to be fully encapsulated by carbon meaning that they can maintain their activity in the presence of carbon deposits. However, this could eventually lead to reactor blockages over long term use which would be problematic. In addition, it was also proposed that the higher activity displayed by the cobalt catalyst could be due to it being more active than the nickel catalyst in the methane decomposition reaction which is normally the rate limiting step in DRM. Lastly, it must be noted that during catalyst preparation, the catalysts in this

study were not calcined after the addition active metal to the support which is generally the norm. This was because the authors believed that calcination increases the chance for the cobalt to lose its catalyst activity through metal oxidation. However, the catalysts were reduced before catalyst testing which was done in the rest of the studies considered. The catalysts studied by San-José-Alonso *et al.* (2009) were supported on γ-alumina.

From the literature reviewed it is evident that some disagreement exists regarding whether bimetallic Ni-Co catalysts are more active and stable in DRM in comparison to monometallic nickel and cobalt catalysts. This is because valid arguments have been made for each viewpoint.

2.5 Catalyst supports

2.5.1 Overview

The performance of a catalyst is not only influenced by the choice of the active metal but also by the support that is chosen (Aramouni *et al.*, 2018). This is because supports provide properties that ensure that the catalytically active nano particles are well dispersed as well as resistant to coking (Aramouni *et al.*, 2018). Additionally, the interaction between the support and active metal species (metal-support interactions) also affects the stability of the catalyst in terms of sintering as well as the reducibility of the active metal (Aramouni *et al.*, 2018). The impact of the choice of supports in the dry reforming reaction was investigated in-depth by Zhang *et al.* (2015) as well as Guo *et al.* (2004).

In the study carried out by Zhang *et al.* (2015), structural properties as well as catalytic performance of nickel (Ni) based catalysts supported on silica (SiO_2), titania (TiO_2), zirconia (ZrO_2), alumina (Al_2O_3), magnesium oxide (MgO), and magnesium oxide modified alumina ($MgO\text{-}Al_2O_3$) were analysed. All the supports were loaded with 8 wt.% Ni whilst catalyst testing was carried out at 750 °C. The study carried out by Guo *et al.* (2004), was also similar in that it analysed the performance of Ni-based catalysts supported on Al_2O_3, $MgO\text{-}Al_2O_3$ as well as magnesium aluminate ($MgAl_2O_4$) at 750 °C. However, the study by Guo *et al.* (2004) differed in that a metal loading of 10 wt.% was employed.

From the study carried out Zhang *et al.* (2015), the catalysts supported on TiO_2, ZrO_2 and SiO_2 were found to have weak metal-support interactions (MSI). This was illustrated by the low reduction temperatures (between 300 – 500 °C) that were obtained when the catalysts were analysed through hydrogen temperature reduction (H_2-TPR). Reduction temperatures were used to compare metal-support interactions as they are generally viewed as a good indicator of their strength. The weak metal-support interactions of the catalysts supported on TiO_2, ZrO_2 and SiO_2 made their reduction easier. This was beneficial because it ensured that more active metal would be available to facilitate the dry reforming reaction. However, this benefit did not translate into good catalytic performance because the catalysts were deactivated through sintering during catalyst testing. The occurrence of sintering was attributed to the weak metal-support interactions.

In comparison, the catalysts that were supported on MgO and Al_2O_3 did not experience deactivation through sintering (Zhang *et al.*, 2015). This was because these catalysts had strong metal-support interactions. This was illustrated by their higher reduction temperatures (reduction was incomplete at 900 °C). However, these strong metal-support interactions had a downside in that they led to the formation of the nickel aluminate ($NiAl_2O_4$) spinel and nickel and magnesium oxide (NiO-MgO) solid solutions. Both these phases are catalytically inactive in DRM and are difficult to reduce. The combination of these factors led to the catalysts performing poorly during testing. The findings for the Al_2O_3 supported catalyst were also supported by Guo *et al.* (2004) who also attributed their low activity to the formation of the $NiAl_2O_4$ spinel. In addition, the Al_2O_3 catalysts were found to have higher carbon deposits in comparison to the other catalysts tested due to their acidity.

The study carried out by Zhang *et al.* (2015) concluded that MgO-Al_2O_3 was the best support amongst those they considered. This was because combining MgO and Al_2O_3 was found to resolve some of the issues encountered by the Al_2O_3 support alone. To illustrate this, the presence of MgO was found to supress the formation of the $NiAl_2O_4$. This was because Mg^{2+} was found to react more easily with Al_2O_3 than Ni^{2+} which led to $MgAl_2O_4$ being formed instead of $NiAl_2O_4$. Additionally, the catalysts supported on MgO-Al_2O_3 were more easily reduced in comparison to those supported on Al_2O_3

catalysts because of the weaker metal-support interactions that were caused by the presence of MgO. The improved reducibility was exhibited in the form of good catalytic performance during catalyst testing. Despite the metal-support interactions observed in MgO-Al_2O_3 being weaker than those in Al_2O_3, sintering was not observed. The findings obtained by Guo *et al.* (2004), for the Al_2O_3 and MgO-Al_2O_3 supported catalysts were also similar. The only significant difference was that the catalysts supported on $MgAl_2O_4$ were found to slightly outperform those supported on MgO-Al_2O_3. This was attributed to the catalysts having improved dispersion as well as better resistance to sintering. $MgAl_2O_4$ supported catalysts were also found to have improved resistance to coking due to their lower acidity.

2.5.2 Effect of the acidity/basicity

When choosing a support for catalysts to be used in DRM, the acidity/basicity of the catalyst support is another factor that must be considered. This is because a catalysts resistance to carbon formation is greatly affected by the acidity/basicity of the support (Jang *et al.*, 2019). According to Abdulrasheed *et al.* (2019) and Jang *et al.* (2019), supports with high acidity promote the accumulation of carbon from methane decomposition on their surfaces. This is because methane decomposition is enhanced by acid sites (Wittich *et al.*, 2020). The enhancement of methane decomposition on acidic supports is detrimental in terms of resistance to carbon formation because it inhibits the dissociative chemisorption of CO_2 on the catalyst surface which plays an essential role in the gasification of carbon deposited during the reaction (Abdulrasheed *et al.*, 2019). This is because carbon deposits also block the basic sites responsible for carbon dioxide adsorption and activation on the support (Fan *et al.*, 2009). On the other hand, catalyst supports with high basicity tend to be more resistant to carbon deposition. This is because having a high basicity improves the adsorption of CO_2 (which is mildly acidic) onto the catalyst surface (Abdulrasheed *et al.*, 2019). The increase in the amount of CO_2 on the support then leads to an acceleration of its activation on basic sites (Phan *et al.*, 2018). This is beneficial because the activated CO_2 species oxidise surface carbon formed during the reaction hence inhibiting carbon accumulation (Jang *et al.*, 2019). The relationship between surface acidity/basicity and catalyst performance was studied in depth by Das *et al.* (2017).

In the study carried out by Das *et al.* (2017), nickel catalysts supported on commercial MgO (basic support), commercial SiO_2 (acidic support) as well as Al_2O_3 and SiO_2 catalysts doped with 1% Cerium and 3% Magnesium (moderate acidity/basicity) were tested in the DRM reaction at 700 °C. The results of the study showed that catalysts with higher acidity favoured the methane decomposition reaction. This was illustrated by highest amount of carbon deposits after the reaction being observed on the catalysts with higher acidity. Therefore, the deactivation experienced by these catalysts was attributed to carbon deposition.

In contrast, the amount of carbon deposited on catalysts with higher basicity was found to be significantly lower. This was attributed to catalysts with higher basicity having higher CO_2 adsorption on their surfaces. Having a higher CO_2 adsorption eventually results in more adsorbed oxygen being available to oxidise carbon formed on the catalyst surface hence inhibiting carbon deposition. Despite this apparent benefit, excessive catalyst basicity was also found to be detrimental to catalyst activity. This is because having a large amount of CO_2 adsorbed on the surface was found to hinder other molecules coming into contact with the catalyst surface. In addition, increased CO_2 adsorption on the surface also resulted in excess oxygen from carbon dioxide activation being available to cause active metal oxidation. Both factors negatively affect catalytic activity.

The work carried out by Das *et al.* (2017), also expanded the knowledge in the field by looking at the effect that catalyst surface acidity/basicity had on the turnover frequency (TOF) which is a measure of catalytic activity as well as the activation energies (E_a) of CH_4 and CO_2. The findings of their study are provided in Figure 2.4. From the figure it is apparent that the activation of CH_4 is favoured on catalysts with higher acidity whilst those with higher basicity favour CO_2 activation (based on the E_a values). This agreed with the prior conclusion that CH_4 and CO_2 activation are favoured at higher acidity and higher basicity respectively. In addition, the highest catalytic activity in terms of the TOF was recorded for catalysts with moderate acidity/basicity where the E_a's of both reactants are similar. From this it can be concluded that an ideal support for DRM must be balanced in terms of acidity/basicity.

This is to ensure that it can enjoy the benefits of both acidic and basic sites without experiencing the downsides related to having excessive acidity or basicity.

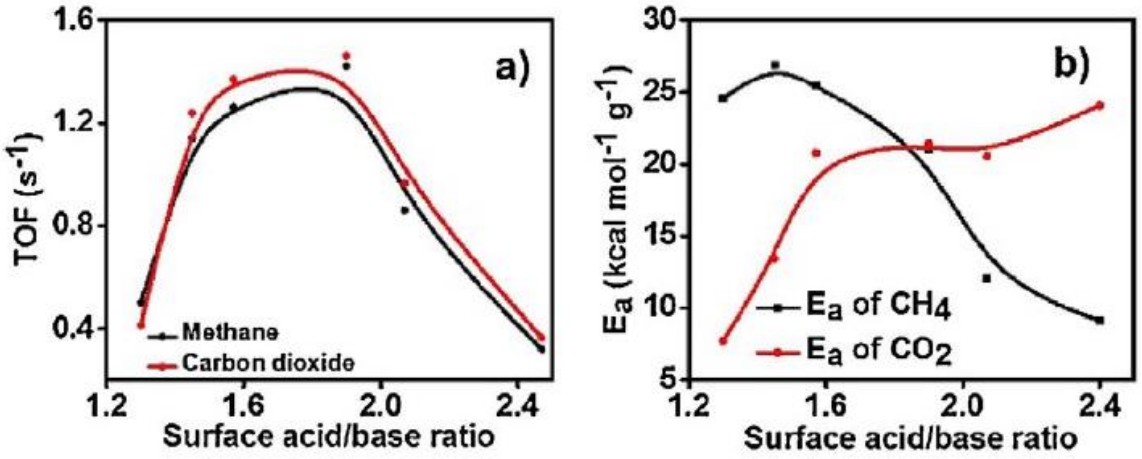

Figure 2.4: The effect of the catalyst surface acidity/basicity on the TOF of the catalyst as well as the activation energy of the reactants from (Das et al., 2017).

2.5.3 Oxygen storage capacity, oxygen vacancies and redox properties

In addition to the effect that the acidity/basicity of a catalyst support plays in determining a catalysts resistance to carbon formation, the presence of oxygen vacancies in the support also plays an equally important role. This is mainly due to the role that oxygen vacancies play in the activation of CO_2 in DRM (Abdulrasheed *et al.*, 2019). Oxygen vacancies are defined by Gerosa *et al.* (2015) as being the, "prototype representation of inherent point defects on metallic oxide catalysts developed in the process of synthesis due to exposure to elevated temperatures and a reducing atmosphere." They are beneficial in DRM because they act as sites for CO_2 activation and C-O bond cleavage (Pakhare & Spivey, 2014). This then leads to an increase in the number of mobile oxygen atoms on the surface that can react with surface carbon, hence lowering the accumulation of carbon deposits.

Ceria (CeO_2) is a support that has been used in DRM because of the existence of oxygen vacancy sites on it (Djinović *et al.*, 2012). In addition, CeO_2 also has a high oxygen storage capacity (OSC) based on its ability to store and release oxygen depending on whether it is on an oxidising or reducing environment (Roh *et al.*, 2001). CeO_2's high OSC is mainly attributed to its good redox properties which enable it switch between its Ce^{4+} and Ce^{3+} states (Ay & Üner, 2015). The redox properties of

CeO_2 also allow it to maintaining its structural integrity during oxygen removal/uptake from its lattice (Sun *et al.*, 2019). In addition, it has been reported that materials with redox properties can improve catalyst stability by reacting directly with carbon-containing reactants and intermediates to produce H_2 and CO to minimize carbon formation and deposition (Abdulrasheed *et al.*, 2019). This was illustrated in the work carried out by Laosiripojana & Assabumrungrat (2005) where it was reported that CeO_2 can reduce carbon deposition by utilising its redox properties to be reduced to non-stoichiometric CeO_{2-x} by methane and hydrogen before being re-oxidised by carbon dioxide. This is shown in Equations (2.-12) to (2.14). Despite all the positive benefits of using CeO_2 as a support in DRM, there are downsides that also exist. The main problem of using CeO_2 as a support in DRM is that it has weak thermal stability at high temperatures under reductive atmospheres (Wang *et al.*, 2017). This results in the OSC being reduced as well as sintering due to the metal support becoming weakened.

$$\boldsymbol{CeO_2 + xCH_4 \rightleftharpoons CeO_{2-x} + xCO + 2H_2} \qquad \text{Equation (2.12)}$$

$$\boldsymbol{CeO_2 + H_2 \rightleftharpoons CeO_{2-x} + xH_2O} \qquad \text{Equation (2.13)}$$

$$\boldsymbol{CeO_{2-x} + xCO_2 \rightleftharpoons CeO_2 + xCO} \qquad \text{Equation (2.14)}$$

2.5.4 Choice of magnesium aluminate ($MgAl_2O_4$) support

After considering all the various properties that are required for a good support material for the dry reforming reaction, $MgAl_2O_4$ was chosen as the support material for use in this project. This is because it strikes a good balance between reducibility as well as stability in terms of sintering and coking which are essential to achieve good catalytic performance. In addition, having a support that is thermally stable is of great importance to this project because catalyst testing will be carried out at high temperatures (600 – 800 °C). $MgAl_2O_4$, is good in this regard as it has a high melting temperature (2135 °C) (Guo *et al.*, 2004). This high melting point would translate to high Hüttig and Tamman temperatures making the active metal less likely to sinter during catalytic testing. Lastly, $MgAl_2O_4$ is neutral in terms of acidity/basicity having a balance of acidic and basic support behaviour. This is ideal because it can benefit

from having the properties of both types of supports without succumbing to the detrimental aspects either one of them.

2.6 Reaction Mechanism

In the field of methane dry reforming, monofunctional and bifunctional reaction mechanisms have been proposed. The difference between these two mechanisms is that the support is involved in the activation of CO_2 in a bifunctional mechanism whilst in a monofunctional mechanism both CH_4 and CO_2 are activated on the active metal.

According to Ferreira-Aparicio *et al.* (2000), Budiman *et al.* (2012), Fan *et al.* (2009), Das *et al.* (2017) and Papadopoulou *et al.* (2012), the first step in both monofunctional and bifunctional mechanisms is the adsporption of CH_4 onto active metal sites and its subsequent dissociation. The steps in this part of the mechanism are given in Equations (2.15) to (2.17). In the equations x, can take any integer value between 0 and 4 whilst M represents a metal active site.

$$\boldsymbol{CH_{4(gas)} + M \rightleftharpoons CH_4 - M} \qquad \text{Equation (2.15)}$$

$$\boldsymbol{CH_4 - M + (4-x)M \rightleftharpoons CH_x - M + (4-x)H - M} \qquad \text{Equation (2.16)}$$

$$\boldsymbol{2H - M \rightleftharpoons H_{2(gas)} + 2M} \qquad \text{Equation (2.17)}$$

After the activation of CH_4 on the active metal sites, Ferreira-Aparicio *et al.* (2000), Fan *et al.* (2009) and Budiman *et al.* (2012) postulated that for monofunctional mechanisms the activation of CO_2 was carried out on active metal sites following Equations (2.18) to (2.21). Fan *et al.* (2009) and Budiman *et al.* (2012) also suggested that monofunctional reaction mechanisms occurred on acidic supports. Ferreira-Aparicio *et al.* (2000) went on to suggest that supports in which monfuntional mechanisms are observed in tending to be more susceptible to the accumulation of carbon as the reaction proceeds. This is because the dissociative adsorption of CO_2 becomes limited due to the accumulation of dehydrogenated carbon deposits (CH_x) coming from the activation of CH_4 which also occurs on the active metal sites. These carbon deposits eventually blocks the metal active sites responsible for the activation of CO_2 leading to loss in activity.

$$CO_{2(gas)} + M \rightleftharpoons CO_2 - M \quad \text{Equation (2.18)}$$

$$CO_2 - M + M \rightleftharpoons CO - M + O - M \quad \text{Equation (2.19)}$$

$$CH_x - M + O - M \rightleftharpoons CO - M + xH - M \quad \text{Equation (2.20)}$$

$$CO - M \rightleftharpoons CO_{gas} + M \quad \text{Equation (2.21)}$$

On the otherhand, Ferreira-Aparicio *et al.* (2000) found that catalysts which were found to exhibit bifunctional mechanisms tended to be less susceptible to losses in activity from the buildup of carbon deposits. The main reason for this was the involvement of the catalyst support in the mechanism. Ferreira-Aparicio *et al.* (2000), suggested that supports having OH groups available to participate in the mechanism could combat the builup of CH_x species which was observed in monofuntional mechanisms by reacting with them. This mechanism through which they were able to do so is given in Equations (2.22) to (2.26). In the mechanism to follow, S represents an active site on the catalyst support.

$$OH_{(support)} \rightleftharpoons OH - M \quad \text{Equation (2.22)}$$

$$OH - M + M \rightleftharpoons O - M + H - M \quad \text{Equation (2.23)}$$

$$CO_2 - M + M \rightleftharpoons CO - M + O - M \quad \text{Equation (2.24)}$$

$$CH_x - M + O - M \rightleftharpoons CO - M + xH - M \quad \text{Equation (2.25)}$$

$$CO - M \rightleftharpoons CO_{(gas)} + M \quad \text{Equation (2.26)}$$

In addition, Ferreira-Aparicio *et al.* (2000) went on to suggest that supports such as alumina which have the ability to hydrate and dehydrate themselves as shown in Equations (2.27) and (2.28) can play a crucial role in the activation of CO_2.

$$2OH^-_{(support)} \rightleftharpoons H_2O - S + O^{2-}_{(support)} \quad \text{Equation (2.27)}$$

$$H_2O - S \rightleftharpoons H_2O_{(gas)}$$ Equation (2.28)

This is because the O^{2-} and OH^- species produced from the support hydration and dehydration could react with CO_2 to form carbonate (CO_3^{2-}) and bicarbonate (HCO_3^-) species as shown in Equations (2.30) and (2.31) respectively. The carbonate and bicarbonate species could then react with H to form formate (HCO_2^-) species as shown in Equation (2.33) and (2.34). Finally the formate species can lead to the formation of CO as shown in Equation (2.35). Equations (2.29) to (2.36) provide all the steps in the mechanism put forward by Ferreira-Aparicio *et al.* (2000) through which CO_2 was activated through the formation of carbonate and bicarbonate species because of the participation of the support in the mechanism.

$$CO_{2(gas)} + S \rightleftharpoons CO_2 - S$$ Equation (2.29)

$$CO_2 - S + O^{2-}_{(support)} \rightleftharpoons CO_3^{2-} - S$$ Equation (2.30)

$$CO_2 - S + OH^-_{(support)} \rightleftharpoons HCO_3^- - S$$ Equation (2.31)

$$2H - M \rightleftharpoons 2H - S$$ Equation (2.32)

$$CO_3^{2-} - S + 2H - S \rightleftharpoons HCO_2^- - S + OH^-_{(support)}$$ Equation (2.33)

$$HCO_3^- - S + 2H - S \rightleftharpoons HCO_2^- - S + H_2O - S + S$$ Equation (2.34)

$$HCO_2^- - S \rightleftharpoons CO - S + OH^-$$ Equation (2.35)

$$CO - S \rightleftharpoons CO_{(gas)} + S$$ Equation (2.36)

Fan *et al.* (2009) and Budiman *et al.* (2012) also put forward bifunctional mechanisms in which the activation of CO_2 came about through the formation of carbonate species because of the involvement of the catalyst support. However, their argument was that this behaviour occurred primarily on basic supports. However, this notion was

challenged by the work carried out by Bitter *et al.* (1998) which found that ZrO_2 which is neither basic or acdic was involved in the activation of CO_2.

2.7 *In situ* magnetometer characterization

2.7.1 Overview

In DRM, the mechanisms through which catalyst deactivation occurs have been mostly studied through ex-situ characterization techniques which can only be carried out after catalyst testing. This is mainly due to the lack of in-situ characterization techniques which can monitor the occurrence catalyst deactivation mechanisms during catalyst testing. The use of an in-situ magnetometry provides a way through which catalyst deactivation could be monitored during reaction in DRM. At the University of Cape Town, an in-situ magnetometer that was developed in-house in the c*change research group with the ability to analyse the occurrence of catalyst deactivation during catalyst testing is available.

An in-situ magnetometer can analyse materials based on their magnetic properties without the need to have direct interaction with them as is the case with ex-situ characterisation techniques (Claeys *et al.*, 2010). Experiments in the in-situ magnetometer can be carried out in a controlled gas environment at elevated pressure (above 50 bar) and high temperatures (Claeys *et al.*, 2014). This is specifically beneficial in catalysis as it allows one to monitor the physical or chemical changes of catalysts at industrially relevant conditions (high temperature and elevated pressure) without having to interfere with the reaction that will be taking place (Claeys *et al.*, 2010). Deactivation phenomena such as sintering, crystallite break-up and oxidation of active metal can be analysed using this method. This is because these factors have an effect on the magnetic behaviour of catalysts (Claeys *et al.*, 2010). In addition, crystallite sizes and crystallite size distributions can also be measured in this way. Details on how this can be done will be discussed in the sections to follow.

2.7.2 Basis of *in situ* magnetometer measurements

The magnetometer can analyse material that is either ferromagnetic or superparamagnetic (Claeys *et al.*, 2010). Ferromagnetic materials display spontaneous magnetism when an external magnetic field is applied at temperatures

below the Curie temperature (T_C) (Dalmon, 1994). This is because at temperatures below T_C, the alignment of the magnetic moments and electron spins is ordered (ferromagnetic state) whilst above T_C, they become disordered (paramagnetic state) (Kittel, 2005). Upon removal of the external magnetic field, the large particles which are not affected by thermal agitation often retain the direction of the magnetic field to create remnant magnetisation (M_{rem}) (Dalmon, 1994).

Superparamagnetic material is made up of small particles of ferromagnetic material (usually smaller than 20 nm) (Dalmon, 1994). It differs from ferromagnetic material in that in the absence of an applied magnetic field, it displays no remnant magnetisation as the particles are affected by thermal agitation (Dalmon, 1994). However, in the presence of an external magnetic field, the particles display magnetism as their magnetic moments align with the direction of the applied field (Dalmon, 1994). Additionally, the magnetisation of superparamagnetic material in a magnetic field (H) is a function of particle size (Dalmon, 1994). Larger particles are more readily magnetised whilst smaller particles require stronger magnetic fields.

Since cobalt and nickel are both ferromagnetic, the in-situ magnetometer could be used to analyse occurrence of deactivation mechanisms in these catalyst during catalyst testing in DRM. It is likely that nanoparticles displaying both ferromagnetic and superparamagnetic behaviour would be present in the catalysts.

2.7.3 Determining sintering

Since sintering results in the growth of smaller catalyst particles into bigger ones, its occurrence will cause an increase in the remnant magnetisation measured. This is because particle growth would decrease the amount of superparamagnetic material in the catalyst. In a study carried out by Claeys *et al.* (2015), the weight fraction of cobalt displaying remnant magnetization (γ) during Fischer-Tropsch experiments was calculated by measuring using the saturation (M_{sat}) and remnant magnetisation (M_{rem}) using Equation (2.37) provided below.

$$\boldsymbol{\gamma = 2 * \frac{M_{rem}}{M_{sat}} * 100} \qquad \text{Equation (2.37)}$$

2.7.4 Determining active metal oxidation and carbon deposition

According to Kittel (2005), the oxides of nickel and cobalt do not display ferromagnetism. This means that the formation of these phases (including metal-support phases) during the reaction can potentially be detected by monitoring the saturation magnetisation (M_{sat}). This is because there will be a decrease in M_{sat} if phases that are not ferromagnetic are formed during the reaction. In addition, calculations carried out in the study by Claeys *et al.* (2015) also showed that the adsorption of carbon species on a cobalt surface leads to a decrease in magnetisation. This means that the deposition of carbon on catalyst surfaces could in principle also be monitored in a manner similar to the one suggested for oxidation. However, it must be noted that the effect of carbon deposition is weaker in comparison to what is observed when oxidation of a metal such as nickel is observed.

2.7.5 Ni-Co alloy Curie temperatures

As previously mentioned, ferromagnetic materials become paramagnetic at the Curie temperature. Therefore, knowledge of the Curie temperatures of the pure forms of both cobalt and nickel as well as their alloys is of importance in magnetometry studies. According to Leger *et al.* (1972), alloys of cobalt and nickel exist over the whole range of cobalt and nickel compositions with their Curie temperatures varying between the limits of the Curie temperatures of the pure metals. The Curie temperatures of pure cobalt and nickel according to Leger *et al.* (1972) are 1125 °C and 354 °C, respectively. A figure generated from data obtained from Leger *et al.* (1972) is given in Figure 2.5.

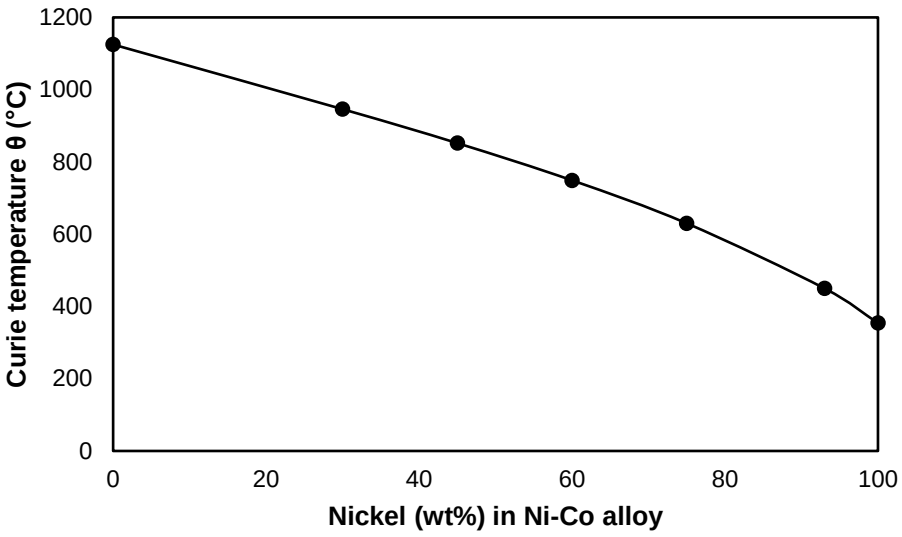

Figure 2.5: Curie temperatures of the cobalt and nickel alloy system adapted from Leger et al. (1972)

To confirm the Curie temperatures reported in the work of Leger *et al.* (1972), the work of Nichizawa & Ishida (1983) as well as Mohn & Wohlfarth (1987) was also consulted. According to Mohn & Wohlfarth (1987), the Curie temperatures of cobalt and nickel are 1115 °C and 358 °C respectively whilst Nichizawa & Ishida (1983), determined them to be 1121 °C and 361 °C respectively. Since the aforementioned Curie temperatures are similar to those obtained by Leger *et al.* (1972), they serve to confirm the results obtained from their work. A phase diagram figure analysing containing information on Curie temperatures of the Ni-Co alloy system is from work carried out by Nichizawa & Ishida (1983) is given in Figure 2.6. The Curie temperature expected for the various Ni-Co alloys are represented by the curve labelled Magnetic Transf in the figure. The figure also shows that the Ni-Co alloys can be formed across all compositions of nickel and cobalt.

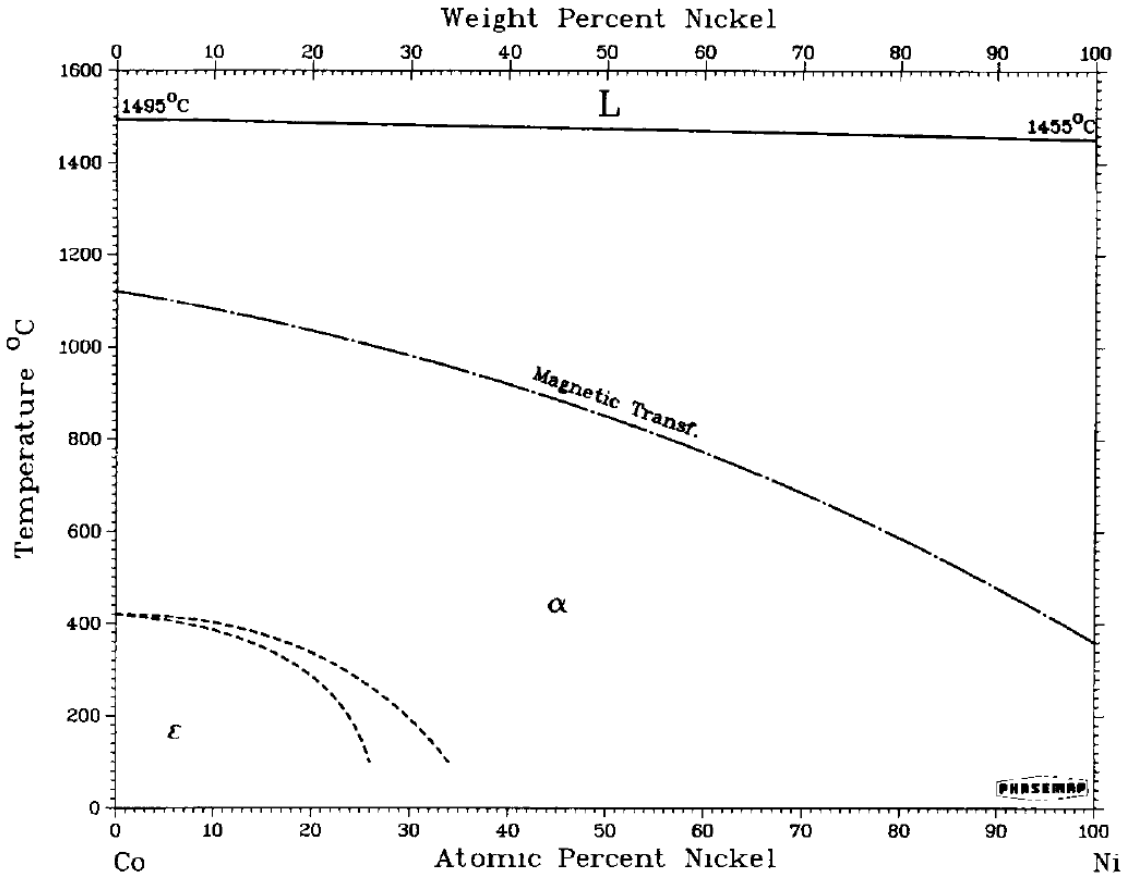

Figure 2.6: Curie temperatures of the cobalt and nickel (Nichizawa & Ishida, 1983).

3 Scope of the thesis

3.1 Project objectives

Based on the literature review, the objectives of this research are to:

- Carry out a thermodynamic analysis to gain more understanding of the dry reforming of methane.
- Synthesize bimetallic Ni-Co alloy catalysts with different compositions of nickel and cobalt as well as monometallic nickel and cobalt catalysts supported on magnesium aluminate.
- Carry out preliminary catalyst testing for some of the catalysts at temperatures between 600 – 750 °C to determine the conditions at which final catalyst testing should be carried out.
- Carry out final catalyst testing for all the catalysts prepared in the study at the conditions deemed to be optimum from preliminary catalyst testing.
- Characterize prepared catalysts before and after catalyst testing.

3.2 Hypothesis

From the information evaluated in the literature review, the following hypothesis has been postulated:

Nickel-cobalt (Ni-Co) bimetallic alloy catalysts supported on magnesium aluminate will produce catalysts that are more active and stable in the dry reforming of methane in comparison to monometallic nickel and cobalt catalysts. Additionally, based on thermodynamics, the dry reforming of methane occurs alongside side reactions such as methane decomposition and the reverse water gas shift reaction. Therefore, the occurrence of these reactions is likely to impact the conversion of CO_2 and CH_4 during the dry reforming of methane.

3.3 Key questions

Based on the objectives of the research and the hypothesis, the key questions of the research are as follows:

- From thermodynamics, what effect does the occurrence of side reactions such as methane decomposition and the reverse water gas shift reaction have on the conversion of CO_2 and CH_4 during the dry reforming of methane?

- What are the threshold conditions for the stable operation of nickel-cobalt (Ni-Co) catalysts in the dry reforming of methane?
- Does the nickel-cobalt (Ni-Co) composition of a catalyst influence its activity in the dry reforming of methane?
- Does the nickel-cobalt (Ni-Co) composition of a catalyst influence its stability in the dry reforming of methane?

4 Experimental methodology

4.1 Catalyst preparation

4.1.1 Preparation of magnesium aluminate ($MgAl_2O_4$) support

The magnesium aluminate support ($MgAl_2O_4$) used in the study was prepared through the coprecipitation method. This was done by following the methodology reported in the work of Guo *et al.* (2004) as a guideline.

To start off, stoichiometric amounts of magnesium nitrate hexahydrate ($Mg(NO_3)_2.6H_2O$, 99%, Sigma-Aldrich) and aluminium nitrate nonahydrate ($Al(NO_3)_3.9H_2O$, 98%, Sigma-Aldrich) were first separately dissolved in deionised water. The resulting solutions were then mixed before aqueous ammonia solution (NH_4OH, 25%, Kimix) was then added to precipitate the Al^{3+} and Mg^{2+} from the solution in the form of hydroxides. This resulted in the formation of a slurry. The addition of the ammonia solution was controlled to ensure that the pH could be maintained at approximately 9.5 whilst the slurry was being constantly stirred at a rate of 6 500 rpm using a disperser (IKA, Ultra-Turrax T25). The slurry was stirred for an hour before being left to age overnight.

Following the ageing process, the resultant slurry was filtered using vacuum filtration. During filtration, the filter cake was then thoroughly washed using deionised water to remove any residual ions remaining from the precipitation process. After the washing process, the filter cake was then recovered and dried overnight in an oven at 120 °C. The dried filter cake was then calcined in an air atmosphere. In the calcination process, the temperature was raised from 50 °C to 800 °C at a ramp rate of 4.17 °C/min in a calcination oven (Nabertherm, LT 5/12). Once at 800 °C, the temperature was held constant for 4 hours before it was subsequently allowed to cool to 50 °C. Thereafter the sample was crushed into a fine powder using a mortar and pestle.

4.1.2 Preparation of supported nickel-cobalt (Ni-Co) catalysts

After the preparation of the $MgAl_2O_4$ support, nickel and cobalt were then added onto the support by slurry impregnation. This was done following the methodology reported in the work of van Helden *et al.* (2020).

To start off, the stochiometric amounts of cobalt nitrate hexahydrate ($Co(NO_3)_2.6H_2O$, ≥ 98%, Sigma-Aldrich) and nickel nitrate hexahydrate ($Ni(NO_3)_2.6H_2O$, 97%, Sigma-Aldrich) required to obtain the desired Ni:Co molar ratio were dissolved in deionized water. Afterwards, the required mass of $MgAl_2O_4$ support was added to the solution to ensure an active metal (nickel and cobalt combined) loading of 10 wt.-% of the prepared catalyst. The mixture was then added to a round bottom flask which was connected to a rotary evaporator (Buchi, Rotavapor R-210/215) to evaporate the water. The evaporation was carried out at a vacuum pressure of 50 mbar and a temperature of 40 °C. Once all the water had been evaporated, the dried sample was recovered so that it could be calcined. During calcination, the temperature was raised from 50 °C to 250 °C at a ramp rate of 1 °C/min in a calcination oven (Nabertherm, LT 5/12). Once at 250 °C, the temperature was held constant for 6 hours before being cooled to room temperature. In total, seven catalysts were prepared and named Ni(100), Ni-Co(90:10), Ni-Co(70:30), Ni-Co(50:50), Ni-Co(30:70), Ni-Co(10:90) and Co(100). The compositions of the catalysts prepared are given in Table 4.1. In all the catalyst testing experiments carried out, the catalysts were first reduced in H_2 at 700 °C following the procedure outlined in Section 4.3.2.

Table 4.1: Nickel and cobalt active metal compositions of the supported metal catalysts prepared.

Sample name	Target Ni content (mol %)	Target Co content (mol %)
Ni(100)	100	0
Ni-Co(90:10)	90	10
Ni-Co(70:30)	70	30
Ni-Co(50:50)	50	50
Ni-Co(30:70)	30	70
Ni-Co(10:90)	10	90
Co(100)	0	100

4.2 Catalyst characterization

4.2.1 Brunauer–Emmett–Teller (BET) analysis

Brunauer-Emmett-Teller (BET) analysis was carried out to determine the surface area and pore volume of the supports and supported metal catalysts used in the study. In the experiments nitrogen (N_2) was used as the adsorbent gas whilst they were carried out at liquid nitrogen temperatures. The catalysts were first degassed overnight at 200

°C in a Micromeritics FlowPrep 060 sample preparation unit to prepare them for analysis. Analysis was then carried out in a Micromeritics TriStar instrument.

4.2.2 Powder X-ray diffraction (PXRD)

Powder X-ray diffraction (PXRD) analysis was carried out to determine the crystalline phases present in the catalysts and support that were prepared. This analysis was carried out using a Bruker D8 advance X-ray diffractometer equipped with a LYNXEYE E 1D mode position sensitive detector and a cobalt source (λ=1.79026 Å). In the experiments, the X-ray diffractometer was operated at 35 kV and 40 mA. A scan range of 20° < 2θ < 120° with a step size of 0.02048° and a time per step of 0.5 s were chosen resulting in a total scan time of 41 minutes and 54 seconds. The reference data to which the diffraction patterns obtained from the experiments was compared to was obtained from the ICDD PDF-2 database.

4.2.3 *In situ* powder X-ray diffraction (in situ PXRD)

In situ powder X-ray diffraction (*in situ* PXRD) was used to study the bulk phase changes of the catalysts prepared from the oxide phase to the metallic phase during reduction. These experiments were carried out using an in-house developed *in situ* PXRD capillary cell (Claeys & Fischer, 2013, Fischer *et al.*, 2014) whose schematic is provided in Figure 4.1. The capillary reactors chosen were made of borosilicate (Capillary Tube Supplies Ltd, UK), 75 mm in length and had an outer diameter and wall thickness of 1 mm and 0.02 mm, respectively. The catalyst bed was loaded into the middle of the capillary and supported by glass wool on either side of the bed. The catalyst bed length was limited to approximately 15 mm to ensure that the catalyst remained in the isothermal zone of the reactor (Clapham, 2012). To monitor the temperature during reduction, an internal thermocouple (Omega, UK) was used. The thermocouple was 0.5 mm in diameter and was placed inside the capillary in such a way that its tip was in contact with the catalyst bed but did not interfere with the X-rays from the XRD. To improve temperature control in the reactor, a heat shield made of a polyimide film (Kapton, Du Pont) mounted on a stainless steel shield was placed above the reactor (Clapham, 2012). The shield is also designed in a way to ensure that it did not interfere with the X-rays.

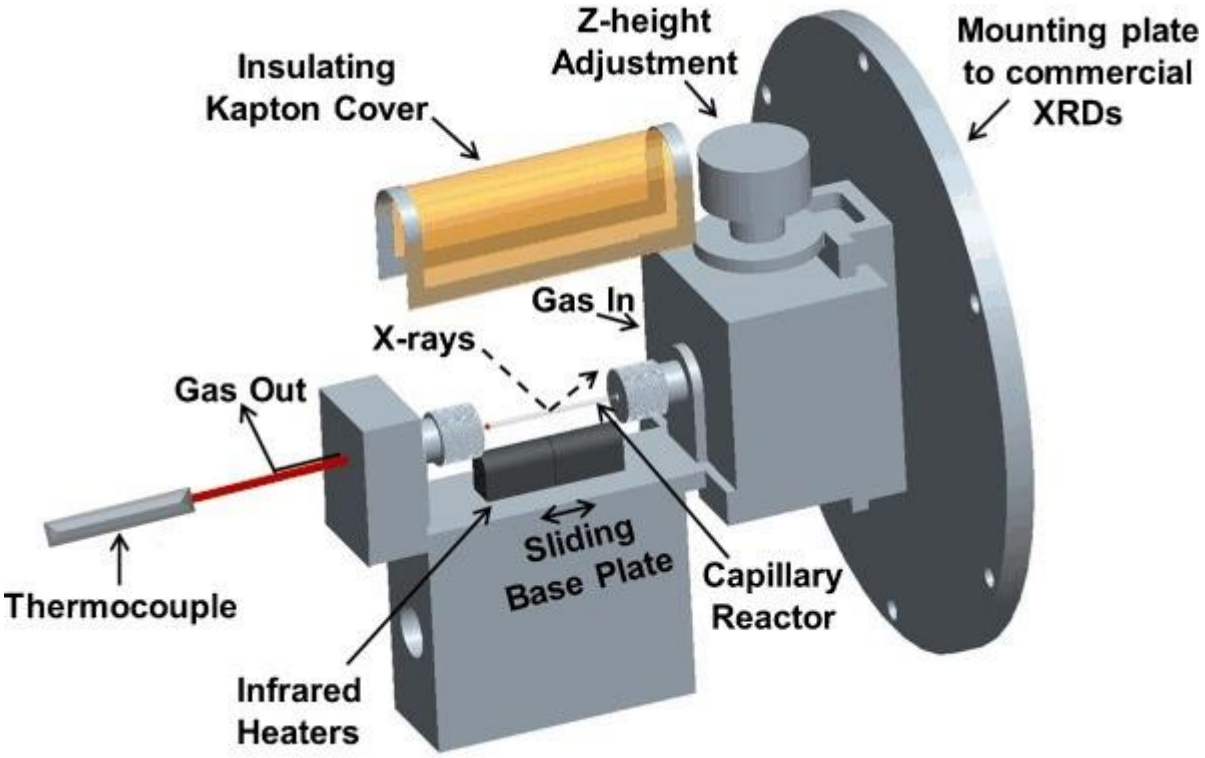

Figure 4.1: Schematic of the in-house developed in situ PXRD capillary cell [From (Fischer et al., 2014)]

The *in situ* PXRD cell was mounted on a Bruker D8 advance X-ray diffractometer equipped with a Bruker AXS Vantec position sensitive detector and a molybdenum source (λ=0.70930 Å). In the experiments, the X-ray diffractometer was operated at 42 kV and 35 mA. A scan range of 15° < 2θ < 30° with a step size of 0.01854° and a time per step of 0.2 s were chosen resulting in a single scan time of 4 minutes and 2 seconds. A delay time of 48 seconds was applied to each scan leading to a total scan time of 5 minutes per scan. In the experiments, the temperature was raised from 50 °C to 450 °C at a ramp rate of 1 °C/min after which the temperature was held constant at 450 °C for 2 hours. The experiments were all carried out under H_2 flow with scans being taken throughout the experiments.

4.2.4 Transmission electron microscopy (TEM)

Transmission electron microscopy (TEM) images of the supports prepared as well as the supported metal catalysts before and after catalyst testing were taken to study their morphology. The images were taken through either a FEI Tecnai F20 TEM equipped with a field emission gun or a FEI T20 TEM equipped with a LaB6 emitter. Both instruments were operated at 200 kV. To prepare the samples for analysis, they

were first crushed with a mortar and pestle before being suspended in ethanol. A few droplets of the suspension were then deposited onto a carbon coated copper grid. The grids were left to dry before analysis was carried out.

4.2.5 High-resolution scanning transmission electron microscopy (HR-STEM)

High-resolution scanning transmission electron microscopy (HR-STEM) images of the Ni-Co(50:50) catalyst were obtained using a JEOL JEM-ARM200F double Cs-corrected TEM at Nelson Mandela University (NMU). The instrument was operated at 200 kV and equipped with a field emission gun, a high angle annular dark field (HAADF) detector and an Oxford XMax 100 TLE (Energy dispersive X-ray spectroscopy) EDX detector. The HAADF images were useful in distinguishing the active metal from the support because of the contrast provided which was difficult to accomplish with conventional TEM analysis. In addition, the Oxford XMax 100 TLE EDX detector enabled elemental analysis to be carried out, to determine how mixed the nickel and cobalt in the catalyst are. To prepare the sample for analysis it was first crushed using a mortar and pestle before being dispersed in ethanol. A few droplets of the suspension were then deposited onto a holey carbon (Quantifoil) grid. The grid was left to dry before analysis was carried out.

4.2.6 Hydrogen temperature programmed reduction (H_2-TPR)

Hydrogen temperature programmed reduction (H_2-TPR) was carried out to determine the reduction behaviour of the catalysts. The analysis was carried out using a Micromeritics AutoChem II 2920 instrument with a quartz U-shaped tube reactor. In the experiments roughly 100 mg of catalyst was loaded into the reactor and then dried for 1 hour at 120 °C in Ar. Afterwards, the temperature was then increased from 60 °C to 900 °C at a rate of 10 °C/min. The heating process was carried out under a gas flow of 50 mL (STP)/min flow of 5 vol % of H_2 in Ar. A thermal conductivity detector (TCD) was used to analyse the consumption of H_2 during the reduction.

4.2.7 Inductively coupled plasma optical emission spectrometry (ICP-OES)

Inductively coupled plasma optical emission spectrometry (ICP-OES) measurements were carried out to determine the nickel to cobalt ratios in the supported metal catalysts that were prepared. These measurements were conducted using a Varian

730 ES ICP-Spectrophotometer instrument. To prepare the samples for analysis, they were first added to 10 mL of aqua regia before being heated at 180 °C for 30 minutes using a MARS-5 microwave digester to digest them. After digestion, the samples were then added to a 25 mL volumetric flask in which they were diluted by adding deionized water. For analysis, the diluted samples were further diluted in 2 wt.% HNO_3 to a dilution factor (DF) of 10 or 100. All the samples were filtered using a 0.2 μm filter before being analysed in the spectrophotometer.

4.2.8 Raman spectroscopy

Raman spectroscopy was carried out in order to analyse the nature of the carbon formed on the surface of the catalysts during catalyst testing. This technique was chosen because of its ability to determine whether the carbon formed is amorphous or graphitic in nature. In addition, carbon is a suitable Raman scatterer which also made the technique ideal for this purpose. This is because this property of carbon ensured that the peaks related to carbon were intense, which simplified the analysis of the spectra. The experiments were carried out using a Witec Confocal Raman Microscope (alpha300) which made use of a 532 nm (green) excitation laser module. During the experiments, the laser power was set between 10 and 20 mW. For data acquisition and processing, the WITec Control FOUR and project FOUR software was used.

4.2.9 Thermogravimetric analysis (TGA)

Thermogravimetric analysis (TGA) was carried out to quantify the amount of carbon that was formed on the catalysts during catalytic testing. The analysis was performed using a Discovery SDT 650 instrument. In the experiments carried out, the samples were added onto alumina pans before the temperature was raised from room temperature to 1000 °C at a rate of 10 °C/min. The heating process was conducted under a gas flow of 30 mL (STP)/min of 21% O_2 in He (air). For data acquisition and processing, the TRIOS software was used.

4.3 Catalyst testing

4.3.1 Test unit and reactor setup

A flow diagram of the test unit used for catalyst testing is given in Figure 4.2. During catalyst testing, CH_4 (Air products, 99.95%), 50% CO_2 in Ar (AFROX) and Ar (Air products, 99.999%) are fed into the test unit using mass flow controllers (MFC) 1, 3 and 2, respectively. The MFC's which are manufactured by Brooks Instruments were all calibrated before use. The gases fed into the test unit from the individual MFC's were all combined into a single line that was connected to a three-way valve (3WV-1) which was used to either direct the gas flow into the dual reactor system or to bypass it. When the gas flow was directed towards the reactors, it first passed through two fused silica columns with equal length. The fused silica columns ensure that the gas flow was split evenly before being fed into the individual reactors. They can achieve this even split as the pressure drop across both columns is the same due to their equal length. The reactors utilised in the test unit were 150 mm in length, had an outer diameter of ¼ inch and can either be made of stainless steel or quartz.

An illustration of one of the reactors is given in Figure 4.3. The catalyst bed was located at the centre in the reactor within the isothermal zone. The catalyst bed was tightly packed with quartz wool on either side of the bed to prevent it from moving outside the isothermal zone. Furthermore, both ends of the catalyst bed were packed with silicon carbide (SiC) and quartz wool. The SiC at the inlet of the reactor also assisted in the preheating of gases entering the reactors. An advantage of the dual reactor setup utilised in the catalyst testing unit is that it has the capability to test two different catalysts under the same conditions in one run. The reactors were heated via an insulated stainless-steel block with 4 cartridges (Thermon South Africa Pty Ltd).

The gas lines exiting the reactor were heated to 80 °C to ensure that no water condensed in the lines before the water traps which were at room temperature. The gas lines exiting the water traps were connected to individual 3/2-way-solenoid valves (A3WV). These were programmed to allow gas flow from only one A3WV at any given time to be sent to an online micro gas chromatogram equipped with a thermal conductivity detector (GC-TCD) for analysis. A gas analysis time interval of 1 hour for each reactor was chosen. After this interval, the A3WVs would automatically change

the reactor being sampled. For example, the A3WVs could be programmed to allow gas from A3WV-1 to be sent to the GC-TCD for sampling for an hour before switching to sample from A3WV-2 in the next hour. During this switching process, the gas flow from the A3WV which was not being analysed by the GC-TCD was sent to the vent.

Before each catalyst test that was carried out, the gas feed that would be used during reaction was first analysed using the online micro-GC-TCD to determine its composition. This was done by directing the gas flow into 3WV-1 away from the line going towards the reactor, hence bypassing it. Three two-way needle valves (2WNV) were installed in series in the bypass line going towards the micro-GC-TCD to mimic the pressure experienced by the gas going through the fused silica columns before being fed to the reactor.

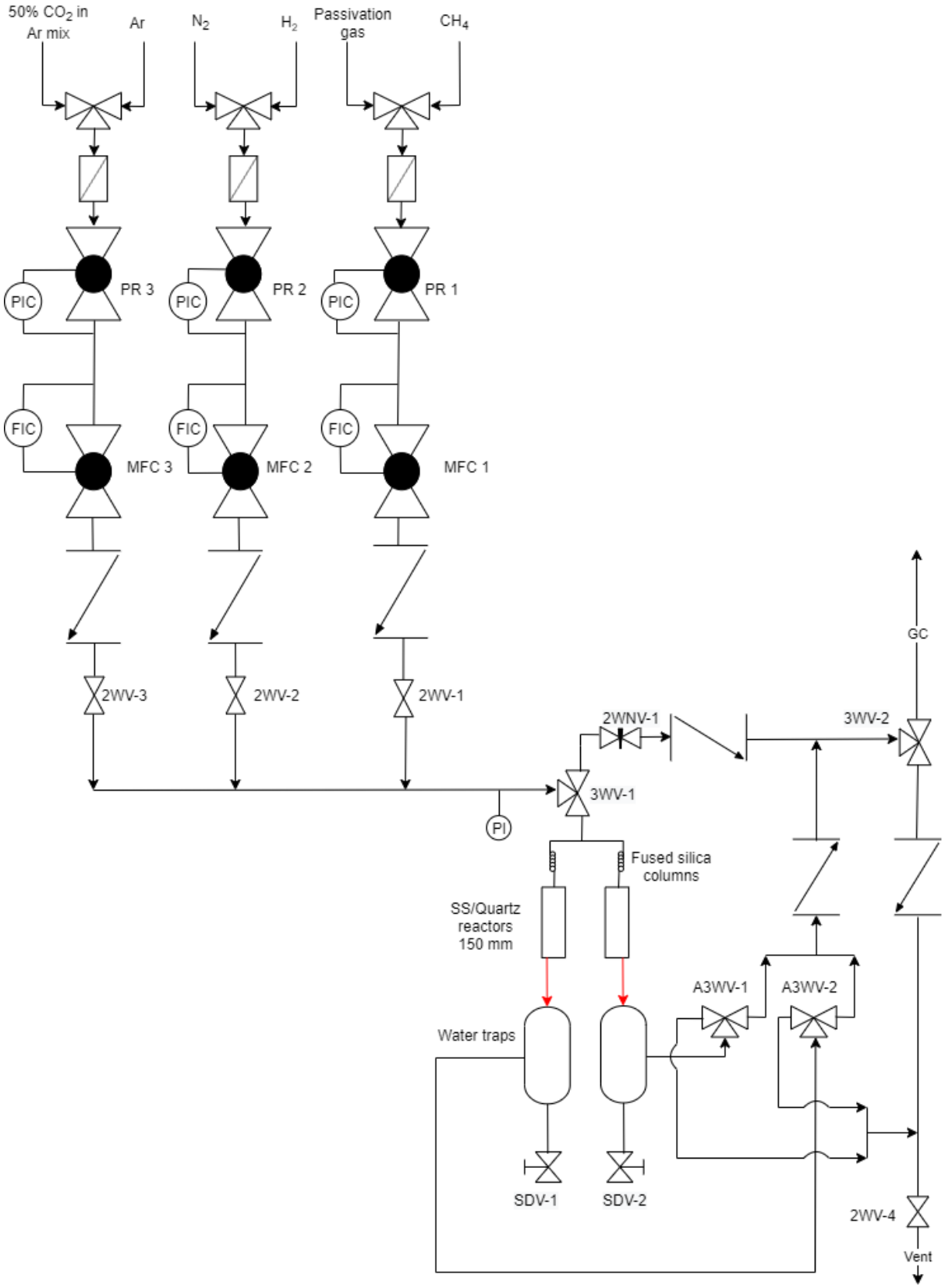

Figure 4.2: Flow diagram of the test unit used for catalyst testing. Red lines represent heated lines.

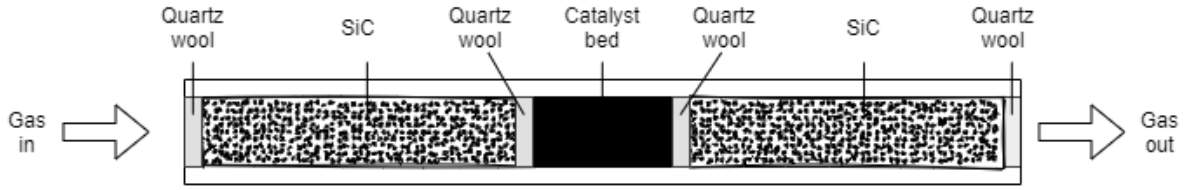

Figure 4.3: Illustration of the reactor used for catalyst testing.

4.3.2 Generalised experimental procedure

In all the catalyst testing carried out, the catalysts were first reduced in 100 mL/min NTP of H_2. In the reduction process, the temperature was raised from room temperature to 700 °C at a rate of 2 °C/min. Once at 700 °C, the temperature was held constant for 2 hours before being allowed to cool to 300 °C. At 300 °C, the gas flow was switched from hydrogen to nitrogen for an hour to flush away any hydrogen that was present on the catalyst surface. This was done to ensure that the catalyst would be kept in an inert atmosphere before the reaction. After the flushing process, the reactor was isolated in this inert atmosphere by ensuring that the gas flow bypassed the reactor. During the period when the reactor was being bypassed, the gas flow was changed from nitrogen to the gases that would be used during the reaction (Ar, CH_4, CO_2). The reactant gases were analysed by the GC-TCD during this time-period in order to obtain information about the gas fed into the reactor, which could then be utilised to carry out conversion calculations. After bypass analysis, the temperature was then raised to the reaction temperature at a rate of 5 °C/min. Once the reaction temperature had been reached, the gas flow containing the reaction mixture was sent to the reactor from the bypass to start the reaction. At the end of the time-period set out for reaction, the reactant gas flows were stopped allowing the reactors to be cooled to room temperature under argon flow. Once at room temperature, the catalysts where then passivated in 1% O_2 in N_2 for one hour. The specific details of the individual catalytic tests carried out will be discussed in the next section.

4.3.3 Specific experimental procedure

The testing conditions for all the catalysts whose performance in the DRM reaction was analysed are summarised in Table 4.2. The first set of catalyst tests carried out focussed on analysing the performance of the catalysts at different reaction temperatures, as well as gauging their long-term stability. These tests were carried out on the Ni-Co(90:10), Ni-Co(50:50) and Ni-Co(10:90) catalysts respectively. The

findings from this first set of tests were then used to choose a single set of conditions that would be ideal to test all the catalysts prepared in the study. The second set of catalyst tests were carried out at the conditions that were deemed ideal from the first tests. The results from the second tests were then used to compare the performance of all the catalysts in the DRM reaction. Specific details about all the catalyst tests that were carried out will be provided below. In all the catalyst tests carried out 30 mg of catalyst was used. The catalyst was also mixed with 30 mg of SiC.

Table 4.2: Testing conditions used for all catalysts tested in the dry reforming of methane reaction

DRM run	Catalyst	Flowrate (mL/min NTP)			Space velocity (mL/g_{cat}-h)	$T_{reaction}$ (°C)	Time (h)
		CH_4	CO_2	Ar			
1.1	Ni-Co(50:50)	20	20	40	160000	600	12
						650	6
1.2	Ni-Co(90:10)	20	20	40	160000	600	12
						650	6
1.3	Ni-Co(50:50)	20	20	40	160000	750	12
						700	12
						750	12
1.4	Ni-Co(90:10)	20	20	40	160000	750	12
						700	12
						750	12
1.5	Ni-Co(10:90)	20	20	40	160000	750	12
						700	12
						650	12
						600	12
						750	12
2.1	Ni(100)	20	20	40	160000	700	12
2.2	Ni-Co(90:10)	20	20	40	160000	700	12
2.3	Ni-Co(70:30)	20	20	40	160000	700	12
2.4	Ni-Co(50:50)	20	20	40	160000	700	12
2.5	Ni-Co(30:70)	20	20	40	160000	700	12
2.6	Ni-Co(10:90)	20	20	40	160000	700	2
2.7	Co(100)	20	20	40	160000	700	12

DRM runs 1.1 and 1.2: Ni-Co(50:50) and Ni-Co(90:10) catalysts

In these catalyst tests, the Ni-Co(50:50) and Ni-Co(90:10) catalysts were tested at 600 °C and 650 °C consecutively. During these runs, the catalysts were tested at each temperature for 12 hours before moving onto the next temperature. However, during these runs a disruption in the CO_2 gas flow which resulted in the amount of CO_2 fed to

the reactor being lower than the desired amount was experienced 6 hours into the catalyst tests at 650 °C. Due to this disruption, it was decided that only the data obtained before the disruption would be considered. In these runs, a 1:1 CH_4:CO_2 feed gas ratio was employed alongside an Ar dilution of 50%.

DRM runs 1.3 and 1.4: Ni-Co(50:50) and Ni-Co(90:10) catalysts

In these catalyst tests, the Ni-Co(50:50) and Ni-Co(90:10) catalysts were tested at 750 °C, 700 °C, and 750 °C consecutively. This was done to obtain data at the temperatures affected by the CO_2 gas flow disruption in DRM Run 1.2 and 1.3, respectively. During these runs, the catalysts were tested at each temperature for 12 hours before moving onto the next temperature. In these runs, a 1:1 CH_4:CO_2 feed gas ratio was employed alongside an Ar dilution of 50%.

DRM run 1.5: Ni-Co(10:90) catalyst

In this catalyst test, the Ni-Co(10:90) catalyst was tested at 750 °C, 700 °C, 650 °C, 600 °C and 750 °C consecutively. During this run, the catalyst was tested at each temperature for 12 hours before moving onto the next temperature. In this run, a 1:1 CH_4:CO_2 feed gas ratio was employed alongside an Ar dilution of 50%.

DRM runs 2.1 – 2.7: All catalysts

Based on the first set of catalyst tests carried out, it was decided that the second set of catalyst tests would be carried out at 700 °C for 12 hours. The results obtained from these tests was then used as a basis to compare the performance of all the catalysts prepared in the DRM reaction. Catalyst testing data for all the catalysts tested with the exception of the Ni-Co(10:90) catalyst (DRM run 2.6) was obtained for the entire 12-hour period. This is because the reactor was blocked due to carbon deposition during the reaction after 2 hours in DRM run 2.6 which meant that the gas product during the run could not be analysed using the online micro-GC-TCD. In all the runs, a 1:1 CH_4:CO_2 feed gas ratio was employed alongside an Ar dilution of 50%.

4.4 Data analysis

The analysis of gases during catalyst testing was carried out using an online micro-GC equipped with a TCD (Agilent 490 Micro GC). The TCD detects gases based on

their differences in thermal conductivity to a carrier gas. The online micro-GC used for analysis had three columns and details about each of these columns as well as the gases that could be analysed in them are given in Table 4.3.

Table 4.3: Detailed information on the micro-GC-TCD used for gas analysis during catalyst testing

Column	Carrier gas	Elutes in order of increasing retention time			
10 m mole sieve (MS5A) Plot	Ar	H_2	CO		
20 m mole sieve (MS5A) Plot	H_2	Ar	N_2	CH_4	CO
10 m PorapakQ	H_2	Mix*	CH_4	CO_2	

*Mixture of Ar, N_2 and CO not retained in the column.

To be able to quantify the amount of gas being eluted from the micro-GC-TCD, it needs to be calibrated using a gas mixture containing known concentrations of the gases that are of interest. This gas mixture should also contain an inert gas whose amount remains constant during the reaction enabling it to act as an internal standard. Based on the calibration gas, individual response factors for each gas with respect to the internal standard can be calculated using Equation (4.1). In the experiments carried out, Ar was chosen as the internal standard. The results of the calibration carried out are available in Appendix A.

$$\boldsymbol{F_x = \frac{n_{Ar} A_x}{A_{Ar} n_x}} \qquad \text{Equation (4.1)}$$

Where, $\boldsymbol{F_x}$ is the response factor of gas $\boldsymbol{x}$ with respect to Ar, $\boldsymbol{A_x}$ and $\boldsymbol{A_{Ar}}$ are the peak areas of gas $\boldsymbol{x}$ and $\boldsymbol{Ar}$ obtained from the GC-TCD data and $\boldsymbol{n_{Ar}}$ and $\boldsymbol{n_x}$ are the molar gas flowrates of $\boldsymbol{Ar}$ and $\boldsymbol{x}$ respectively obtained from the calibration gas.

Once the response factors for the individual gases had been obtained from the calibration, the molar flowrate of each individual gas during the reaction was calculated using Equation (4.2). The response factors calculated are available in Appendix A.

$$\boldsymbol{n_{x,out} = F_x \frac{n_{Ar,in} A_A}{A_{Ar}}} \qquad \text{Equation (4.2)}$$

Where, $\boldsymbol{n_{x,out}}$ is the molar flowrate of gas $\boldsymbol{x}$ exiting the reactor, $\boldsymbol{F_x}$ is the response factor of gas $\boldsymbol{x}$ with respect to Ar, $\boldsymbol{A_x}$ and $\boldsymbol{A_{Ar}}$ are the peak areas of gas $\boldsymbol{x}$ and $\boldsymbol{Ar}$ obtained from the GC-TCD data and $\boldsymbol{n_{Ar}}$ is the molar gas flowrate of $\boldsymbol{Ar}$ which remains constant during the reaction.

Once the molar gas flowrates for each individual gas had been calculated, the conversion of CO_2 ($\boldsymbol{X_{CO_2}}$) and CH_4 ($\boldsymbol{X_{CH_4}}$) were calculated using Equations (4.3) and (4.4) respectively. The H_2/CO ratio which was used as a measure of selectivity was calculated using Equation (4.5).

$$\boldsymbol{X_{CO_2}} = \frac{\boldsymbol{n_{CO_2,in}} - \boldsymbol{n_{CO_2,out}}}{\boldsymbol{n_{CO_2,in}}} \qquad \text{Equation (4.3)}$$

$$\boldsymbol{X_{CH_4}} = \frac{\boldsymbol{n_{CH_4,in}} - \boldsymbol{n_{CH_4,out}}}{\boldsymbol{n_{CH_4,in}}} \qquad \text{Equation (4.4)}$$

$$\frac{\boldsymbol{H_2}}{\boldsymbol{CO}}\ \boldsymbol{ratio} = \frac{\boldsymbol{n_{H_2,out}}}{\boldsymbol{n_{CO,out}}} \qquad \text{Equation (4.5)}$$

Where $\boldsymbol{n_{CO_2,in}}$ and $\boldsymbol{n_{CH_4,in}}$ are the molar gas flowrates of CO_2 and CH_4 fed into the reactor, $\boldsymbol{n_{CO_2,out}}$, $\boldsymbol{n_{CH_4,out}}$, $\boldsymbol{n_{H_2,out}}$ and $\boldsymbol{n_{CO,out}}$ are the molar gas flowrates of CO_2, CH_4, H_2 and CO exiting the reactor.

4.5 Thermodynamic analysis

To complement the catalyst testing that was carried out, a thermodynamic analysis of the DRM reaction as well as the side reactions that can occur alongside it was carried out. For this analysis, two approaches were followed, namely the use of equilibrium constants (K_a's) and the use of direct minimisation of the Gibbs free energy of the system. The main difference between these two approaches is the viewpoint from which chemical equilibrium is calculated. In the K_a's approach chemical reactions are considered whilst in the direct minimisation of Gibbs free energy, a system of compounds is considered. More detailed information on the two approaches is available in Section 2.2 of the literature review.

4.5.1 Equilibrium constant (K_a) approach

The first step in calculating chemical equilibrium using the K_a approach was to determine the Gibbs free energy of the chemical reaction ($\boldsymbol{\Delta G_{rxn}}$) at the temperature of interest ($\boldsymbol{T}$). This was done by making use of the Gibbs-Helmholtz equation which is given in Equation (4.6). The equation can be further simplified through the separation of variables and integration to the form given in Equation (4.7). In these calculations the reference state temperature ($\boldsymbol{T_0}$) and pressure were chosen to be 25 °C and 1 bar, respectively. This choice was influenced by the availability of tabulated data for the Gibbs free energy and enthalpy of formation ($\boldsymbol{\Delta G_f}$) and ($\boldsymbol{\Delta H_f}$) at this reference state. Having this data available was beneficial as it simplified the calculation of Gibbs free energy and enthalpy of reaction ($\boldsymbol{\Delta G_{rxn}(T_0)}$) and ($\boldsymbol{\Delta H_{rxn}\,(T_0)}$) at the reference state. The enthalpy of reaction at the temperature of interest ($\boldsymbol{\Delta H_{rxn}(T)}$) which is required in calculating $\boldsymbol{\Delta G_{rxn}}$ was calculated using Equation (4.8). The heat capacity of the reaction ($\boldsymbol{\Delta C_{p_{rxn}}}$) which accounts for the temperature dependency of $\boldsymbol{\Delta H_{rxn}}$ was determined using Equation (4.9). In Equation (4.9), the coefficients $\boldsymbol{\Delta a_{rxn}}$, $\boldsymbol{\Delta b_{rxn}}$, $\boldsymbol{\Delta c_{rxn}}$ and $\boldsymbol{\Delta d_{rxn}}$ represent heat capacity constants for the reaction. These were calculated by multiplying the individual heat capacity coefficients of each compound in the specific reaction by its stochiometric coefficient. Once $\boldsymbol{\Delta G_{rxn}(T)}$, had been calculated, the K_a for the reaction was determined using Equation (4.10). The thermodynamic data used in the calculations discussed in this section was obtained from (Elliott & Lira, 2012)

$$\frac{\partial\left(\frac{\Delta G_{rxn}}{T}\right)}{\partial T} = -\frac{\Delta H_{rxn}}{T^2} \qquad \text{Equation (4.6)}$$

$$\frac{\Delta G_{rxn}(T)}{T} - \frac{\Delta G_{rxn}(T_0)}{T_0} = \int_{T_0}^{T} -\frac{\Delta H_{rxn}(T)}{T^2}\, dT \qquad \text{Equation (4.7)}$$

$$\Delta H_{rxn}(T) = \Delta H_{rxn}(T_0) + \int_{T_0}^{T} \Delta C_{p_{rxn}}\, dT \qquad \text{Equation (4.8)}$$

$$\Delta C_{p_{rxn}} = \Delta a_{rxn} + \Delta b_{rxn} T + \Delta c_{rxn} T^2 + \Delta d_{rxn} T^3 \qquad \text{Equation (4.9)}$$

$$K_a = exp\left(-\frac{\Delta G_{rxn}(T)}{RT}\right)$$ Equation (4.10)

Equation (4.11) provides the relationship between K_a and the partial pressures of the gases involved in a chemical reaction. In this equation y_i represents the mole fraction of each individual gas, P represents the total pressure of the system whilst v_i represents the stochiometric coefficient of each gas in the reaction. An expansion of this equation applied to the DRM reaction is provided on Equation (4.12). The chemical composition at equilibrium at any given temperature for a specific reaction and feed composition can be determined by equating the numerical value of K_a determined from Equation (4.10) to the expression generated for the chemical reaction using Equation (4.11). The equilibrium conversion for the reaction can then be determined from the results of the calculations.

$$K_a = \prod (y_i P)^{v_i}$$ Equation (4.11)

$$K_a = \frac{(y_{CO}P)^2 \left(y_{H_2}P\right)^2}{(y_{CH_4}P)(y_{CO_2}P)}$$ Equation (4.12)

4.5.2 Direct minimisation of Gibbs free energy approach

In the direct minimisation of Gibbs free energy approach, the total Gibbs free energy of the system (ΔG^{system}) was first determined using Equation (4.13). In Equation (4.13), n_i represent the number of moles of whilst μ_i represents the chemical potential of species (i). Equation (4.14) provides the expression from which μ_i can be calculated. In this equation, $\bar{f}_i$ and f_i^0 represents the partial and standard state fugacities of the species whilst $\Delta G_f(T)$ represents the Gibbs free energy of formation. Equation (4.15) provides an expression expanding on $\bar{f}_i$ in which y_i represents the mole fraction of each individual species, P represents the total pressure of the system whilst φ_i represents the fugacity coefficient, which can be taken to be 1 if the gasses behave like ideal gasses. $\Delta G_f(T)$ was calculated using the same method used to calculate $\Delta G_{rxn}(T)$ from the Gibbs-Helmholtz equation which was outlined in the K_a approach. The only difference was that $\Delta G_f(T)$ was calculated for individual species rather whilst $\Delta G_{rxn}(T)$ was calculated for specific reactions. Once the expression for

$\boldsymbol{\Delta G^{system}}$ had been generated, a feed composition was chosen based on which $\boldsymbol{\Delta G^{system}}$ was minimised. In the minimisation calculations, elemental balances based on the species in the systems and the feed composition were used as a constraint for the chemical equilibrium that was calculated.

$$\boldsymbol{\Delta G^{system}} = \sum \boldsymbol{n_i \mu_i} \qquad \text{Equation (4.13)}$$

$$\boldsymbol{\mu_i} = \boldsymbol{\Delta G_f}(\boldsymbol{T}) + \boldsymbol{RTln}\frac{\bar{\boldsymbol{f}}_{\boldsymbol{\iota}}}{\boldsymbol{f_i^0}} \qquad \text{Equation (4.14)}$$

$$\bar{\boldsymbol{f}}_{\boldsymbol{\iota}} = \boldsymbol{y_i \varphi_i P} \qquad \text{Equation (4.15)}$$

5 Fresh catalyst characterization results

5.1 Powder X-ray diffraction (PXRD)

5.1.1 Magnesium aluminate ($MgAl_2O_4$) support

Powder X-ray diffraction (PXRD) was used to determine the crystalline phases that were present after the drying and calcination processes during the preparation of the catalyst support. The PXRD patterns obtained after the drying and calcination processes are provided in Figure 5.1. From Figure 5.1, it is clear that the phase that is present after the drying process during the preparation of the support is magnesium aluminium hydroxide ($MgAl_2(OH)_8$). This is understandable because the dried sample was obtained from the precipitation of magnesium and aluminium ions which were in solution using ammonia solution (NH_4OH). This dried sample was then calcined in an air atmosphere to form the magnesium aluminate ($MgAl_2O_4$) support. Figure 5.1 also shows that the calcination process was successful because the crystalline phase present after it matches the reference pattern obtained for $MgAl_2O_4$.

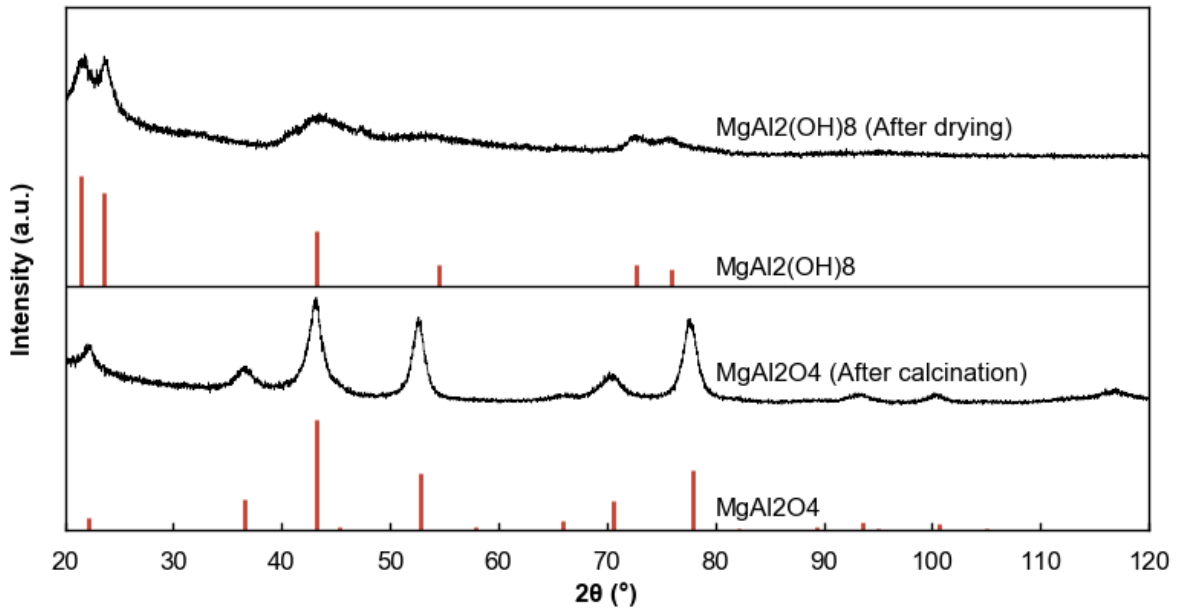

Figure 5.1: PXRD patterns obtained during catalyst support preparation for $MgAl_2(OH)_8$ (after drying) and $MgAl_2O_4$ (after calcination). Reference patterns for $MgAl_2(OH)_8$ and $MgAl_2O_4$ are also provided in red

Since the amount of catalyst support that was required to prepare all the supported metal catalysts required for the study could not be made in a single batch, numerous batches were prepared. The PXRD patterns obtained for the individual batches is provided in Figure 5.2. From Figure 5.2, it was determined that the crystalline phase

present in the individual batches was $MgAl_2O_4$. This also shows that the method used in the preparation of the catalyst support was reproducible.

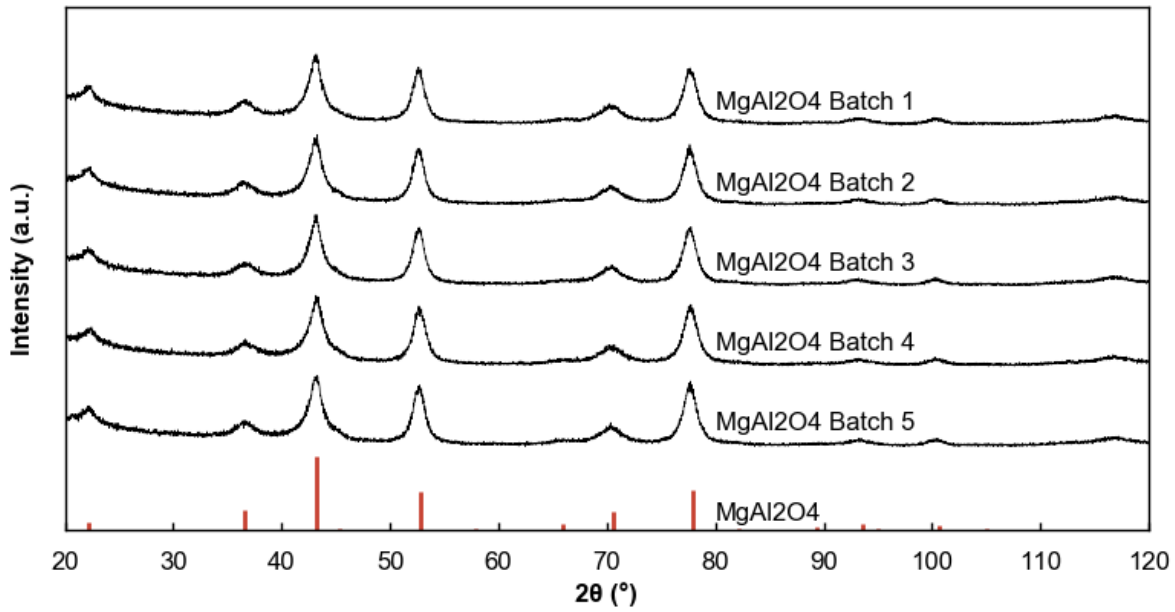

Figure 5.2: PXRD patterns obtained for the different batches of $MgAl_2O_4$. Reference pattern for $MgAl_2O_4$ is also provided in red

5.1.2 Supported nickel-cobalt (Ni-Co) catalysts

After the preparation of the $MgAl_2O_4$ support, nickel and cobalt were added to the support via slurry impregnation before calcination to prepare the supported metal catalyst required for the study. The active metal on the supported metal catalysts was in the form of metal oxides following the calcination step. A comprehensive list of the catalysts prepared, and their compositions is available in Table 4.1. PXRD patterns obtained for the pure cobalt (Co(100)) and pure nickel (Ni(100)) supported metal catalysts are provided in Figure 5.3. From the Ni(100) PXRD pattern in Figure 5.3, the presence of nickel oxide (NiO) in the supported metal catalyst was determined from the shoulder peaks at 2θ values of around 50° and 75°. These peaks correspond to the NiO reference. However, the presence of the cobalt (II, III) oxide (Co_3O_4) phase in the Co(100) supported metal catalyst could not be determined through PXRD as shown in Figure 5.3. This is because both Co_3O_4 and the $MgAl_2O_4$ support are both spinel structures having peaks at similar 2θ values. This can be illustrated by their references which are provided in Figure 5.3.

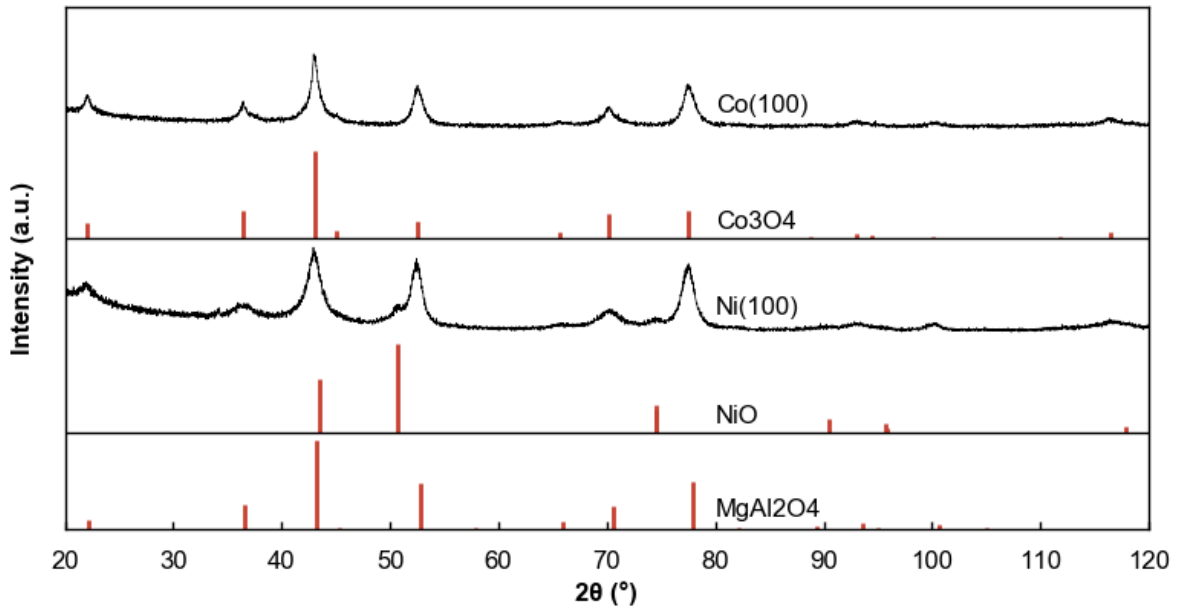

Figure 5.3: PXRD patterns obtained after the preparation of the pure cobalt (named Co(100)) and the pure nickel (named Ni(100)) supported metal catalysts. Reference patterns for Co_3O_4, NiO and $MgAl_2O_4$ are also provided in red

The PXRD patterns obtained for the bimetallic nickel-cobalt (Ni-Co) catalysts of varying Ni:Co ratios are provided in Figure 5.4. From Figure 5.4, the presence of nickel and cobalt on the Ni-Co catalysts could not be determined through PXRD as was the case for the Co(100) catalyst. The reason behind this is that the nickel cobalt oxide ($NiCo_2O_4$) that is expected to be formed in the Ni-Co catalysts after calcination is also a spinel structure. This makes it makes it difficult to distinguish from the $MgAl_2O_4$ support, which is also a spinel structure. Additionally, the PXRD patterns for the Ni-Co samples do not have the shoulder peaks at 2θ values of around 50° and 75° associated with the NiO as was the case in the Ni(100) sample. This could be because the amount of it that could possibly form, especially in the nickel rich catalysts, was reduced because of the concurrent formation of the $NiCo_2O_4$ phase. This would make its detection via PXRD more difficult as its peaks would have a lower intensity.

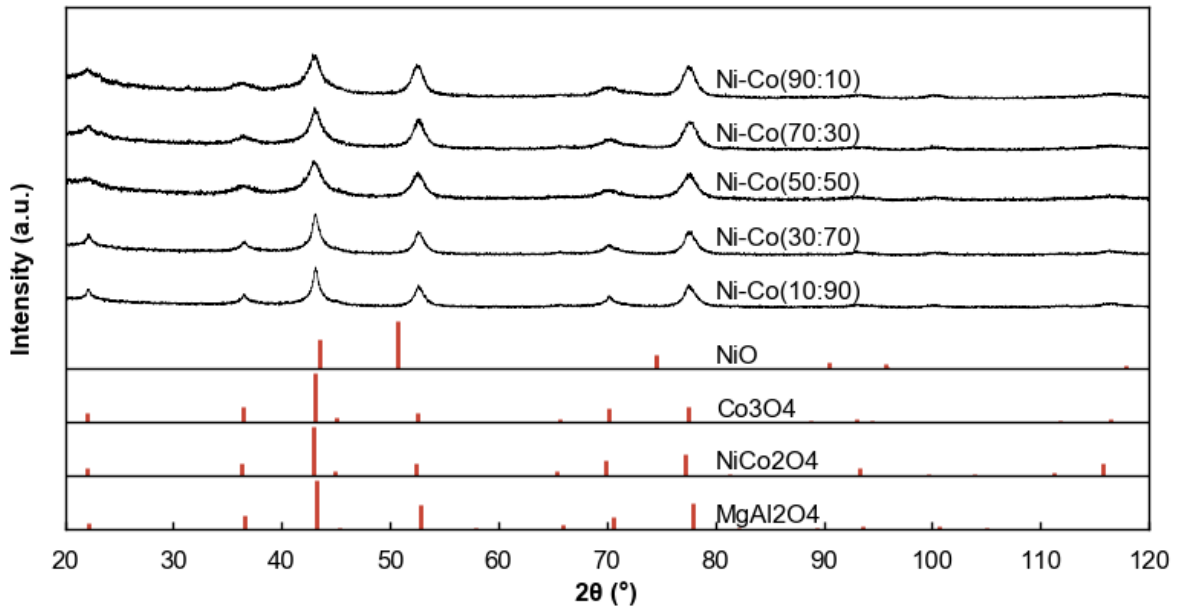

Figure 5.4: PXRD patterns obtained after the preparation of the Ni-Co(90:10), Ni-Co(70:30), Ni-Co(50:50), Ni-Co(30:70) and Ni-Co(10:90) supported metal catalysts. Reference patterns for NiO, Co_3O_4, $NiCo2O_4$ and $MgAl_2O_4$ are also provided in red

5.2 Transmission electron microscopy (TEM)

Transmission electron microscopy (TEM) was carried out to study the morphology of the unreduced catalysts. TEM images of the $MgAl_2O_4$ support, Ni-Co(50:50) catalyst, Co(100) catalyst and Ni(100) catalyst are provided in Figure 5.5, labelled A, B, C and D respectively. From the TEM images obtained, it can be seen that the support material and the catalyst samples where active metal had been deposited look very similar. This was due to the poor contrast between the support and the active metal. However, in the samples containing active metal, more darker regions were observed which likely signalled the presence of the active metal in those catalyst samples. Due to the poor contrast between the catalyst support and the active metal, size information for the active metal deposited on the support could not be obtained from the TEM images. Although size information could not be obtained from the images, it must be noted that the crystallite sizes based on the images taken were similar hence it was assumed that similar crystallite sizes were present in all the catalysts.

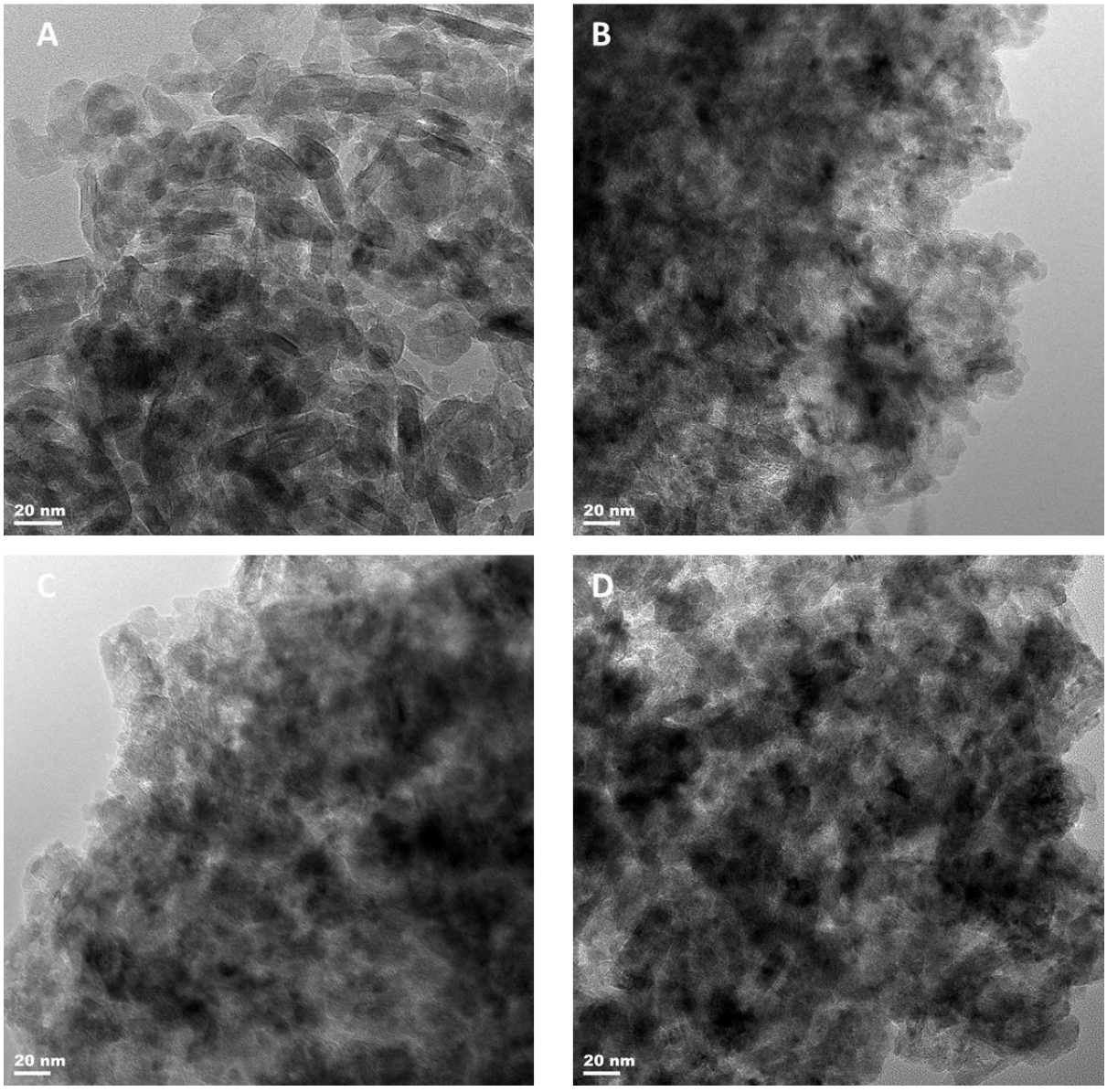

Figure 5.5: TEM images of $MgAl_2O_4$ support (A), Ni-Co(50:50) catalyst (B), Co(100) catalyst (C) and Ni(100) catalyst (D)

5.3 High-resolution scanning transmission electron microscopy (HR-STEM)

High-resolution scanning transmission electron microscopy (HR-STEM) was used to analyse a reduced sample of the Ni-Co(50:50) catalyst. Prior to the analysis, the Ni-Co(50:50) catalyst was reduced in hydrogen for 2 hours at 700 °C before being passivated in 1% O_2 in Ar for 1 hour at room temperature. Some images obtained from the HR-STEM analysis carried out are provided in Figure 5.6. In Figure 5.6, bright field images (images A – D) and their corresponding high angle annular dark field (HAADF) images (images E – H) are provided. The HAADF images were very useful in determining the presence of nickel and cobalt on the support because of the improved contrast that they provided. This distinction could not easily be made based on the

TEM analysis that was carried out, so the HR-STEM analysis proved to be complementary in this regard. Unfortunately, this analysis could not be carried out for all the catalysts.

From images E and F, it was determined that good dispersion was achieved in the catalyst. This conclusion was reached on the basis that most of the support was bright, contrasted by the darker active metal on it. Images C and D which focussed on individual Ni-Co particles showed that these particles were between 10 – 20 nm in size. This provided the best estimate of the potential Ni-Co average particle size as there weren't enough images to make a better estimation.

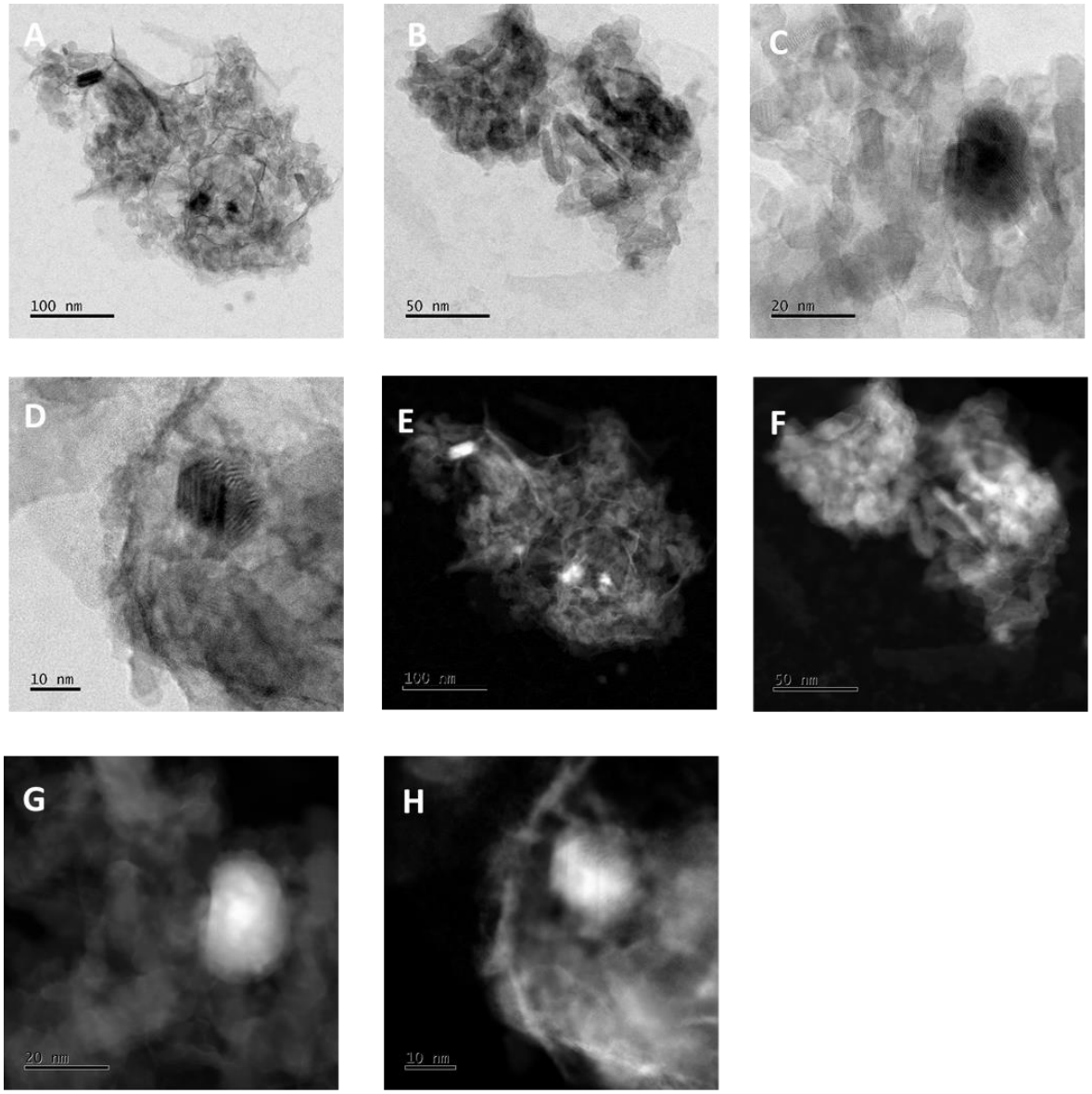

Figure 5.6: High resolution scanning transmission electron microscopy (HR-STEM) images of a reduced sample of the Ni-Co(50:50) catalyst. A - D are bright field images whilst E - H are HAADF images.

In addition, HR-STEM energy dispersive X-ray spectroscopy (EDX) mapping was also carried out to determine whether the cobalt and nickel were well mixed. A HR-STEM EDX map obtained during the analysis of the Ni-Co(50:50) catalyst is provided in Figure 5.7. From Figure 5.7, it can be seen that in the area analysed, nickel and cobalt are well mixed. This can be confirmed by the signal distribution of cobalt and nickel provided in images B and C being similar.

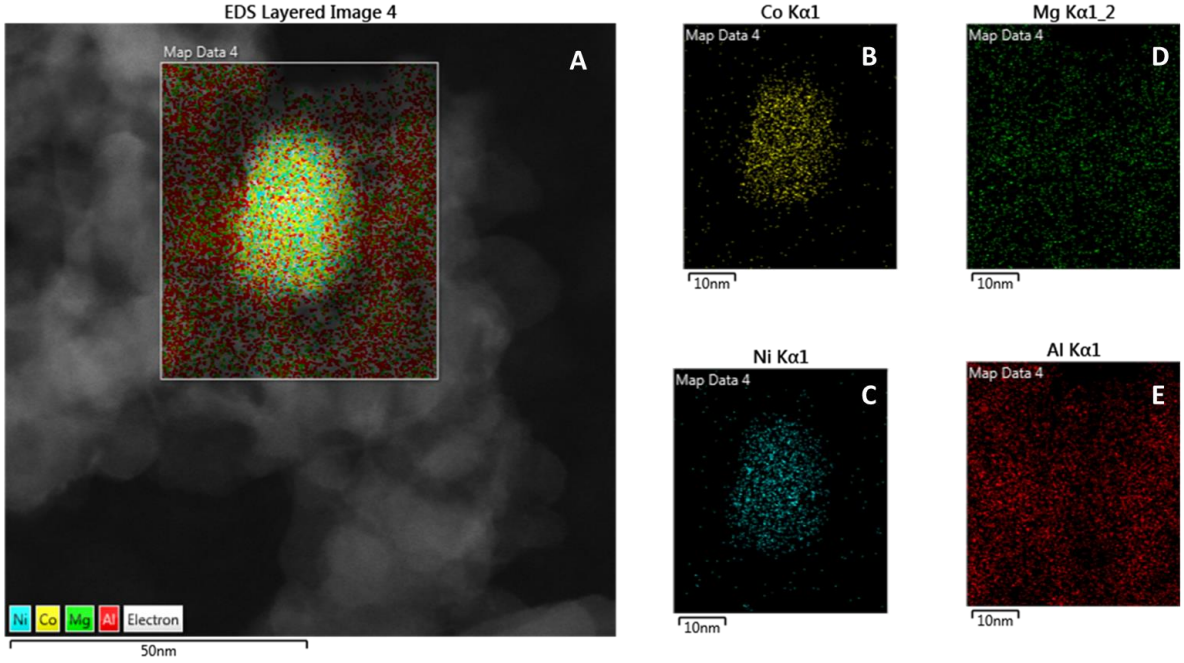

Figure 5.7: HR-STEM EDX maps for a reduced sample of the Ni-Co(50:50) catalyst where: A is a HAADF image of the reduced Ni-Co(50:50) catalyst with a colour composite map of Co, Ni, Mg and Al, B is the Co signal distribution, C is the Ni signal distrubution, D is the Mg signal distrubution and E is the Al signal distrubution

5.4 Brunauer–Emmett–Teller (BET) analysis

Brunauer–Emmett–Teller (BET) analysis was carried out to determine the BET surface area, pore volume and average pore diameter for the $MgAl_2O_4$ support as well as all the unreduced supported metal catalysts prepared for the study. The results obtained from this analysis are summarised in Table 5.1. From the results, it was determined that the addition of active metal to the $MgAl_2O_4$ support resulted in a decrease in the BET surface area. In addition, a trend was also observed whereby the nickel rich catalysts were found to have lower BET surface areas in comparison to their cobalt rich counterparts. A similar trend was also observed for the pore volume as the nickel rich catalysts with the exception of the Ni-Co(70:30) catalysts had lower pore volumes

compared to the cobalt rich catalysts. The nitrogen adsorption-desorption isotherms for all the catalysts are available in Appendix B. These isotherms showed that all the catalysts had type IV isotherms.

No trend was observed in terms of the average pore diameter as the values obtained for the catalysts were similar except for the Ni-Co(50:50) catalyst, which had the lowest pore diameter of all prepared catalysts. The supported catalysts were prepared *via* slurry impregnation, implying that the solution containing the metal precursors (for Ni and Co) could end up inside and outside the pores of the support. The observed decrease in the pore diameter after slurry impregnation indicates that some particles formed/grew inside the pores of the support during the drying and calcination processes. For the Ni-Co(50:50) catalyst, it is possible that a relatively large fraction of the Ni-Co oxide particles formed inside the pores of the support, leading to a supported catalyst with the lowest average pore diameter. Although reliable size information could not be obtained from XRD and TEM (Sections 5.1 and 5.2), we further propose that the large fraction of the Ni-Co oxide particles located inside the pores are smaller than 15.5 nm, which is the average pore diameter of the bare support. All the catalysts, as well as the $MgAl_2O_4$ support, were found to have meso-pores as their average pore diameters were between 2 nm to 50 nm. The pore size distributions of all the catalysts are also available in Appendix B.

Table 5.1: Summary of results obtained from BET analysis on the catalyst support as well as supported metal catalysts used in the study

Catalyst	BET surface area (m^2/g)	Pore volume (cm^3/g)	Average pore diameter (nm)
$MgAl_2O_4$	100.4	0.415	15.5
Ni(100)	69.3	0.236	12.9
Ni-Co(90:10)	61.6	0.225	13.5
Ni-Co(70:30)	68.4	0.303	15.7
Ni-Co(50:50)	89.5	0.253	10.5
Ni-Co(30:70)	80.6	0.253	14.8
Ni-Co(10:90)	85.7	0.357	14.5
Co(100)	90.1	0.337	13.9

5.5 Inductively coupled plasma optical emission spectrometry (ICP-OES)

Inductively coupled plasma optical emission spectrometry (ICP-OES) was used to determine the active metal loading as well as the Ni:Co ratios of the supported metal

catalysts that were prepared. A summary of the results obtained is provided in Table 5.2. From the results, it was determined that the targeted active metal loading was not achieved in the catalysts prepared as the values obtained were below those targeted. In addition, the nickel rich catalysts had lower active metal loadings compared to the cobalt rich catalysts. The targeted metal loadings are based on the assumption that there is full deposition of the active metal onto the support. Based on the results obtained, it likely that this assumption did not hold. However, the Ni:Co ratios that were obtained for the supported metal catalyst were similar to what was targeted during catalyst synthesis. The Ni-Co(50:50) catalyst was the only exception with respect to the Ni:Co ratio obtained as it ended up having more cobalt than had been targeted.

Table 5.2: ICP-OES results obtained for the supported metal catalyst prepared for the study

Catalyst	Targeted total active metal loading (wt.%)	Actual total active metal loading (wt.%)	Targeted Ni:Co ratio	Actual Ni:Co ratio
Ni(100)	10	7.33	100:0	100:0
Ni-Co(90:10)	10	8.21	90:10	90:10
Ni-Co(70:30)	10	7.49	70:30	69:31
Ni-Co(50:50)	10	9.56	50:50	44:56
Ni-Co(30:70)	10	8.94	30:70	29:71
Ni-Co(10:90)	10	9.48	10:90	9:91
Co(100)	10	9.06	100:0	0:100

5.6 *In situ* powder X-ray diffraction (in situ PXRD)

In situ powder X-ray diffraction (*in situ* PXRD) was used to study the bulk phase changes of the supported metal catalysts that occur during the reduction of the active metal from the oxide phase to the metallic phase. In the *in situ* PXRD studies, the temperature was raised from 50 °C to 450 °C at a rate of 1 °C/min before being held constant at 450 °C for 2 hours. The analysis was carried out under H_2 flow. The on top view of the of the diffraction patterns that were obtained for the Ni(100) reduction is given in Figure 5.8. From Figure 5.8, it was determined that the formation of metallic Ni during the reduction of the Ni(100) catalyst occurred around 350 °C. This change was indicated by the decrease in intensity of the peak at a 2θ value of 17° as well as an increase in intensity in the peak just below a 2θ value of 20°. The simultaneous changes in these two peaks occurred because metallic Ni, unlike the NiO which was the initial phase during the reduction, does not have a peak at a 2θ value of 17°, whilst

its most intense peak lies just above a 2θ value of 20°. Hence when metallic Ni begins to form the peak at a 2θ value of 17 ° disappears whilst the peak at a 2θ value of 20° increases in intensity. The Ni metallic phase has an additional peak near a 2θ of 23° but this was not exactly visible as its intensity was low relative to the rest of the peaks in the diffraction pattern. The Ni-Co(90:10) and Ni-Co(70:30) catalysts, which were nickel rich, displayed similar reduction patterns to the Ni(100) catalyst. The reduction of the Ni-Co(90:10) and Ni-Co(70:30) catalysts into the metallic phase occurred around 400 °C and 350 °C respectively. The results of their characterisation using *in situ* PXRD plots are available in Appendix C.

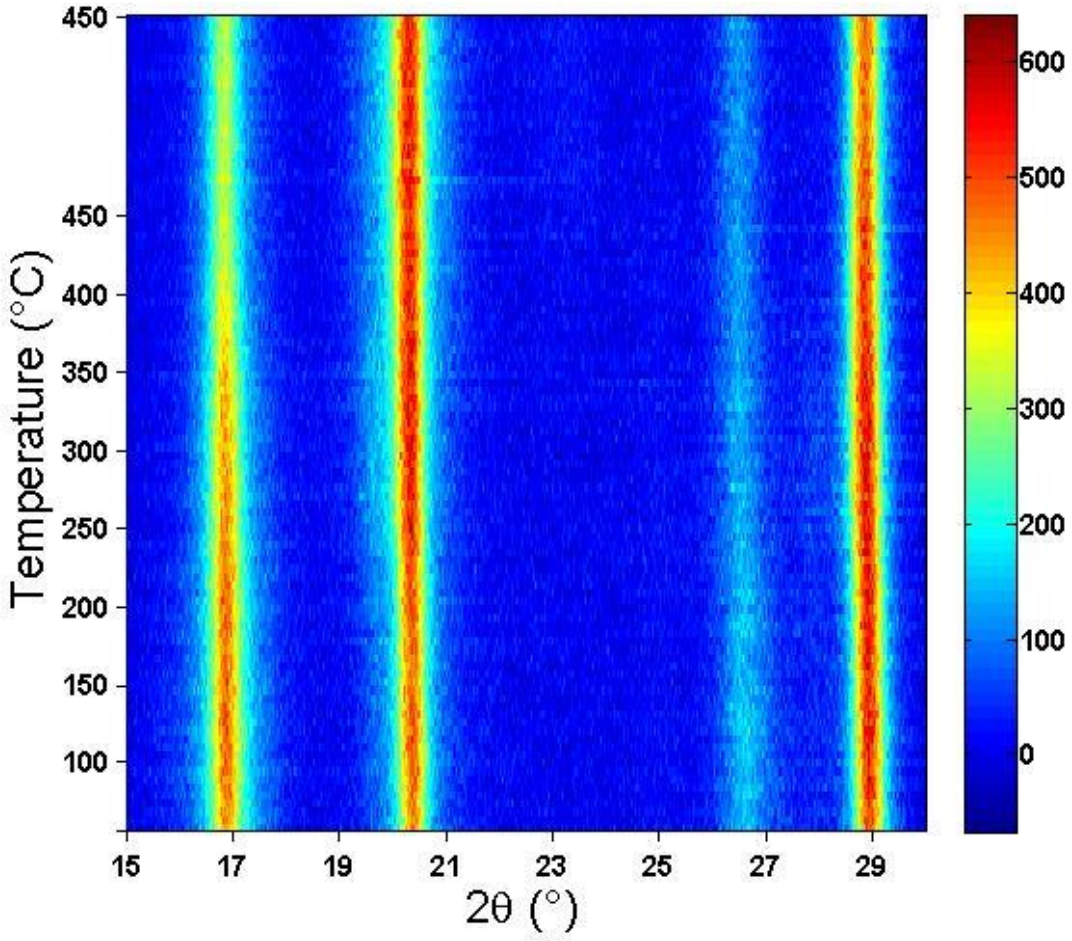

Figure 5.8: On top view of the in situ PXRD patterns obtained during the reduction of the Ni(100) catalyst.

The on top view of the of the diffraction patterns obtained for the Co(100) catalyst during *in situ* PXRD analysis is given in Figure 5.9. From Figure 5.9, it was determined that the reduction of the Co(100) catalyst goes through an intermediate oxide phase, unlike the Ni(100) catalyst. This intermediate oxide phase was determined to be CoO

because of the two peaks that appear at 2θ values just above 19° and 27° around 200 °C which correspond to the CoO reference. The transition from the CoO phase into metallic face centred cubic (fcc) Co was determined to occur below 450 °C when the CoO peaks began to disappear. The Ni-Co(50:50), Ni-Co(70:30) and Ni-Co(90:10) catalysts displayed similar reduction patterns to the Co(100) catalyst, as their reduction passed through an intermediate oxide phase. The onset temperatures for the reduction events that were observed during the experiments carried out are provided in Table 5.3. The *in situ* PXRD characterisation of these catalysts are also available in Appendix C.

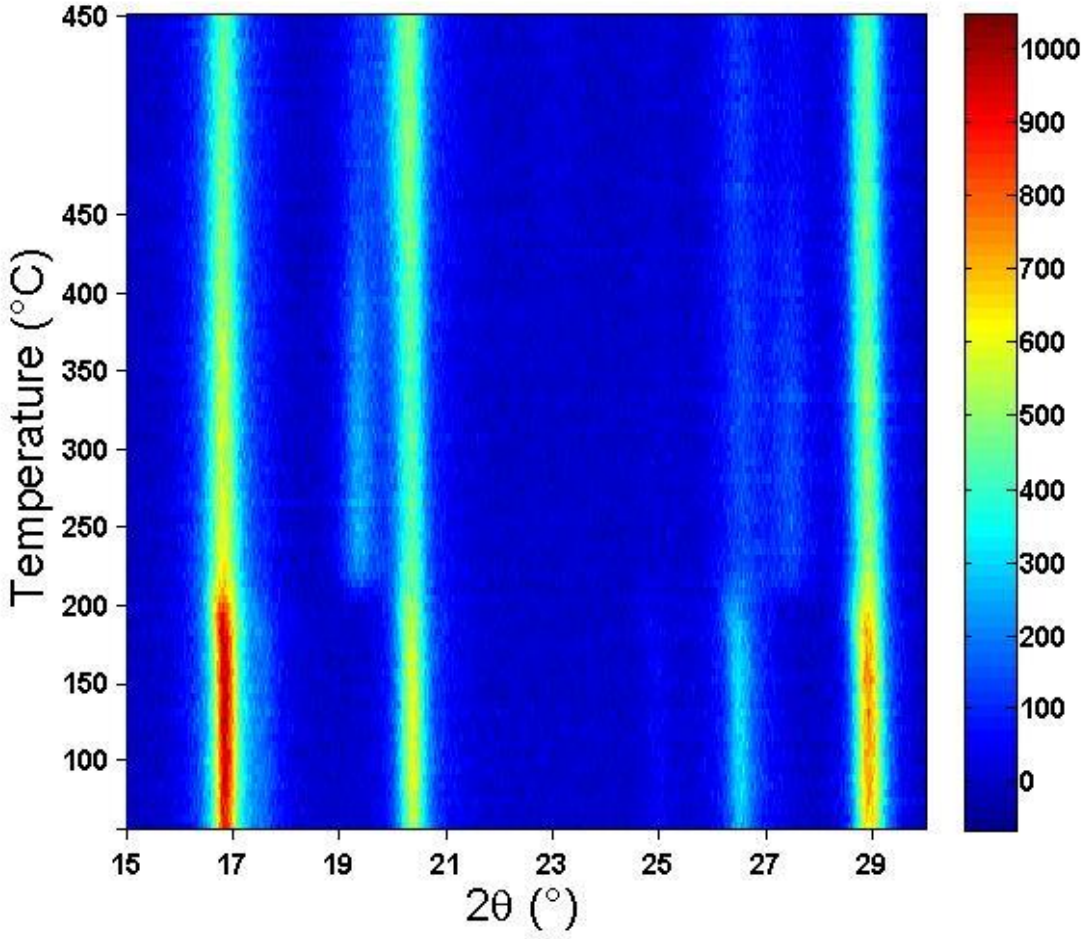

Figure 5.9: On top view of the in situ PXRD patterns obtained during the reduction of the Co(100) catalyst.

Table 5.3: Onset temperature of reduction events for the Ni-Co(50:50), Ni-Co(30:70) and Ni-Co(10:90) catalysts during the in situ PXRD experiments conducted

Catalyst	Onset temperature of reduction into mixed oxide phase	Onset temperature of reduction into metallic phase
Ni-Co(50:50)	200 °C	350 °C
Ni-Co(30:70)	200 °C	400 °C
Ni-Co(10:90)	200 °C	410 °C

5.7 Hydrogen temperature programmed reduction (H_2-TPR)

Hydrogen temperature programmed reduction (H_2-TPR) studies were also carried out on the supported metal catalysts that were prepared to study their reduction behaviour. The results obtained from the H_2-TPR studies are provided in Figure 5.10. From Figure 5.10, it was observed that the reduction of the catalysts occurred in two phases. These two phases were represented by the two sets of peaks observed in the H_2-TPR results. The first of these peaks which was more dominant and occurred just above 200 °C was associated with the reduction of the initial oxide phases present in the catalysts into the metallic phase, as was highlighted by the results obtained from *in situ* XRD studies. From Figure 5.10, it can be seen that the initial reduction peak for the cobalt rich catalysts had a shoulder, whilst those of the nickel rich catalysts did not. The shoulder peak in the cobalt rich samples was an indication that the peak consisted of two peaks representing different phases. This agreed with the *in situ* XRD studies, whereby it was shown that the reduction of the cobalt rich catalysts went through an intermediate oxide phase.

The second reduction peak observed in the H_2-TPR results which occurred above 400 °C was broader, lower in intensity and spanned a wider temperature range. This peak was associated with the reduction oxide particles having strong metal support interactions, which made reduction more difficult. This meant that the reduction temperature needed prior to catalytic testing was required to be high to ensure the complete reduction of these catalysts. Lastly, the onset of reduction for the cobalt rich catalysts was observed to occur at lower temperatures in comparison to the nickel rich catalysts. This is evident from the trends that can be observed from Figure 5.10,

whereby the temperature at which the maxima of the first reduction peak occurred increased with increasing nickel content in the catalysts.

The trends discussed above were found to be applicable for all the catalysts except for the Ni-Co(50:50) catalyst. The Ni-Co(50:50) catalyst was different in that the second reduction peak, occurring at a higher temperature was more dominant than the first one. This result was unexpected because the reduction patterns obtained for this catalyst using *in situ* PXRD were similar to those obtained for the cobalt rich catalysts. To ensure that the results obtained for this catalyst were not anomalous, the experiment was repeated and yielded similar results which are provided in Appendix D.

Although TEM analysis was not conclusive in terms of the size of the Ni-Co oxide particles, the cause of the different reduction behaviour exhibited by the Ni-Co(50:50) catalyst could be related to the catalyst having a wide particle size distribution. Since larger particles are more easily reduced, it is possible that the initial smaller peak seen in the H_2-TPR profile of Ni-Co(50:50) represents the reduction of relatively large particles. The smaller particles were then reduced at a higher temperature, which is represented by the more intense second peak. Based on the previously discussed average pore diameter results in Section 5.4, the second peak could correspond to the reduction of the large fraction of Ni-Co particles located inside the pores of the support. These particles were small in size as their growth was limited by the pore diameter of the support (15.5 nm), which would explain why the second H_2-TPR peak was greater.

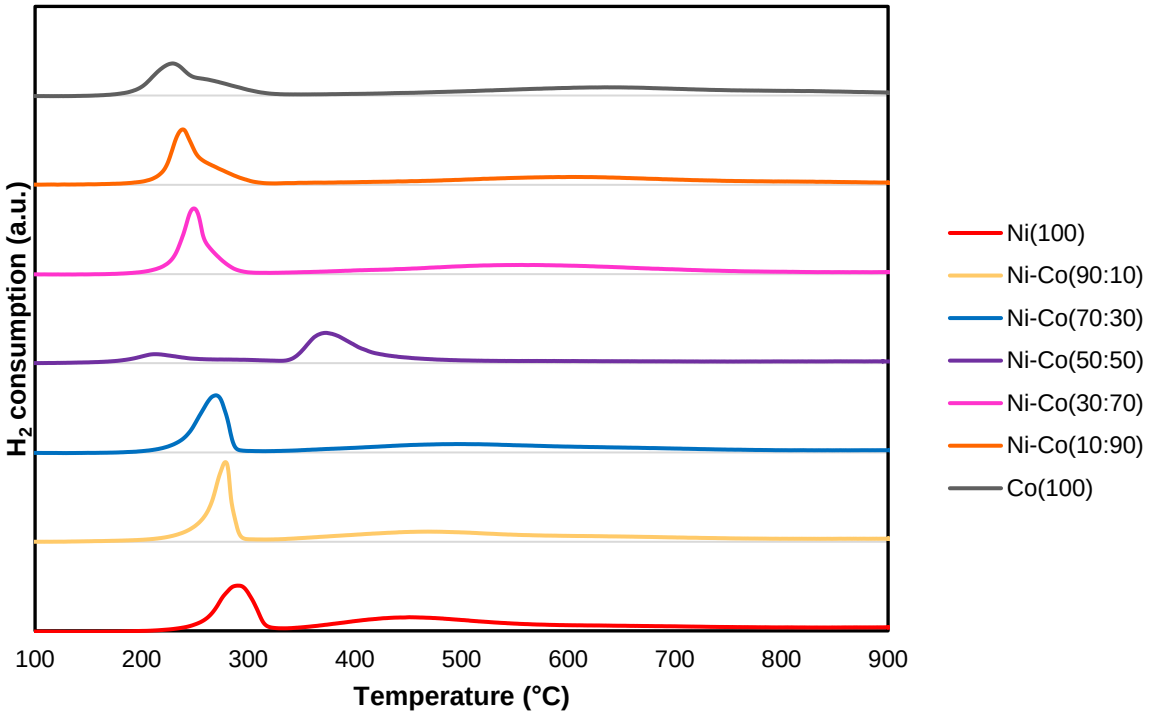

Figure 5.10: H_2-TPR results for the reduction for all the catalysts prepared.

6 Thermodynamic evaluation and catalyst testing results

6.1 Thermodynamic analysis

6.1.1 Equilibrium constant (K_a) approach

The first step that was carried out to determine chemical equilibrium using the equilibrium constant (K_a) approach was to calculate the K_a values of the individual reactions that were considered in the study. For the study, the reactions chosen were DRM, methane cracking, Boudouard, reverse gasification of carbon and the RWGS reactions. The K_a values obtained for the individual reactions are given in Figure 6.1. In Figure 6.1, the K_a values are given as logarithm values to the base 10. This was done to simplify the graphical comparison between the K_a values in the temperature range chosen because they decrease/increase exponentially for the individual reactions. Making this comparison graphically using the actual K_a values would be difficult because the largest values are several orders of higher than the smallest values. This would result in a plot dominated by the largest K_a values. The K_a values were calculated using the methodology outlined in Section 4.5.1.

From Figure 6.1, it was determined that the K_a values decreased with increasing temperature for the exothermic reactions (CO hydrogenation and Boudouard) whilst they increased with increasing temperature for the endothermic reactions (DRM, Methane cracking and RWGS). Since the equilibrium conversion achievable for a reaction increases as the K_a value increases, the results obtained from the calculations were plausible. This is because the K_a values were higher at the temperatures at which the reactions are favoured. Based on the calculated K_a values, it was also concluded that in the temperature range studied, the DRM reaction would be favoured as the temperature was increased. Additionally, the methane cracking and RWGS reactions were deemed to be the side reactions that would most likely compete with the DRM reaction at the temperatures at which it would be favoured.

The trends obtained for the variation of the K_a values with the temperature were also similar to those obtained from the study carried out by Zhang *et al.* (2007). However, there was a difference pertaining to the temperature at which the DRM reaction became more likely than the methane cracking reaction. Zhang *et al.* (2007) predicted that this would occur around 680 °C whilst the results obtained from the study carried

out determined that this would occur just above 700 °C. The methodology followed in the calculations carried out by Zhang *et al.* (2007) was not provided which made it difficult to determine the reasons for the differences in the findings.

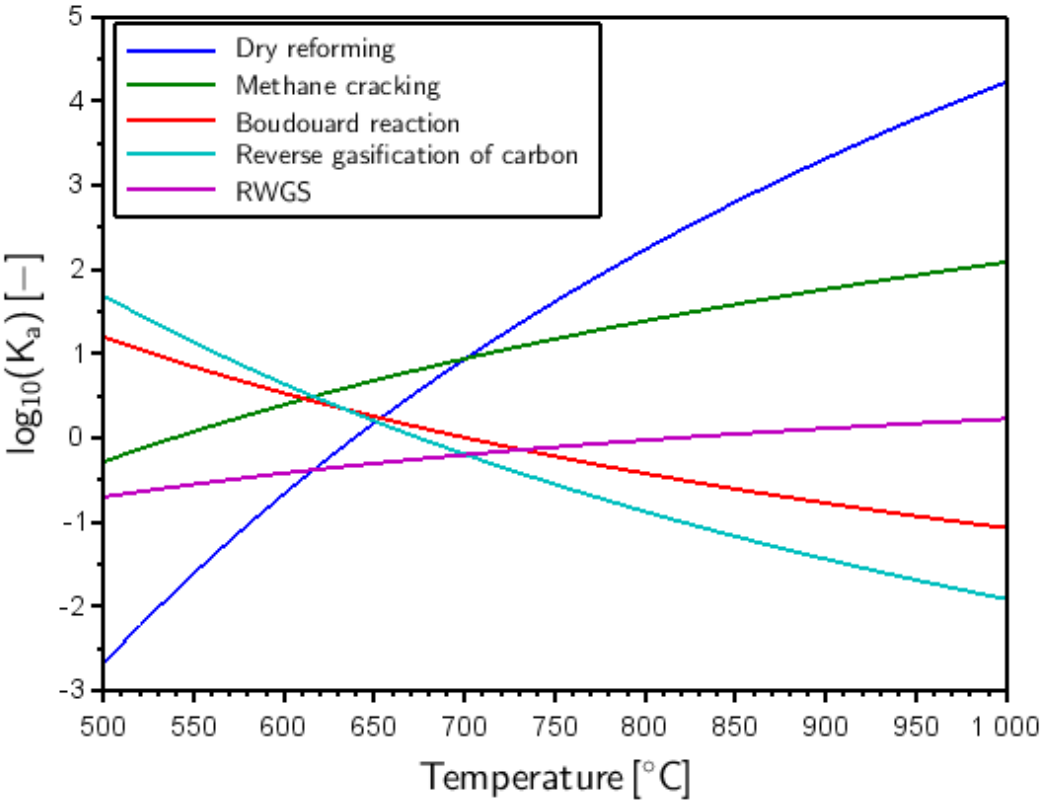

Figure 6.1: Variation of the K_a values with increasing temperature for the reactions considered in the thermodynamic analysis carried out

Once, the K_a values for the reactions to be considered in the study had been determined, the equilibrium conversion (X_{eq}) for the DRM reaction was calculated. This was done to determine the baseline X_{eq} for CO_2 and CH_4 that are achievable in the absence of side reactions. In the calculations, two systems were considered namely: one without feed dilution and another with 50% Ar feed dilution. For the system without dilution, a CH_4:CO_2 molar feed ratio of 1:1 was used whilst for the system with 50% Ar dilution, a CH_4:CO_2:Ar molar feed ratio of 1:1:2 was used. The calculations for both systems were carried out at a pressure of 1.01325 bar. The system in which the feed gas was diluted with 50% Ar was studied to investigate the impact that gas dilution would have on X_{eq} since the feed gas during catalyst testing was diluted by Ar to the same extent. The results obtained from the study are given in Figure 6.2.

From Figure 6.2, it was determined that X_{eq} increased with increasing temperature for the DRM reaction. These results were plausible because of the endothermic nature of the reaction and how the K_a values for the reaction were determined to increase with increasing temperature. On the other hand, dilution was determined to increase X_{eq} for the DRM reaction. The reason for this difference is that dilution changes the partial pressures of the individual gases in the system which are then used to calculate X_{eq}. The values of X_{eq} obtained CO_2 and CH_4 were the same because both reactants have the same stoichiometric coefficients in the DRM reaction.

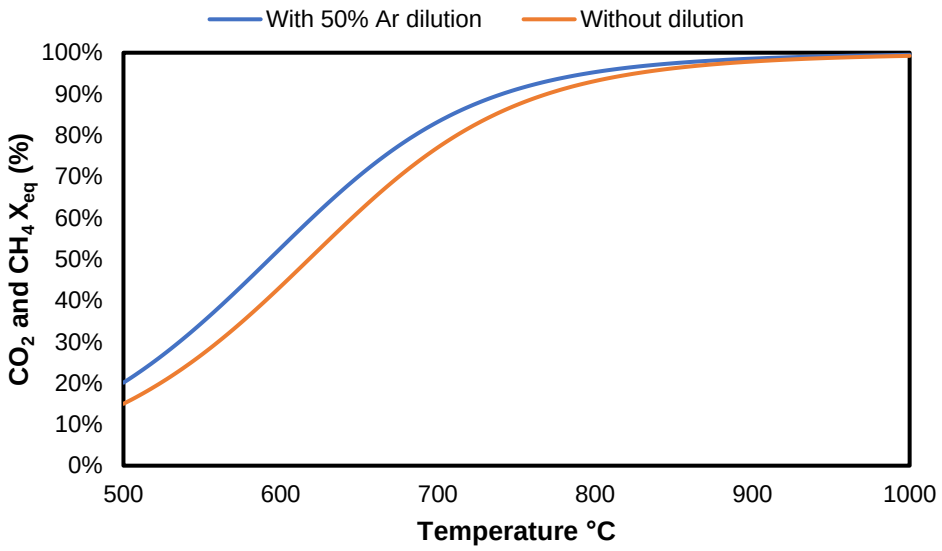

Figure 6.2: Equilibrium conversion for the DRM as a function of temperature at 1.01325 bar. For the system without dilution a CH_4:CO_2 molar feed ratio of 1:1 whilst for the system with 50% Ar dilution a molar feed ratio of CH_4:CO_2:Ar of 1:1:2 was used.

The final step in the thermodynamic analysis carried out using the K_a values was to determine how the number of moles of the compounds in the reactions considered varied with temperature at equilibrium. For this study, two systems were considered namely: one without feed dilution and another with 50% Ar feed dilution. For the system without dilution, a CH_4:CO_2 molar feed ratio of 1:1 was used whilst for the system with 50% Ar dilution, a CH_4:CO_2:Ar molar feed ratio of 1:1:2 was used. The calculations for both systems were carried out at a pressure of 1.01325 bar. The results for the system without feed dilution are given in Figure 6.3 whilst the results for the system with 50% Ar feed dilution are given Figure 6.4.

From the results provided in Figure 6.3 and Figure 6.4, it can be seen that the amount of CH_4 and CO_2 in the systems at equilibrium decreased with increasing temperature. In addition, there was more CO_2 than CH_4 at equilibrium up until 900 °C. These results can partly be explained by the fact that the methane cracking reaction which consumes CH_4 is initially favoured (up until 700 °C) over the DRM reaction which results in there being more CH_4 than CO_2 at equilibrium. Further evidence for the methane cracking reaction being more thermodynamically favourable over the DRM reaction is provided by there being more H_2 than CO at equilibrium. Another reason why there is more CO_2 than CH_4 at equilibrium at lower temperatures is because the Boudouard reaction which lead to the formation of CO_2 is favoured at those temperatures.

The amount of C and H_2O at equilibrium were found to decrease with increasing temperature. This was because the reactions leading to their formation such as the RWGS, CO hydrogenation and the Boudouard reactions had less influence on the systems with increasing temperature. This is because the K_a values for these reactions become significantly smaller in comparison to those of the methane cracking and DRM reactions. Considering that the goal of DRM is to maximise the production of synthesis gas whilst limiting the formation of carbon, it was concluded that higher temperatures would are most ideal for the dry reforming of methane. This conclusion is in line with those reached in the literature reviewed.

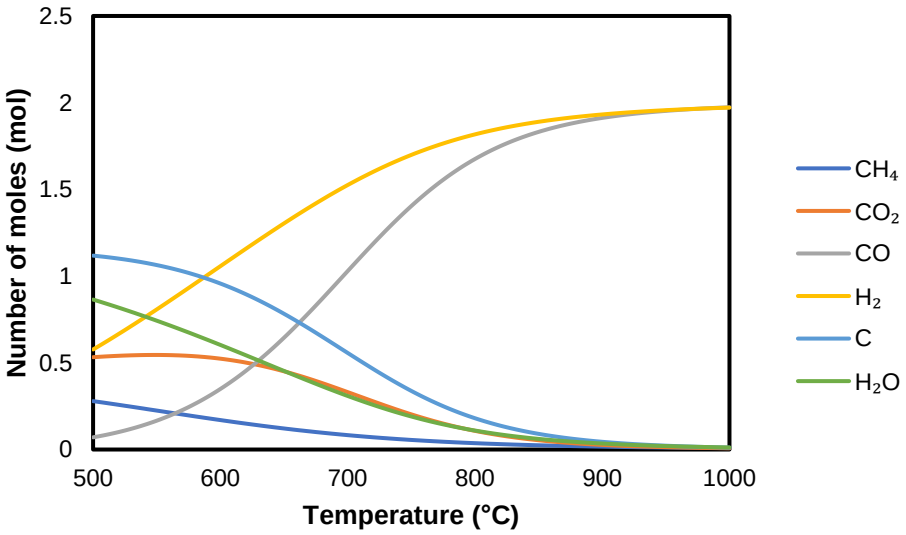

Figure 6.3: The variation of the number of moles at equilibrium for the system considering the DRM, methane cracking, RWGS, Boudouard and CO hydrogenation reactions as a function of temperature at 1.01325 bar. A CH_4:CO_2 molar ratio of 1:1 was used in the study (system without dilution).

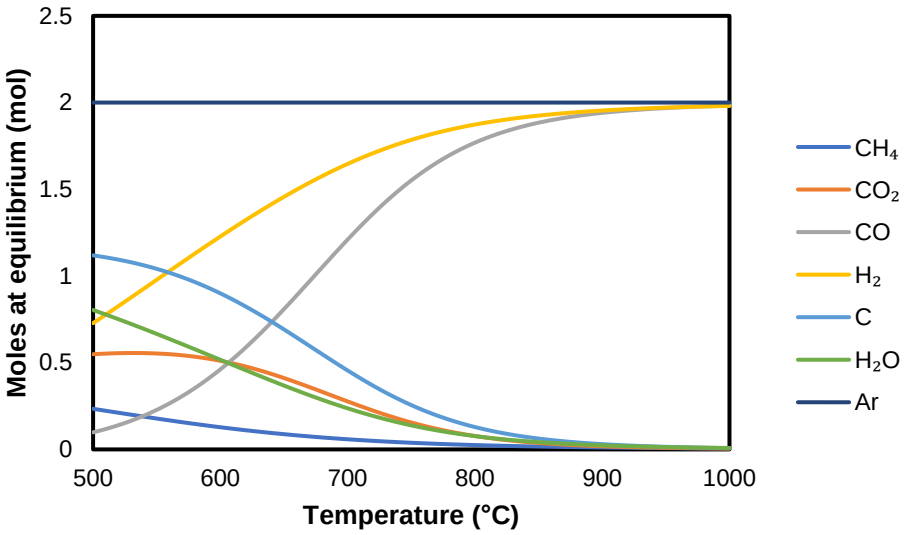

Figure 6.4: The variation of the number of moles at equilibrium for the system considering the DRM, methane cracking, RWGS, Boudouard and CO hydrogenation reactions as a function of temperature at 1.01325 bar. A CH_4:CO_2:Ar molar feed ratio of 1:1:2 was used (system with 50% Ar dilution).

The variation of X_{eq} CO_2 with temperature was calculated using the results obtained from the determination of the moles at equilibrium in the two systems studied. The results of the calculations are given in Figure 6.5. From Figure 6.5, X_{eq} CO_2 was found to decrease between 500 – 600 °C before subsequently increasing. The initial drop in X_{eq} CO_2 provided evidence that the Boudouard reaction which is exothermic competes with the RWGS and DRM reactions which are endothermic in this temperature range. Initially, the systems would favour having more CO_2 at equilibrium because of the Boudouard reaction which led to X_{eq} CO_2 decreasing. However, as the was temperature increased (above 600 °C) the DRM and RWGS reactions became more favourable resulting in X_{eq} CO_2 increasing after the initial drop.

Diluting the feed was found to decrease X_{eq} CO_2 for temperatures below 600 °C and to increase it for temperatures above 600 °C. This observation was assumed to be linked to the competition between the Boudouard, RWGS and DRM reactions at temperatures below 600 °C. Lastly, it was also noted that the initial values of X_{eq} CO_2 at 500 °C were both higher than the baseline values for X_{eq} CO_2 DRM reaction. The baseline X_{eq} CO_2 values for the DRM reaction were 15% and 20% for the systems without and with 50% Ar dilution, respectively. On the other hand, the initial X_{eq} CO_2

for the systems without and with 50% Ar dilution were 47% and 45% respectively. The significant difference in these values provided evidence for impact of side reactions in the systems studied.

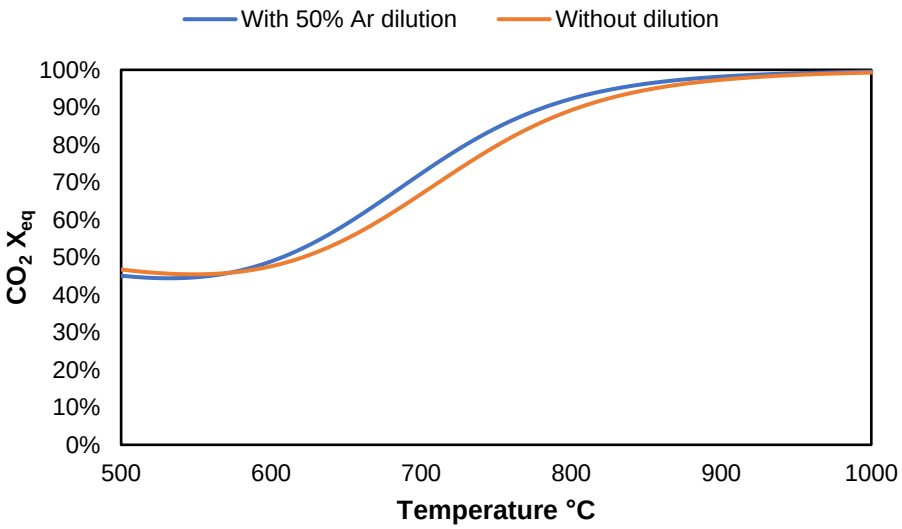

Figure 6.5: CO_2 equilibrium conversion as a function of temperature at 1.01325 bar for a system considering the DRM, methane cracking, RWGS, Boudouard and CO hydrogenation reactions. The system without dilution has a CH_4:CO_2 molar feed ratio of 1:1 whilst the system with 50% Ar dilution has a molar feed ratio of CH_4:CO_2:Ar of 1:1:2.

The variation of X_{eq} CH_4 with temperature was also calculated using the results obtained from the determination of the moles at equilibrium in the two systems studied. The results of the calculations are given in Figure 6.6. From the results, it was determined X_{eq} CH_4 that increased with increasing temperature. In addition, dilution was also found to increase X_{eq} CH_4. These findings followed similar trends to those obtained for the baseline values of X_{eq} CH_4 for the DRM reaction. However, the X_{eq} CH_4 values obtained for both systems studied were significantly higher at 500 °C. At 500 °C, the baseline X_{eq} CH_4 values for the DRM reaction were 15% and 20% for the systems without and with 50% Ar dilution, respectively. On the other hand, the X_{eq} CH_4 values for the systems with 50% Ar dilution and without it were 77% and 72% respectively at the same temperature. The methane cracking reaction which is favoured over the DRM reaction below 700 °C is the most likely reason why there is a large difference between the X_{eq} CH_4 values at lower temperatures.

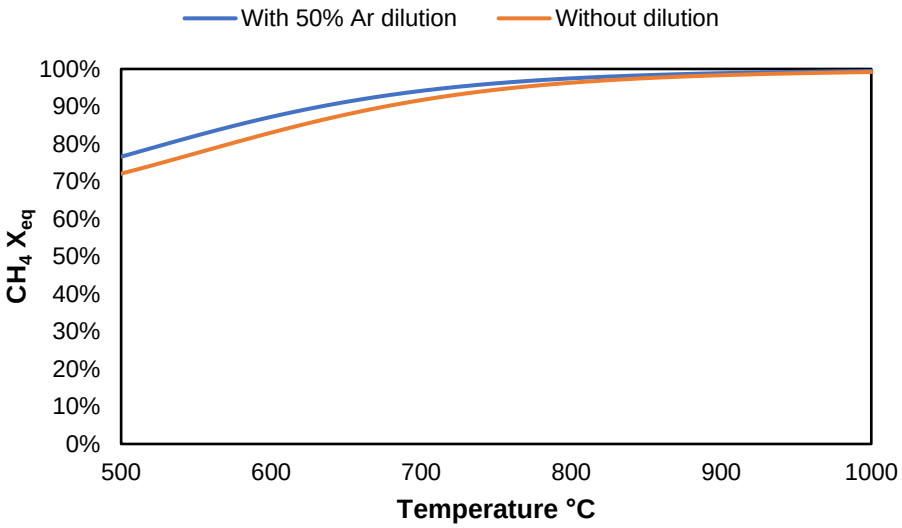

Figure 6.6: CH_4 equilibrium conversion as a function of temperature at 1.01325 bar for a system considering the DRM, methane cracking, RWGS, Boudouard and CO hydrogenation reactions. The case without dilution has a CH_4:CO_2 molar feed ratio of 1:1 whilst the case with 50% dilution has a molar feed ratio of CH_4:CO_2:Ar of 1:1:2.

6.1.2 Direct minimisation of Gibbs free energy approach

The first step in determining chemical equilibrium using the direct minimisation of Gibbs free energy approach was choosing the compounds that would make up the systems to studied. The first system studied was comprised of CH_4, H_2O, CO, CO_2, H_2 and C. For this system, a CH_4:CO_2 molar feed ratio of 1:1 was used. The second system was different from the first in that Ar was added as an additional compound to the system to study the effects of dilution. In the second system a CH_4:CO_2:Ar molar feed ratio of 1:1:2 was used to mimic the dilution that was used during catalyst testing. For both systems, the calculations were carried out a system pressure of 1.01325 bar. The calculations were carried out using the methodology outlined in Section 4.5.2.

The results of the calculation for the systems without dilution as well as with a 50% Ar feed dilution are provided in Figure 6.7 and Figure 6.8 respectively. From the results it was determined that higher temperatures would be most favourable for the DRM reaction. This is because the production of synthesis gas would be maximised as shown by the moles of H_2 and CO at equilibrium both approaching 2 moles at higher temperatures (which was the highest possible value they could reach based on the feed). The amount of C and H_2O at equilibrium also approached zero at higher temperatures which showed that formation of unwanted products was limited by increasing temperature. These results support conclusion reached when the same studies were carried out using the K_a approach which found that the DRM reaction

became more thermodynamically favourable than the side reactions that occur alongside it when the temperature was increased. In addition, the findings from the direct minimisation of Gibbs free energy were also in agreement with those obtained from the K_a approach in that there is more CO_2 and H_2 at equilibrium at lower temperatures than CO and CH_4. This also provided further evidence to the conclusion reached using the K_a approach which determined that the methane cracking reaction was initially more thermodynamically favourable than the DRM reaction.

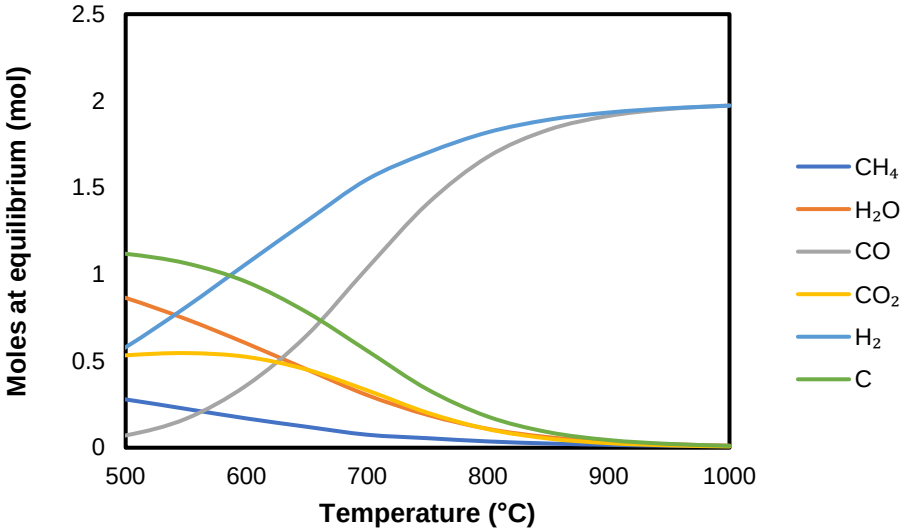

Figure 6.7: The variation of the number of moles at equilibrium as a function of temperature at 1.01325 bar for a system comprised of CH_4, H_2O, CO, CO_2, H_2 and C. The calculations were carried out using the direct minimisation of Gibbs free energy approach and a CH_4:CO_2 molar feed ratio of 1:1 was used

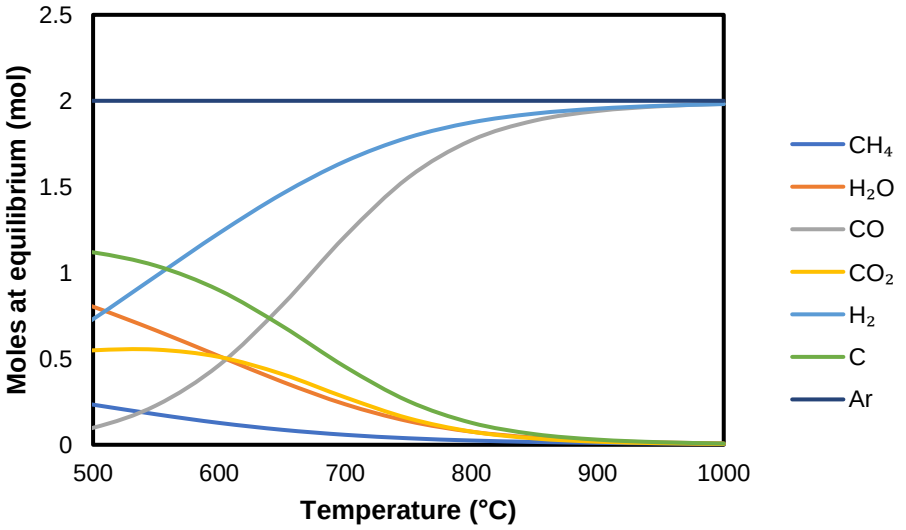

Figure 6.8: The variation of the number of moles at equilibrium as a function of temperature at 1.01325 bar for a system comprised of CH_4, H_2O, CO, CO_2, H_2, C and Ar. The calculations were carried out using the direct minimisation of Gibbs free energy approach and a CH_4:CO_2:Ar molar feed ratio of 1:1:2 was used

The variation of X_{eq} CO_2 and X_{eq} CH_4 with temperature was also determined using results for the moles at equilibrium obtained using the direct minimisation of Gibbs free energy approach for. This was done for the systems with and without 50% Ar dilution. The results for the variation of X_{eq} CO_2 and X_{eq} CH_4 with temperature are provided in Figure 6.9 and Figure 6.10 respectively. The results X_{eq} CO_2 presented in Figure 6.9 obtained from the direct minimisation of Gibbs free energy were similar to those obtained using the K_a approach which are given in Figure 6.5. This is because between 500 °C to 600 °C there is an initial drop X_{eq} CO_2 which is then followed by an increase. In addition, dilution was found to decrease X_{eq} CO_2 below 600 °C whilst increasing it above 600 °C. These observations are a result of the competition that occurs between the Boudouard, RWGS and DRM reactions in the temperature range studied. This was discussed in detail for the K_a approach.

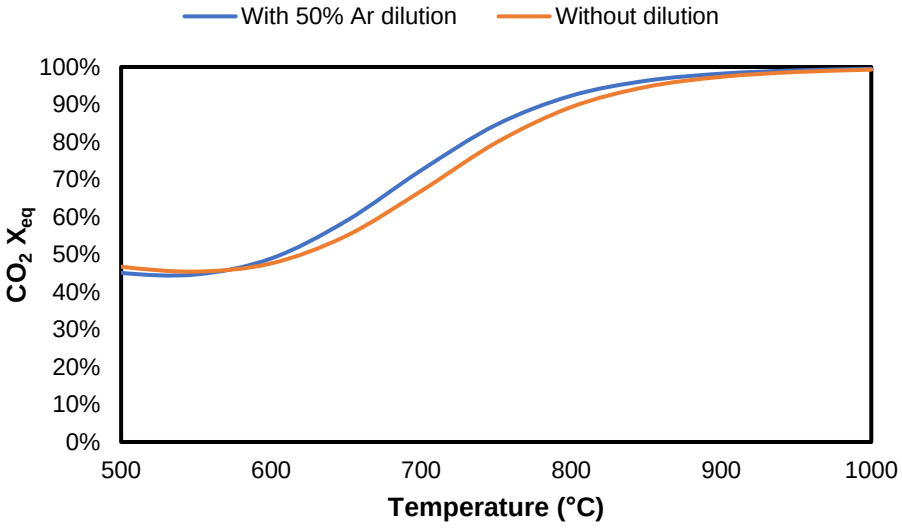

Figure 6.9: CO_2 equilibrium conversion as a function of temperature at 1.01325 bar. The calculations were carried out using the direct minimisation of Gibbs free energy approach. A CH_4:CO_2:Ar molar feed ratio of 1:1:2 was used for the system with 50% Ar dilution whilst a CH_4:CO_2 molar feed ratio of 1:1 was used for the system without dilution.

The results for the variation of X_{eq} CH_4 with temperature are provided in Figure 6.10. From these values it was determined that the values of X_{eq} CH_4 at lower temperatures are significantly higher the corresponding X_{eq} CO_2 values. The reason behind this was that the methane cracking reaction was more thermodynamically favourable over the DRM reaction below 700 °C. In addition, diluting the system with Ar was found to increase X_{eq} CH_4. These findings agreed with those obtained from the calculations carried out using the K_a approach.

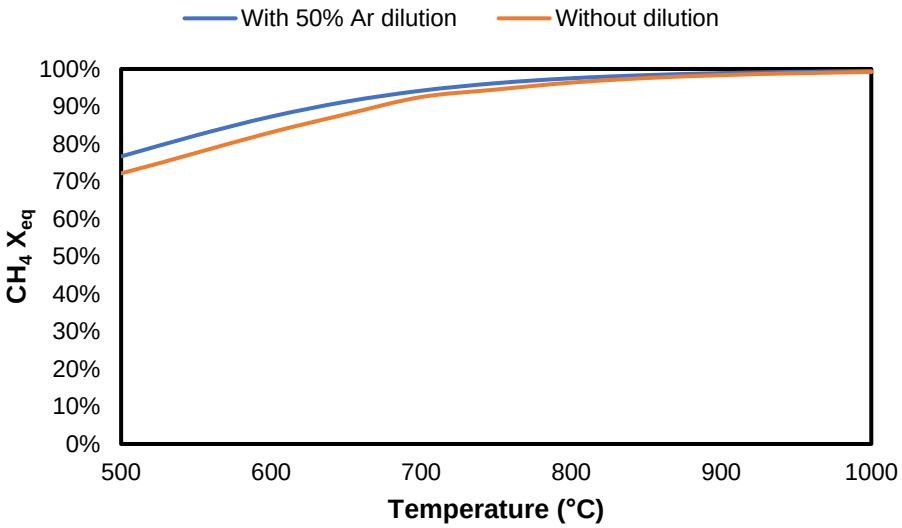

Figure 6.10: CH_4 equilibrium conversion as a function of temperature at 1.01325 bar. The calculations were carried out using the direct minimisation of Gibbs free energy approach. A CH4:CO2:Ar molar feed ratio of 1:1:2 was used for the system with 50% Ar dilution whilst a CH_4:CO_2 molar feed ratio of 1:1 was used for the system without dilution.

6.1.3 Summary

From the thermodynamic analyses carried out using the K_a approach as well as the direct minimisation of Gibbs free energy, it was concluded higher temperatures are more favourable for the DRM reaction. This was because the side reactions that compete with it such as the methane cracking and the RWGS reaction had a less pronounced impact on the thermodynamic behaviour at higher temperatures. In addition, it was also concluded that the DRM, methane cracking, Boudouard, CO hydrogenation and the RWGS reactions could sufficiently describe what happens thermodynamically during the dry reforming of methane in the temperature range studied. This was because the results obtained using the K_a approach using these reactions as a basis agreed with results from the direct minimisation of the Gibbs free energy which were calculated based on a system of compounds rather than specific reactions.

Carrying out the thermodynamic equilibrium analyses using two approaches was found to be useful in gaining a deeper understanding of the dry reforming of methane from a thermodynamic standpoint. The calculations carried out using the K_a approach were helpful in that they provided an opportunity to match the thermodynamic behaviour to specific reactions. This process would have been more difficult if only the direct minimisation of Gibbs free energy approach had been employed because it was

not directly dependent on specific reactions. However, the direct minimisation of Gibbs free energy was helpful in that it provided a way to determine whether the reactions chosen for the K_a approach were adequately represented the chemical equilibrium of the system. This was because its results would remain constant for a specific set of compounds. It must be noted that though thermodynamic calculations were a good starting point in understanding the dry reforming of methane, ultimately the catalyst would determine what was observed during catalyst testing. This is because catalysts can influence which reactions occur by kinetically suppressing some reactions over others.

Based on the findings of the thermodynamic analysis, it was decided to carry out the first stage of catalyst testing at temperatures between 600 – 750 °C. This temperature range was chosen with the goal of understanding how the catalysts chosen for the study would perform at in favouring the DRM reaction over the that compete with it such as the Boudouard, RWGS and methane cracking reactions.

6.2 Catalyst testing

Catalyst testing was carried out using two stages namely: preliminary catalyst testing and final catalyst testing. During preliminary catalyst testing (DRM runs 1.1 – 1.5), the focus was on analysing the performance of catalysts at different reaction temperatures between 600 – 750 °C as well as to study the long-term stability of catalysts in DRM. Due to the time constraints associated with carrying out long-term stability experiments, only the Ni-Co(90:10), Ni-Co(50:50) and Ni-Co(10:90) catalysts were used during preliminary catalyst testing.

The findings from preliminary catalyst testing were then used to choose a single set of conditions that would be ideal to test all the catalysts prepared in the study. The catalyst tests that were carried out at these conditions were called final catalyst testing (DRM runs 2.2 – 2.7). The results from the final catalyst testing experiments were then used to compare the performance of all the catalysts prepared in the study in methane dry reforming.

The experimental procedures that were followed during catalyst testing are described in Sections 4.3.2 and 4.3.3. The conditions for the catalyst tests carried out are also available in Table 4.2. The catalysts were reduced at 700 °C for 2 hours before all the catalyst testing experiments.

6.2.1 Preliminary catalyst testing

6.2.1.1 DRM run 1.1: Ni-Co(50:50) catalyst

The results for the variation of conversion with time on stream (TOS) for the Ni-Co(50:50) catalyst at 600 °C and 650 °C are given in Figure 6.11. For the catalyst testing carried out at 650 °C, only the results during the first 6 hours at the temperature were considered. This is because there was a disruption in the CO_2 gas flow that occurred after that point. From the results given in Figure 6.11, it was determined that the activity of the catalyst decreased with TOS at both temperatures tested. To illustrate this, at 600 °C, the CH_4 and CO_2 conversions decreased from 27% and 37% respectively after a TOS of 1 hour to 22% and 30% respectively after a TOS of 12 hours. On the other hand, increasing the temperature was found to lead to an increase in conversion as was shown by both the CH_4 and CO_2 conversions rising to 34% and 44% respectively during the first hour at 650 °C. The effect that increasing temperature had on the conversion was in line with the findings of the thermodynamic analysis that was carried out. However, the prediction from the thermodynamic analysis that the conversion of CH_4 would be higher than that of CO_2 did not hold based on the results obtained. A possible explanation for this would be that the catalyst suppressed the methane cracking reaction which usually is behind the CH_4 conversion being higher. Additionally, the RWGS reaction could have also caused the CO_2 conversion to be higher than the CH_4 conversion.

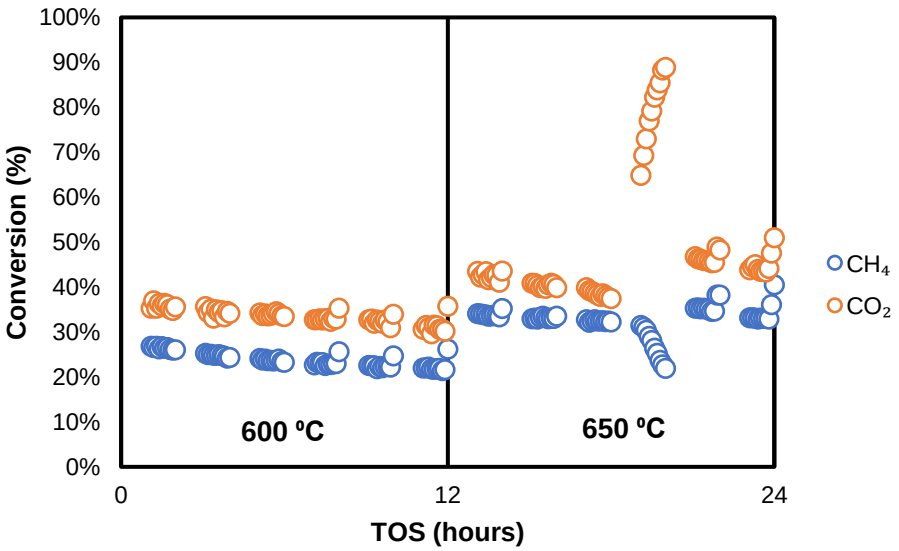

Figure 6.11: The variation of conversion with TOS for the Ni-Co(50:50) catalyst in DRM run 1.1. (Pressure: atmospheric, CH_4:CO_2:Ar feed ratio: 1:1:2, space velocity: 160000 mL/g_{cat}-h).

The results for the variation of the H_2/CO ratio with TOS for the Ni-Co(50:50) catalyst are presented in Figure 6.12. The H_2/CO ratio is often used as an indicator of selectivity in DRM. In a case where only the DRM reaction happens, an H_2/CO ratio of 1 is expected. According to Pakhare & Spivey (2014), having a H_2/CO ratio below 1 serves as an indicator for the RWGS reaction being the dominant side reaction whilst a H_2/CO ratio above 1 indicates that the methane cracking reaction is the dominant side reaction. Based on this, it was determined that at the temperatures at which the catalyst was tested, the RWGS reaction was the dominant side reaction as the H_2/CO ratios were below 1. The RWGS reaction being the dominant side reaction also provided support as to why the CO_2 conversion was higher than the CH_4 conversion. The outliers observed in Figure 6.12 after a TOS of 18 hours were a result of the disruption in the CO_2 gas flow that occurred during catalyst testing.

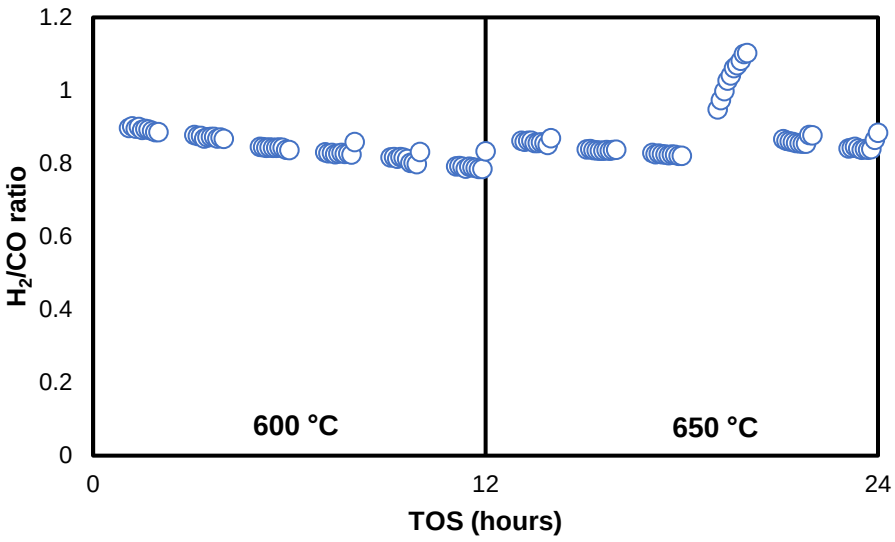

Figure 6.12: The variation of the H2/CO ratio with TOS for the Ni-Co(50:50) catalyst in DRM run 1.1. (Pressure: atmospheric, CH_4:CO_2:Ar feed ratio: 1:1:2, space velocity: 160000 mL/g_{cat}-h).

6.2.1.2 DRM run 1.2: Ni-Co(90:10) catalyst

The results for variation of conversion with TOS for the Ni-Co(90:10) catalyst at 600 °C and 650 °C are given in Figure 6.13. For the catalyst testing carried out at 650 °C, only the results for the first 6 hours at the temperature were considered. This is because there was a disruption in the CO_2 gas flow that occurred 18 hours into catalyst testing. From the results in Figure 6.13, it was determined that the activity of the catalyst decreased with TOS at both temperatures tested. To illustrate this, at 600 °C, the CH_4 and CO_2 conversions decreased from 31% and 39% respectively after a TOS of 3 hours to 25% and 34% respectively after a TOS of 11 hours. On the other hand, increasing the temperature was found to increase conversion as was shown by both the CH_4 and CO_2 conversions rising to 39% and 47% respectively when the temperature was increased to 650 °C after a TOS of 12 hours. This was expected due to the endothermic nature of the DRM reaction and the RWGS and methane cracking side reactions that compete with it. As was the case for the Ni-Co(50:50) catalyst, the CO_2 conversion was higher than the CH_4 conversion. This also led to the conclusion that the RWGS reaction was potentially the dominant side reaction during catalyst testing. The findings from the catalyst testing for the Ni-Co(90:10) catalyst were similar to those obtained for the Ni-Co(50:50). However, the main difference between the results was that the Ni-Co(90:10) catalyst was more active than the Ni-Co(50:50) catalyst as it had higher CO_2 and CH_4 conversions.

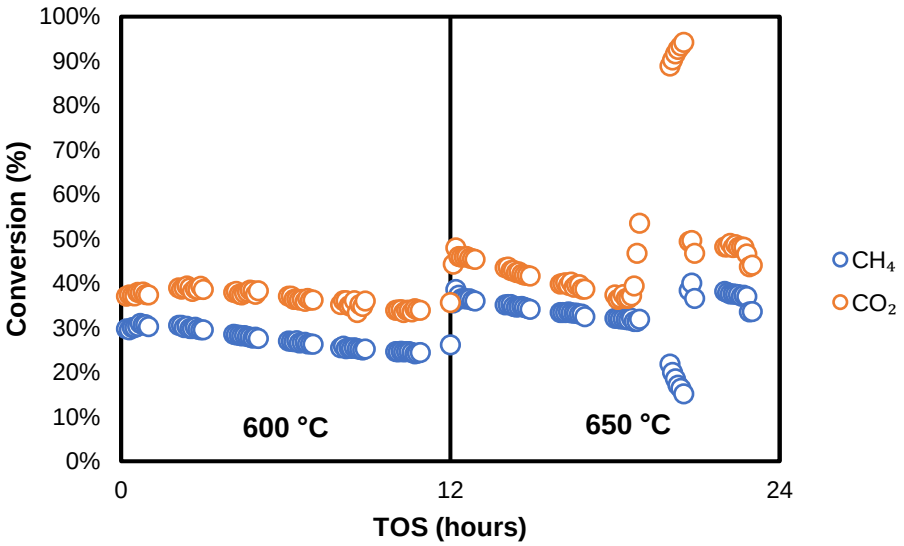

Figure 6.13: The variation of conversion with TOS for the Ni-Co(90:10) catalyst in DRM run 1.2. (Pressure: atmospheric, CH_4:CO_2:Ar feed ratio: 1:1:2, space velocity: 160000 mL/g_{cat}-h).

The results for the variation of the H_2/CO ratio with TOS for the Ni-Co(90:10) catalyst are presented in Figure 6.14. From Figure 6.14, the H_2/CO ratio remains below 1 during catalyst testing. Based on this it was concluded that the RWGS reaction was the dominant side reaction during catalyst testing. It should also be noted that increasing the temperature led to a slight increase in the H_2/CO ratio which could be an indication that the influence of the RWGS reaction at higher temperatures is less. The outliers observed in Figure 6.14 after a TOS of 18 hours were a result of the disruption in the CO_2 gas flow that occurred during catalyst testing.

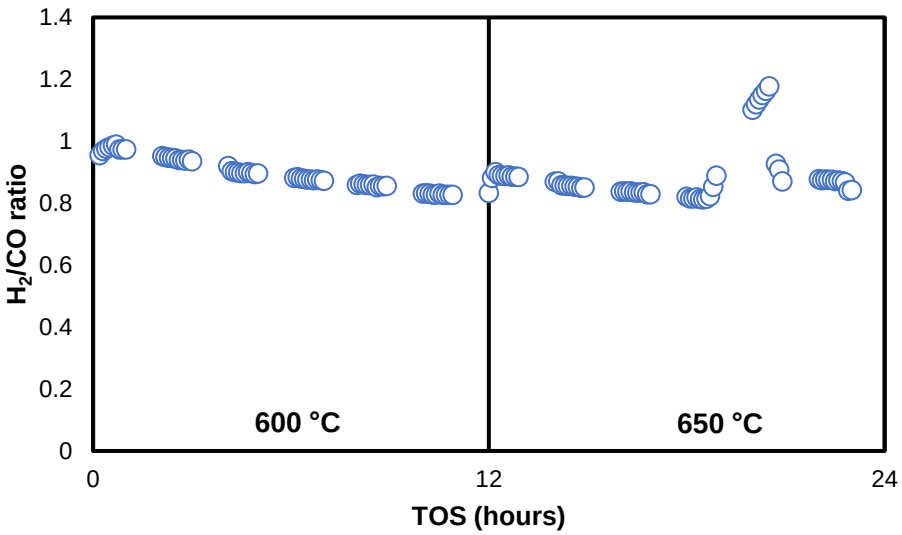

Figure 6.14: The variation of the H_2/CO ratio with TOS for the Ni-Co(90:10) catalyst in DRM run 1.2. (Pressure: atmospheric, CH_4:CO_2:Ar feed ratio: 1:1:2, space velocity: 160000 mL/g_{cat}-h).

6.2.1.3 DRM run 1.3: Ni-Co(50:50) catalyst

The results for variation of conversion with TOS for the Ni-Co(50:50) catalyst at 750 °C and 700 °C are given in Figure 6.15. From the results presented in Figure 6.15, it was determined that the catalyst was more stable at 750 °C and 700 °C than at 600 °C and 650 °C. This was because there were no significant losses in CO_2 and CH_4 conversion with increasing TOS as was the case at 600 °C and 650 °C. The CO_2 and CH_4 conversions remained stable at 68% and 59% at 750 °C. When the temperature was decreased to 700 °C, the CO_2 and CH_4 conversion dropped down to 56% and 45% respectively. The catalyst was able to maintain these conversions throughout the 12-hour testing period at the temperature. Lastly the catalyst was also found to be able to recover to its initial activity when the temperature was increased back to 750 °C. As was the case when catalyst testing was carried out at 600 °C and 650 °C, the CO_2 conversion was higher than the CH_4 conversion.

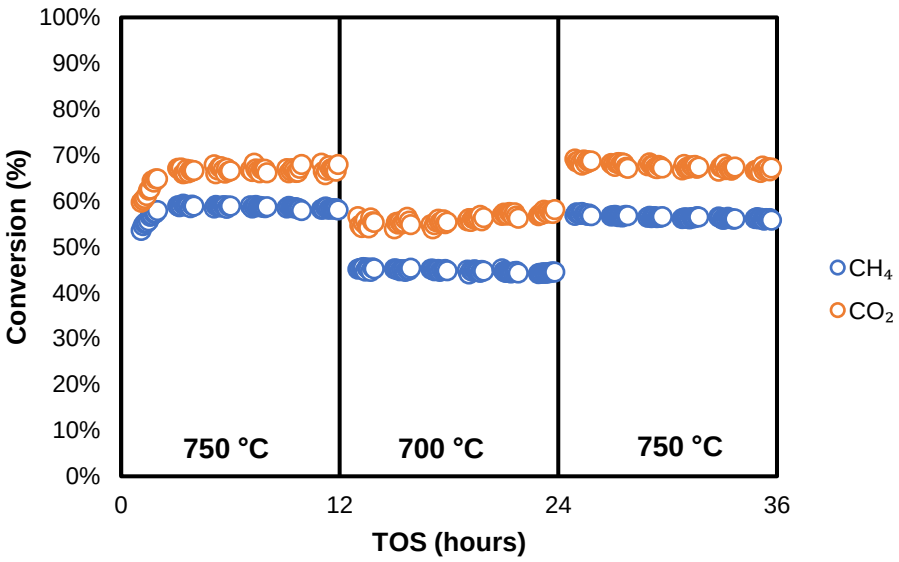

Figure 6.15: The variation of conversion with TOS for the Ni-Co(50:50) catalyst in DRM run 1.3. (Pressure: atmospheric, CH_4:CO_2:Ar feed ratio: 1:1:2, space velocity: 160000 mL/g_{cat}-h).

The results of how the H_2/CO ratio varied with TOS are given in Figure 6.16. The H_2/CO ratio at 750 °C started off at 1.05 at a TOS of 1 hour and gradually dropped to 0.96 after a TOS of 12 hours. During catalyst testing at 700 °C, the H_2/CO ratio reached a minimum of 0.9. Since the H_2/CO was close to 1 at both temperatures tested it was difficult to make a call as to whether the methane cracking reaction was more dominant than the RWGS reaction during catalyst testing.

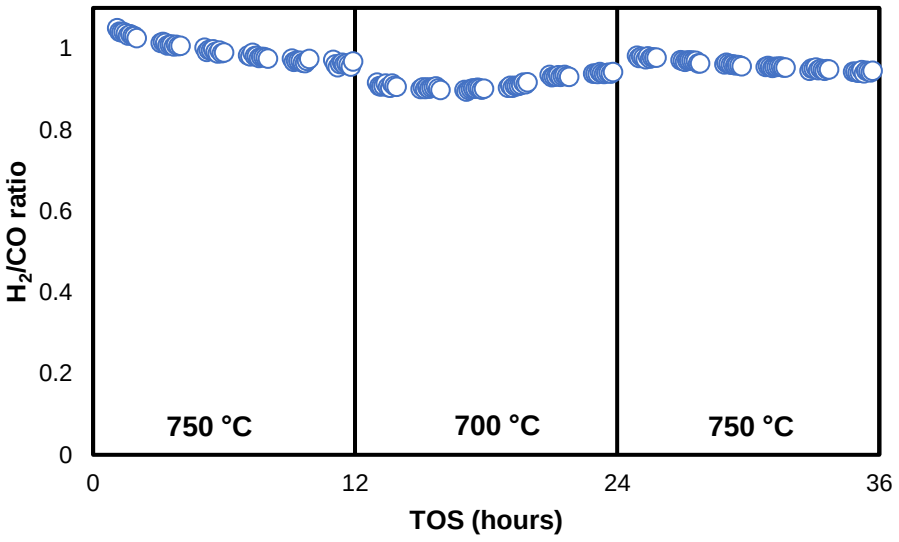

Figure 6.16: The variation of the H_2/CO ratio with TOS for the Ni-Co(50:50) catalyst in DRM run 1.3. (Pressure: atmospheric, CH_4:CO_2:Ar feed ratio: 1:1:2, space velocity: 160000 mL/g_{cat}-h).

6.2.1.4 DRM run 1.4: Ni-Co(90:10) catalyst

The results for the variation of conversion with TOS for the Ni-Co(90:10) catalyst at 750 °C and 700 °C are given in Figure 6.17. From the results presented in Figure 6.17, it was determined that the catalyst was more stable at 750 °C and 700 °C than it was at 600 °C and 650 °C. This was because there were no significant changes decreases in CO_2 and CH_4 conversion with increasing TOS as was the case at 600 °C and 650 °C. The CO_2 and CH_4 conversions remained stable at 80% and 78% at 750 °C. When the temperature was decreased to 700 °C, the CO_2 and CH_4 conversion dropped down to 67% and 60% respectively. Lastly the catalyst was also found to be able to recover to its initial activity when the temperature was increased back to 750 °C. As was the case when catalyst testing was carried out at 600 °C and 650 °C, the CO_2 conversion was higher than the CH_4 conversion. However, the difference between the two conversions during the first 12 hours was not miniscule as it remained around 2%. However, the difference between the CO_2 and CH_4 conversions increased with TOS.

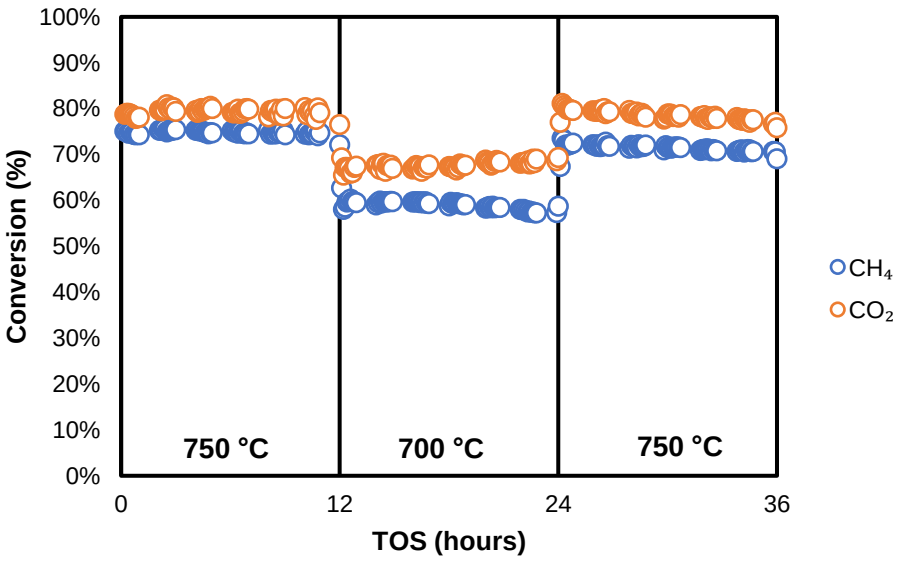

Figure 6.17: The variation of conversion with TOS for the Ni-Co(90:10) catalyst in DRM run 1.4. (Pressure: atmospheric, CH_4:CO_2:Ar feed ratio: 1:1:2, space velocity: 160000 mL/g_{cat}-h).

The results of how the H_2/CO ratio varied with TOS are given in Figure 6.18. The H_2/CO ratio was consistently above 1 for both periods when catalyst testing was carried at 750 °C reaching a maximum of 1.06 during the first 12 hours of catalyst testing. At 700 °C, the H_2/CO ratio was slightly below 1 reaching a minimum of 0.96. Considering how close the H_2/CO ratio was to 1, it was difficult to make a call on which

side reaction was dominant during catalyst testing at 750 °C and 700 °C. Though an argument can be made that methane cracking was dominant at the start of the reaction when the H_2/CO ratio was above 1.

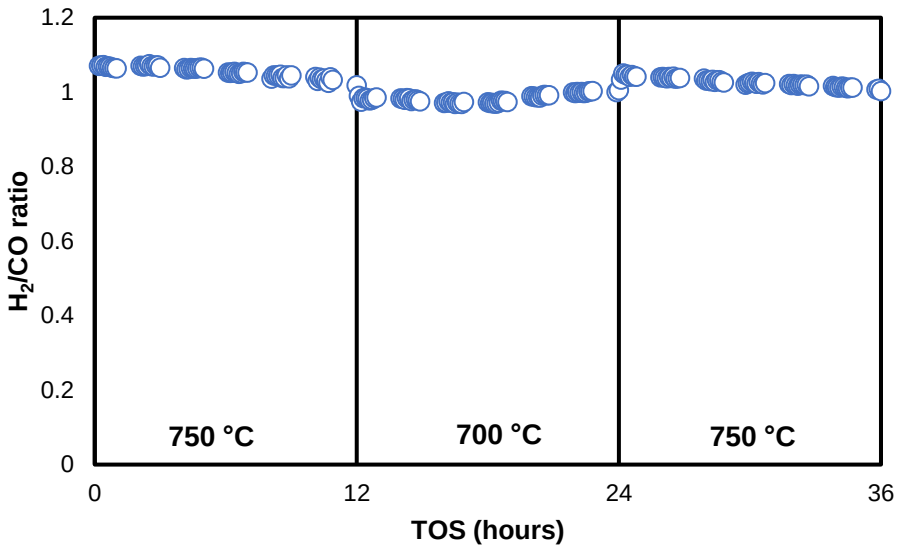

Figure 6.18: The variation of the H_2/CO with TOS for the Ni-Co(90:10) catalyst in DRM run 1.4. (Pressure: atmospheric, CH_4:CO_2:Ar feed ratio: 1:1:2, space velocity: 160000 mL/g_{cat}-h).

6.2.1.5 DRM run 1.5: Ni-Co(10:90) catalyst

The results for variation of conversion with TOS for the Ni-Co(10:90) catalyst at 750 °C, 700 °C, 650 °C and 600 °C are given in Figure 6.19. From Figure 6.19, it was determined that the catalyst was most active at the start of the reaction, but its activity decreased with increasing TOS. During the first 12 hours of catalyst testing at 750 °C, the CO_2 and CH_4 conversions dropped from 79% and 70% to 70% and 59% respectively. This trend was also replicated at 700 °C, 650 °C and 600 °C as the activity continued to decrease with increasing TOS at each of those temperatures. The catalyst reached its lowest level of activity after a TOS of 48 hours at 600 °C where the CO_2 and CH_4 conversions were 17% and 12% respectively. Unlike the Ni-Co(50:50) and Ni-Co(90:10) catalysts in DRM runs 1.3 and 1.4, the Ni-Co(10:90) catalyst was unable to recover to its initial activity when the temperature was raised back to 750 °C for the final 12 hours of catalyst testing. This was understandable because of how conversion was found to decrease with TOS at all the temperatures that the catalyst was tested at. During the final 12 hours of catalyst testing the CO_2 and CH_4 conversions dropped from 60% and 52% to 56% and 47% respectively. The

CO_2 conversion also remained higher than the CH_4 conversion throughout the 60-hour catalyst testing period.

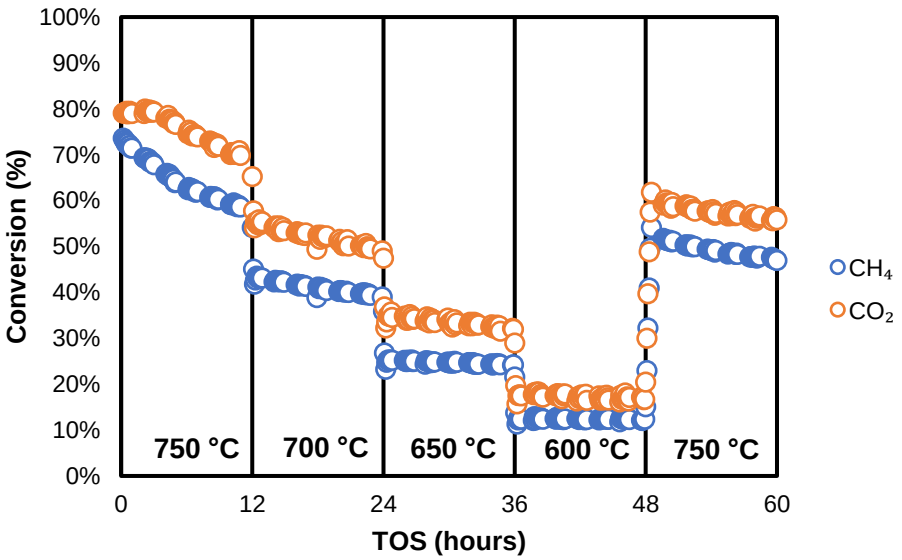

Figure 6.19: The variation of conversion with TOS for the Ni-Co(10:90) catalyst in DRM run 1.5. (Pressure: atmospheric, CH_4:CO_2:Ar feed ratio: 1:1:2, space velocity: 160000 mL/g_{cat}-h).

The results of the variation of the H_2/CO ratio with TOS are given in Figure 6.20. From the results, the H_2/CO ratio started of above 1 reaching a maximum around 1.08 at a TOS of 3 hours. After that maximum point, the H_2/CO ratio proceeded to drop below 1 for the remainder of catalyst testing. Decreasing the temperature was found to decrease the H_2/CO ratio. A minimum H_2/CO ratio of 0.63 reached during catalyst testing at 600 °C. Based on the results it was concluded that the RWGS reaction was the dominant side reaction during catalyst testing as the H_2/CO ratio was consistently below 1. Additionally, its impact was found to be more significant at lower temperatures.

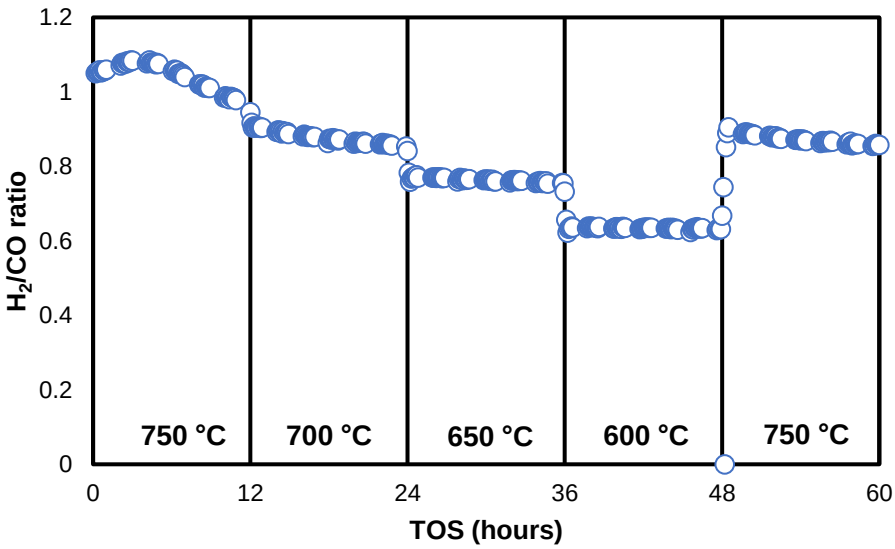

Figure 6.20: The variation of the H_2/CO ratio with TOS for the Ni-Co(10:90) catalyst in DRM run 1.5. (Pressure: atmospheric, CH_4:CO_2:Ar feed ratio: 1:1:2, space velocity: 160000 mL/g_{cat}-h).

6.2.1.6 Summary

From preliminary catalyst testing it was concluded that the catalysts had higher conversion at higher temperatures. This was expected because of the endothermic nature of the dry reforming of methane as well as the findings from the thermodynamic analysis that was carried out. In terms of activity, the Ni-Co(90:10) catalyst was the most active amongst the catalysts tested, followed by the Ni-Co(10:90) catalyst with the Ni-Co(50:50) catalyst being least active. This conclusion was reached based on the activity results from the first 12 hours of catalyst testing in DRM runs 1.3 – 1.5. The comparison could be made as catalysts were tested at the same temperature (750 °C) during that time. It must be noted that though the Ni-Co(10:90) catalyst was initially more active than the Ni-Co(50:50) catalyst, its activity was not stable as the CO_2 and CH_4 conversions were found to decrease with TOS. The Ni-Co(90:10) and Ni-Co(50:50) catalysts were found to be able to maintain a constant level of activity at 750 °C and 700 °C. This stability made them intriguing catalysts especially for long term use.

The CO_2 conversion was found to be higher than the CH_4 conversion during catalyst testing for all the catalysts that were studied. This result was likely caused by RWGS side reaction. The results of the H_2/CO ratio during catalyst testing provided some additional evidence for the likely occurrence of the RWGS reaction especially at 600

°C and 650 °C because it was below 1. However, at 750 °C and 700 °C the H_2/CO ratios were much closer to 1 and sometimes above 1. This showed the influence of the RWGS likely decreased with increasing temperate with the methane cracking reaction being more significant at higher temperatures.

Based on the first set of catalyst testing experiments, it was decided that final catalyst testing would be carried out at 700 °C for a TOS of 12 hours. These conditions were chosen because the catalysts studied during the preliminary testing showed good activity at the temperature. In addition, a TOS of 12 hours was deemed to be sufficient to compare the performance of the catalyst at a temperature because it was shown that losses in activity could be adequately determined over a 12-hour time-period.

6.2.2 Final catalyst testing

During final catalyst testing, all the catalyst were tested at 700 °C for a period of 12 hours. The results obtained were then used to determine whether there was a relationship between the Ni-Co composition of the catalysts and their performance in the dry reforming of methane. The CH_4 and CO_2 conversions after a TOS of 1 hour and 10 hours were used as the basis of comparison between the catalysts. It must be noted that there was no conversion data for the Ni-Co(10:90) catalyst at a TOS of 10 hours because the reactor was blocked due to carbon formation during catalyst testing. The results for the variation of CH_4 and CO_2 conversions with TOS for all the catalysts during final catalyst testing are provided in Figure 6.21 and Figure 6.22, respectively. From Figure 6.21 and Figure 6.22, it is evident that all the catalysts tested except for the Ni(100) catalyst were relatively stable during catalyst testing. In addition, the CO_2 conversions were higher than the CH_4 conversions for all the catalysts tested which agreed with the results from preliminary catalyst testing.

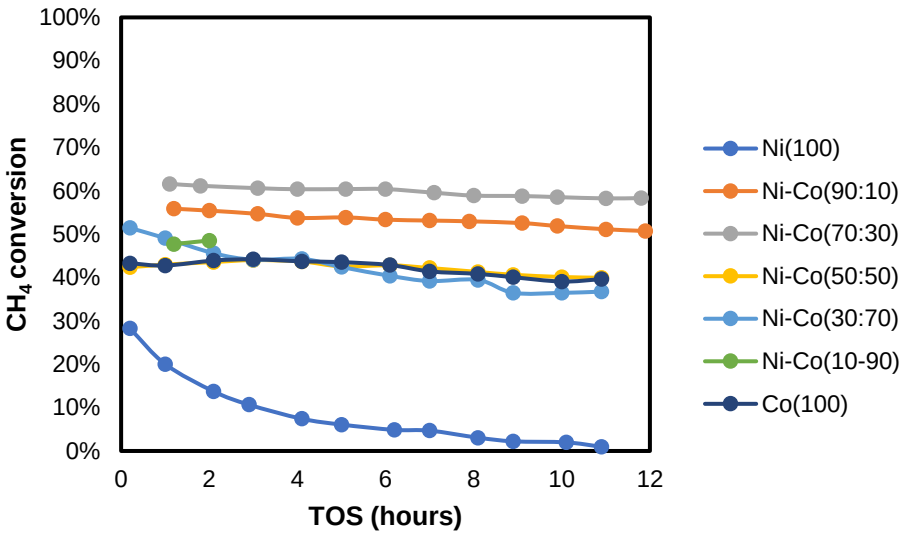

Figure 6.21: The variation of CH_4 conversion with TOS for the all the catalysts tested in DRM runs 2.1 – 2.7. (Pressure: atmospheric, CH_4:CO_2:Ar feed ratio: 1:1:2, space velocity: 160000 mL/g_{cat}-h).

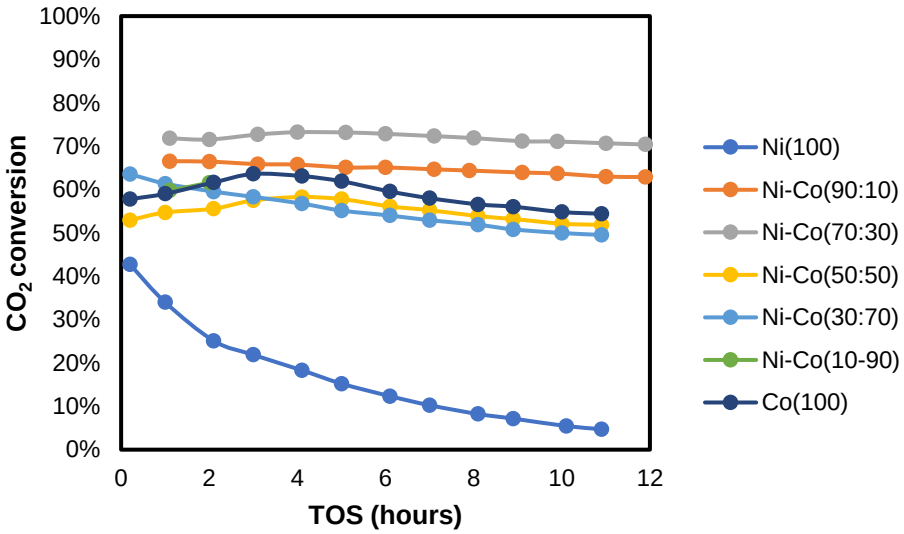

Figure 6.22: The variation of CH_4 conversion with TOS for the all the catalysts tested in DRM runs 2.1 – 2.7. (Pressure: atmospheric, CH_4:CO_2:Ar feed ratio: 1:1:2, space velocity: 160000 mL/g_{cat}-h).

The relationship between the CH_4 and CO_2 conversions and the Ni-Co composition of the catalysts are given in Figure 6.23 and Figure 6.24 respectively. From the results in Figure 6.23 and Figure 6.24, it was determined that the nickel rich bimetallic Ni-Co catalysts were the most active catalysts. The reasoning behind this was that the Ni-Co(70:30) catalyst had the highest CH_4 and CO_2 conversions followed by the Ni-Co(90:10) catalyst. The cobalt rich Ni-Co catalysts and the monometallic cobalt catalyst were found to be less active than the nickel rich Ni-Co catalysts as their CH_4

and CO_2 conversions were lower. However, the activity of the cobalt rich Ni-Co catalysts and the monometallic cobalt catalysts was similar. The most surprising finding from final catalyst testing was that the monometallic nickel catalyst was the least active catalyst because it had the lowest initial CH_4 and CO_2 conversions at a TOS of 1 hour. Additionally, the Ni(100) catalyst was the least stable because it had it experienced the largest losses in activity of all the catalysts tested. This was illustrated by the catalyst experiencing relative losses in CH_4 and CO_2 conversion of 90% and 85% respectively over a 9-hour time period as shown in Table 6.1. The relatively losses in conversion experienced by the rest of the catalysts are also provided in Table 6.1. Data for the Ni-Co(10:90) catalyst was unavailable due to the reactor blockage that occurred during the testing of that catalyst.

Table 6.1: Summary of the relative loss in CH_4 and CO_2 conversion between TOS: 1 hour and TOS: 10 hours during DRM runs 2.1 - 2.7

Catalyst	Relative loss in CH_4 conversion	Relative loss in CO_2 conversion
Ni(100)	90%	85%
Ni-Co(90:10)	5%	4%
Ni-Co(70:30)	5%	1%
Ni-Co(50:50)	7%	5%
Ni-Co(30:70)	14%	18%
Ni-Co(10:90)		
Co(100)	9%	7%

From the results, it was concluded that bimetallic Ni-Co catalyst can be more active than monometallic cobalt and nickel catalysts. This was especially true for the nickel rich Ni-Co catalysts that were studied. These conclusions were in line with those reached by Luisetto *et al.* (2012), Gao *et al.* (2017) and Horlyck *et al.* (2018). The low of activity of the monometallic nickel catalyst was also surprising because Takanabe *et al.* (2005) and Ay & Üner (2015) who studied the activity of bimetallic Ni-Co catalysts in the dry reforming of methane found monometallic catalyst to be more active than bimetallic Ni-Co catalysts. The lack of stability of the monometallic nickel catalyst was also surprising as Guo *et al.* (2004) found nickel catalysts supported on $MgAl_2O_4$ to have good stability during dry reforming.

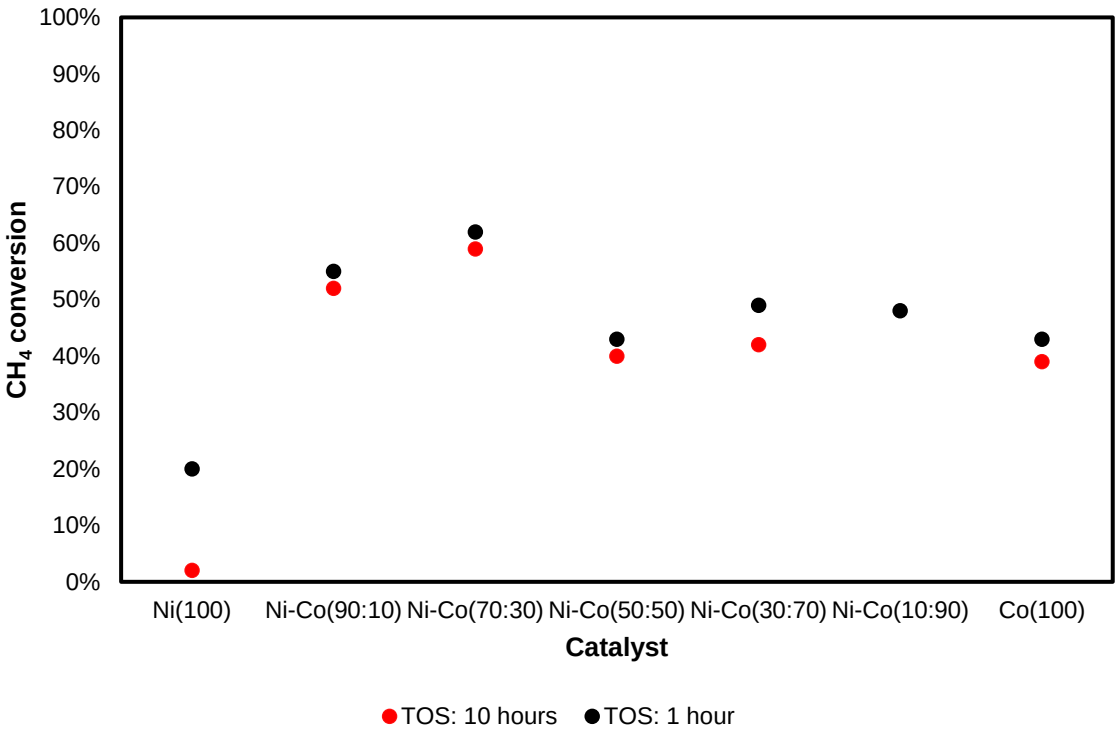

Figure 6.23: The relationship between the CH_4 conversion at 700 °C and the Ni-Co composition for DRM runs 2.1 – 2.7. (Pressure: atmospheric, CH_4:CO_2:Ar feed ratio: 1:1:2, space velocity: 160000 mL/g_{cat}-h).

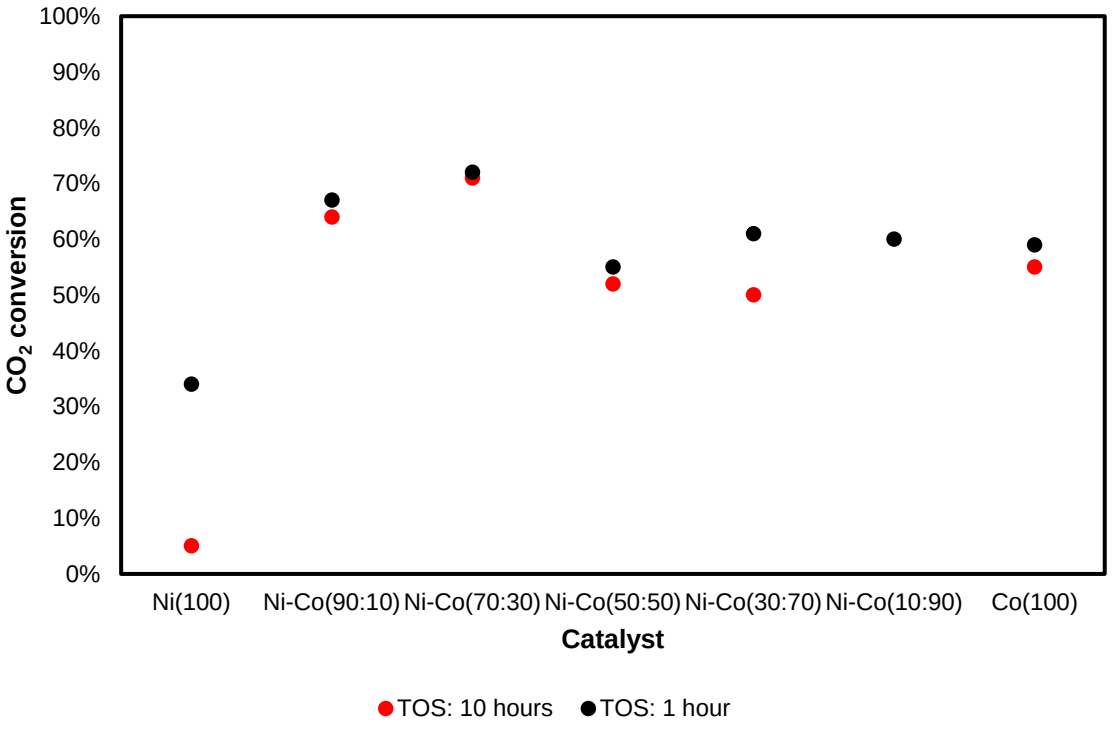

Figure 6.24: The relationship between the CO_2 conversion at 700 °C and the Ni-Co composition for DRM runs 2.1 – 2.7. (Pressure: atmospheric, CH_4:CO_2:Ar feed ratio: 1:1:2, space velocity: 160000 mL/gcat-h).

7 Post-run catalyst characterization results

7.1 Powder X-ray Diffraction (PXRD)

After catalyst testing, the catalysts were recovered and characterised by PXRD. The PXRD patterns obtained during the first stage of catalyst testing (DRM runs 1.1-1.5) are provided in Figure 7.1. However, no PXRD pattern is provided for DRM run 1.1 because of difficulties incurred when recovering the catalyst for that run. When comparing the PXRD patterns provided in Figure 7.1 to those of the fresh catalyst that were presented in Figure 5.3, the main difference is the presence of a graphite peak (C) at a 2θ value of 30 °. This result provides evidence for the fact that carbon deposition occurred on the catalysts during this set of catalyst tests. Additionally, the catalysts recovered from DRM run 1.2 – 1.4 have peaks at a 2θ value of 60°, which matches with the CoNi reference. This peak also provides evidence regarding the presence of the CoNi alloy in the catalysts during catalyst testing. A possible explanation for the absence of this peak in the pattern for DRM run 1.5 could be that the catalyst oxidised before PXRD analysis was carried out.

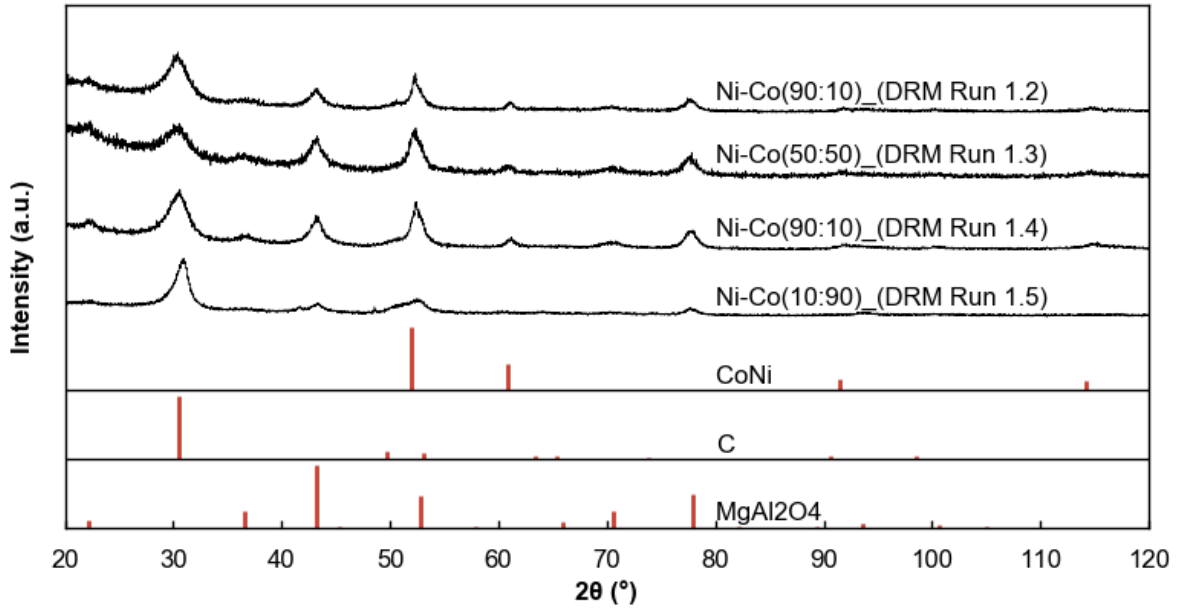

Figure 7.1: PXRD patterns obtained after the catalyst testing for DRM runs 1.2 – 1.5. Reference patterns for CoNi, C and $MgAl_2O_4$ are also provided in red.

PXRD was also used to characterise the catalysts recovered from the second set of catalyst tests (DRM runs 2.1 – 2.7). The PXRD patterns obtained for these catalysts are provided in Figure 7.2. From Figure 7.2, it is evident that there was carbon

deposition on all catalysts during catalyst testing except for the Ni(100) catalyst from DRM run 2.1. The peak in the PXRD patterns at a 2θ value of 30°, which matches to the C reference, provided evidence for the carbon deposition that occurred. Additionally, some of the tested catalysts have a peak at a 2θ value of 60°, which matches with the CoNi reference. This peak provides evidence regarding the presence of the CoNi alloy in the catalysts where it is found. Catalyst oxidation is a possible explanation for the absence of this peak in the rest of the catalysts where it was not found in the PXRD patterns provided.

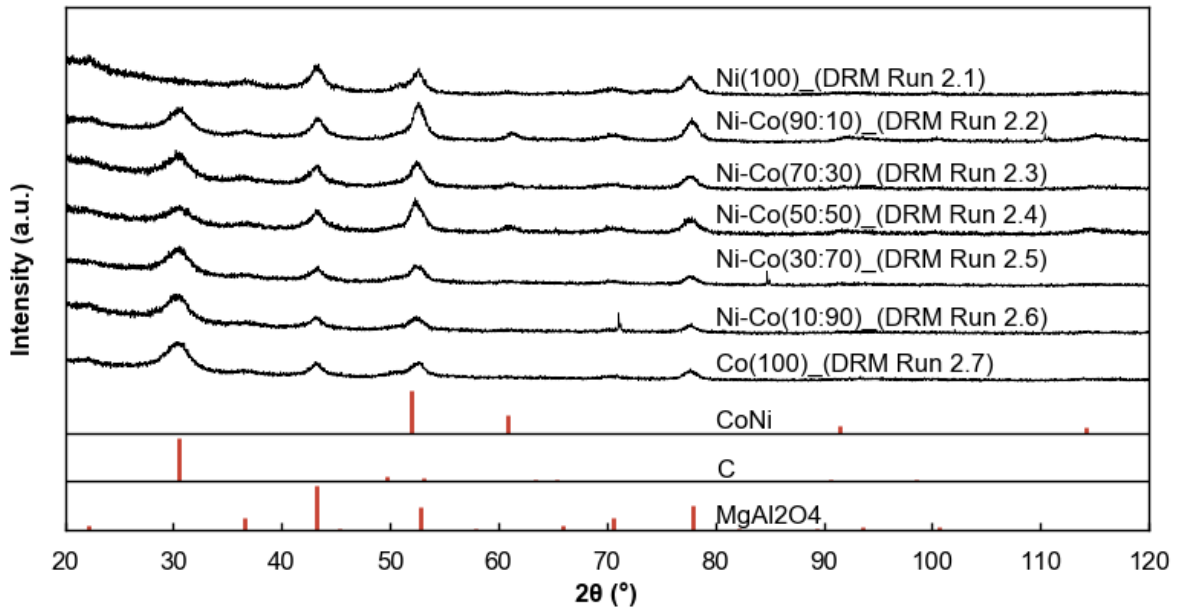

Figure 7.2: PXRD patterns obtained after the catalyst testing for DRM runs 2.1 – 2.7. Reference patterns for CoNi, C and $MgAl_2O_4$ are also provided in red.

7.2 Raman spectroscopy

The catalysts that were recovered from the second set of catalyst tests (DRM runs 2.1 – 2.7) were also analysed through Raman spectroscopy. This was conducted to gain insight regarding the nature of the carbon that was carbon deposited onto the catalyst surface during catalyst testing. The Raman spectra obtained for the catalysts are provided in Figure 7.3. According to Tuinstra & Koenig (1970), the Raman spectra of a single crystal of graphite which is perfectly crystalline would have a single peak at 1575 cm^{-1} (G band). However, when disorder is introduced to carbon, an additional peak is observed at 1355 cm^{-1} (D band). The presence of the D and G bands in Raman spectra are therefore generally used to determine the presence of carbon. Based on

this, the Raman spectra provided in Figure 7.3, show that there was carbon deposition on all the catalysts during catalyst testing with the exception of the Ni(100) sample.

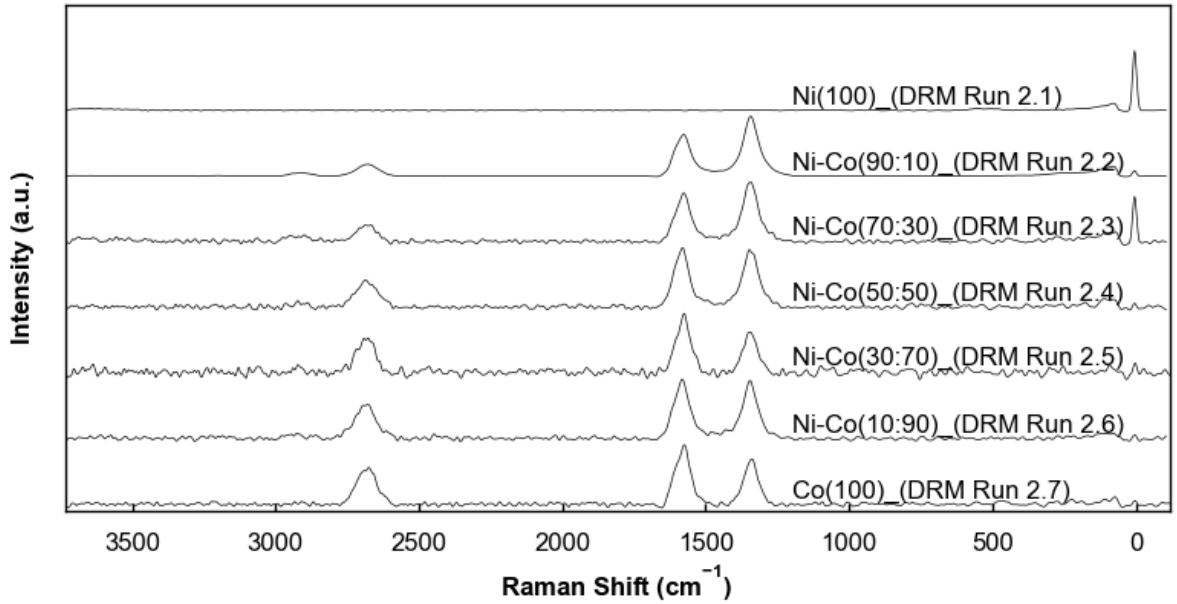

Figure 7.3: Raman spectra obtained for the catalysts recovered from DRM runs 2.1 – 2.7.

Additional information about the structure of carbon deposits on the catalysts was also obtained by further analysing the Raman spectra. According to Maher *et al.* (2013), the ratio of the intensity of the D to G band (I(D)/I(G)) can be used to determine how graphitic the carbon deposits are. A lower I(D)/I(G) value would for instance show that the carbon deposited is mostly graphitic as the G band would be more dominant. Furthermore, Maher *et al.* (2013) stated that the presence of a sharp 2D peak which occurs around 2700 cm^{-1} in conjunction with the presence of D and G bands provides an additional indicator that the carbon analysed is mostly graphitic in nature. In Figure 7.4, the relationship between the I(D)/I(G) band ratio and the Ni-Co composition of the catalysts from DRM runs 2.1 – 2.7 is provided. From Figure 7.4, it was observed that the I(D)/I(G) ratio decreases with increasing cobalt content in the catalyst. Based on the findings of Maher *et al.* (2013), this was an indication that the carbon deposits on the cobalt rich catalysts were more graphitic in comparison to their nickel rich counterparts. In addition, the 2D peaks in the Raman spectra of the cobalt rich catalysts in Figure 7.3 are more intense than those in the nickel rich catalysts. This provided further support for the case that the carbon deposits of the cobalt rich catalysts were more graphitic in nature compared to their nickel rich counterparts.

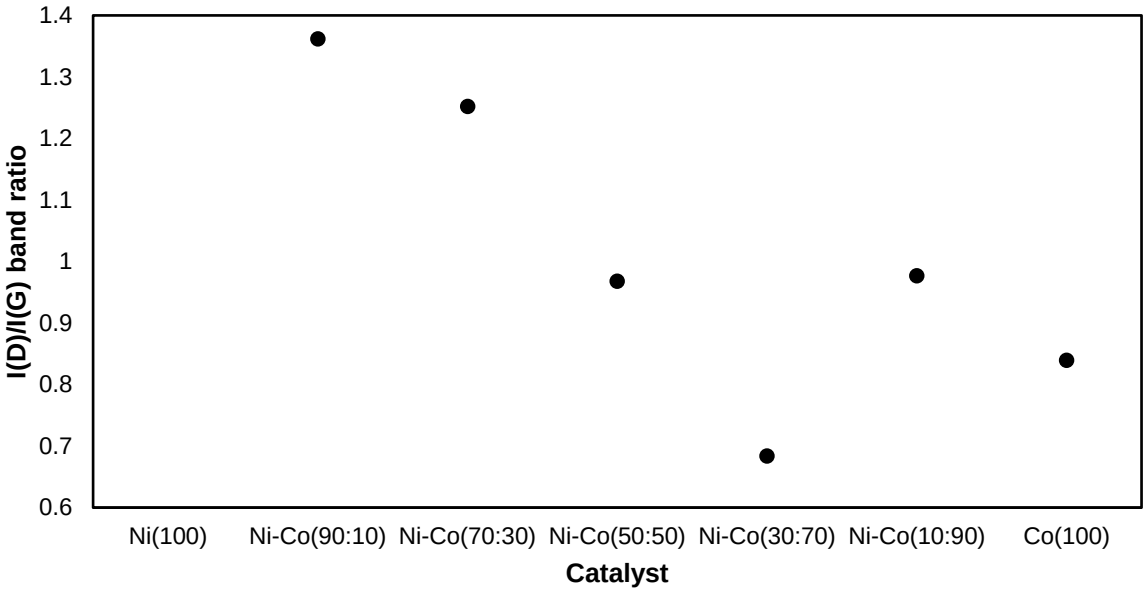

Figure 7.4: The relationship between the D to G band intensity ratio and the Ni-Co composition for the catalysts studied in DRM run 2.1 – 2.7.

7.3 Thermogravimetric analysis (TGA)

Thermogravimetric analysis (TGA) was carried out to quantify the amount of carbon deposited on the catalysts recovered from DRM runs 2.1 – 2.7. In the analysis, the temperature was ramped from room temperature to 1000 °C at a rate of 10 °C/minute in air. The TGA analysis profiles obtained for the Ni(100) and Co(100) catalysts are provided in Figure 7.5. From Figure 7.5, it was observed that both the Ni(100) and Co(100) had similar decreases in weight (%) at the start of the analysis. This initial decrease in weight (%) is generally associated with the evaporation of the moisture that was initially present on the catalyst surface at the start of the analysis. However, above 400 °C a second drastic decrease in weight (%) was observed for the Co(100) catalyst. This second loss in weight (%) occurs due to the reaction of the carbon deposits that were present on the catalyst with air to form CO_2. This second decrease in weight (%) was not observed on the Ni(100) catalyst because there were little to no carbon deposits on that catalyst. This finding agreed with the results from the PXRD and Raman analysis. The TGA profiles that were obtained for the rest of the catalysts not included in Figure 7.5, were similar to the profile obtained for the Co(100) sample. This is because there was carbon deposition on all those catalysts as well. The TGA profiles for these catalysts are provided in Figure 7.6.

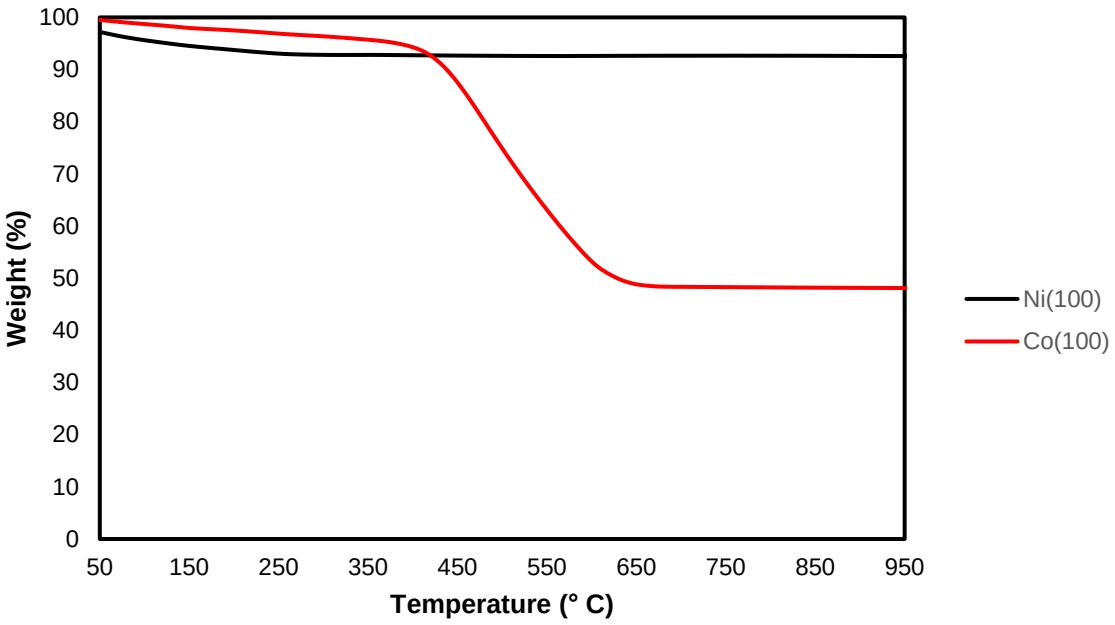

Figure 7.5: TGA analysis profiles results obtained for the Ni(100) and Co(100) catalyst samples in DRM runs 2.1 and 2.7 respectively

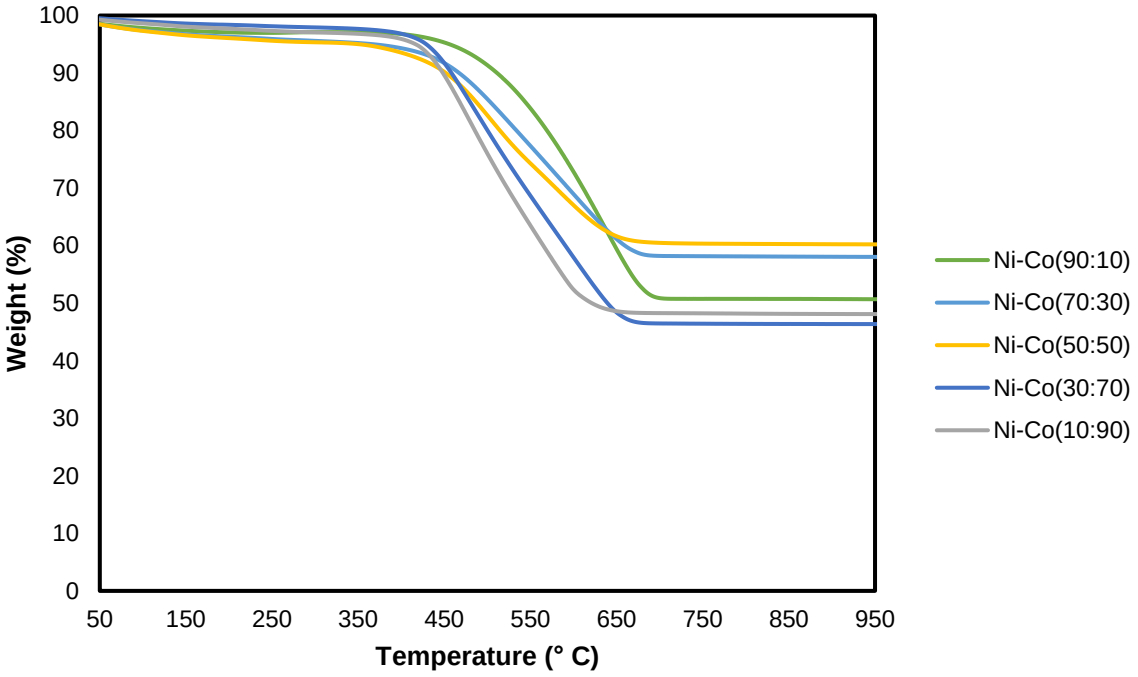

Figure 7.6: TGA analysis profiles results obtained for the Ni-Co(90:10), Ni-Co(70:30), Ni-Co(50:50), Ni-Co(30:70) and Ni-Co(10:90) catalyst samples in DRM runs 2.2 – 2.6

Differential thermogravimetry (DTG) profiles for all the catalysts analysed were obtained by determining the derivative of the TGA profiles. These are provided in Figure 7.7. From the profiles obtained, it was determined that the carbon deposited on the catalysts was oxidised between 350 – 750 °C because all the peaks on the DTG

profiles lie in this region. Additionally, the onset temperature for the oxidation of the carbon species was found to increase with increasing nickel content in the catalyst. Based on this finding, the carbon deposits on the nickel rich Ni-Co catalysts were more stable as they were oxidised at higher temperatures. Lastly, the DTG profiles of the cobalt rich Ni-Co catalysts were comprised of an initial peak around 450 °C and a shoulder peak above 550 °C. This finding suggests that there were two types of carbon with different stabilities deposited on the cobalt rich Ni-Co catalysts. Luisetto *et al.* (2012) reported similar findings in their work and attributed it to being a result of amorphous carbon being oxidised at a lower temperature (450 °C) and graphitic carbon being oxidised at higher temperature (650 °C). When compared to the Raman results, the results obtained from the DTG profiles are counterintuitive. This is because the carbon deposits on the cobalt rich catalysts were found to be more graphitic in nature, hence one would not expect the deposits to have a more amorphous carbon deposits as the DTG profiles would suggest.

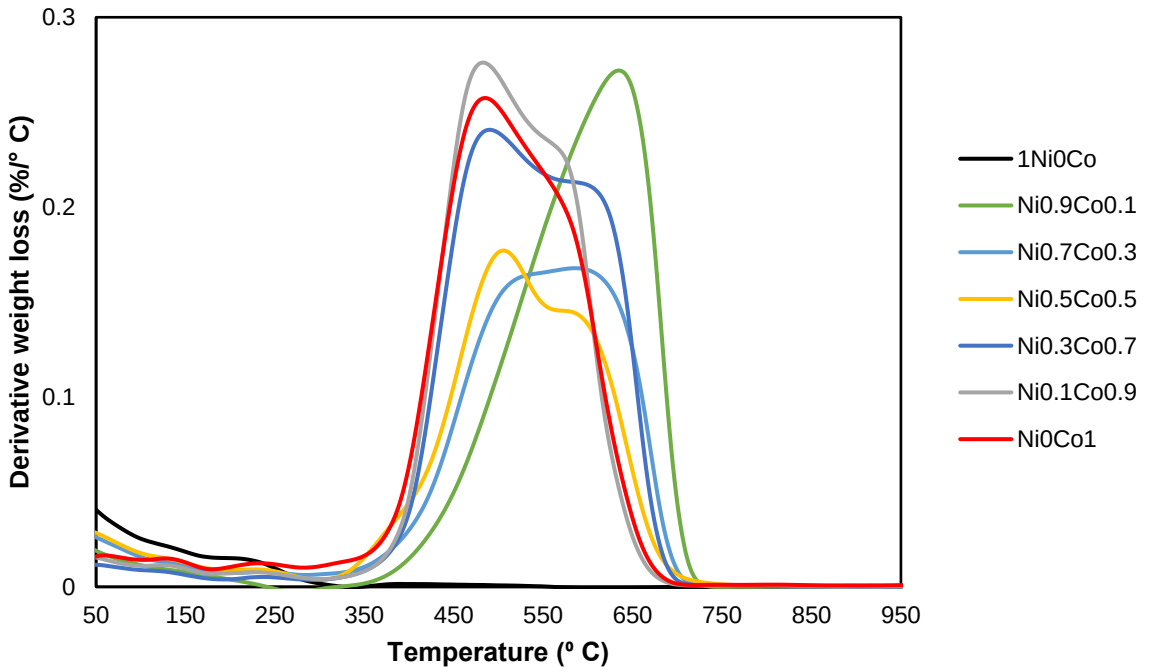

Figure 7.7: DTG profiles obtained for the Ni(100), Ni-Co(90:10), Ni-Co(70:30), Ni-Co(50:50), Ni-Co(30:70), Ni-Co(10:90) and Co(100) catalyst samples in DRM runs 2.1 – 2.7.

The %weight losses at the end of TGA analysis for the catalysts from DRM runs 2.1 – 2.7 were compared to determine whether there was a relationship between the amount of carbon deposited on the catalysts in and their Ni-Co composition. The

results of this comparison are provided in Figure 7.8. From Figure 7.8, it was determined that there is no clear correlation between the amount of carbon deposited on individual catalysts and their Ni-Co composition. This was because the %weight loss for all the catalysts, with the exception of the Ni(100) catalyst, were similar which indicated that the carbon deposits were similar as well. The Ni(100) catalyst had the lowest %weight loss because there was no significant carbon deposition on that catalyst.

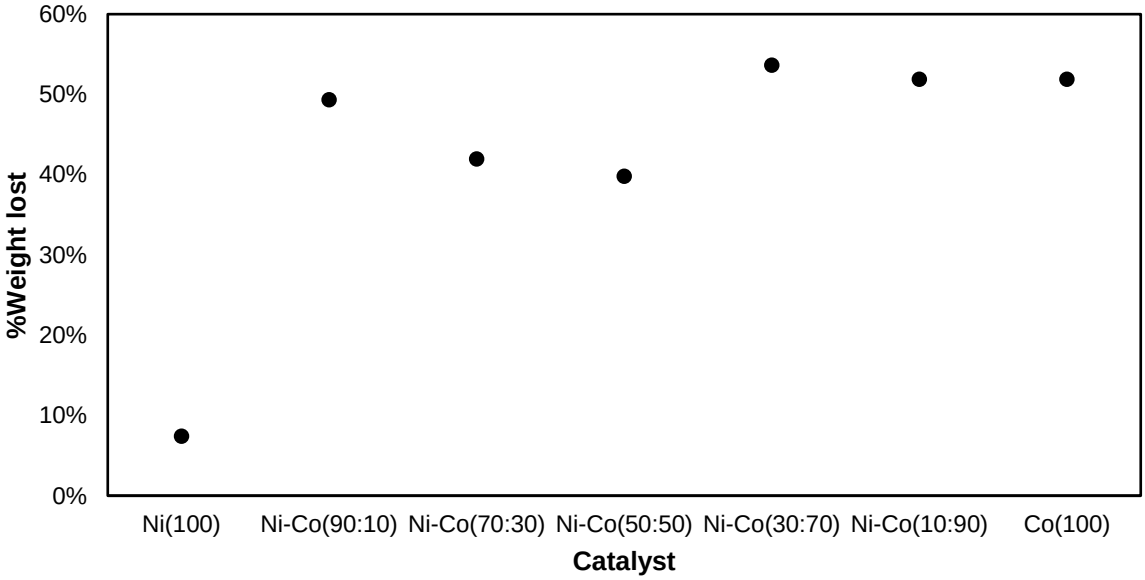

Figure 7.8: %weight loss observed for the catalysts recovered from DRM runs 2.1 - 2.7 at the end of TGA analysis that was carried out.

7.4 Transmission electron microscopy (TEM)

Transmission electron microscopy (TEM) was also used to analyse the catalysts recovered from DRM runs 2.1 – 2.7. TEM images obtained for the individual catalysts are provided in Figure 7.9. From Figure 7.9, there was carbon deposition on all the catalysts, with the exception of the Ni(100) catalyst given in image G. This was because carbon nanotubes were present in the TEM images for the Ni-Co bimetallic catalysts given in images B – F, whilst the Co(100) catalyst, given in image A, had sheets of carbon that covered extensive parts of the catalyst surface. The TEM image obtained for the Ni(100) catalyst given in image G did not provide any evidence for the formation of carbon as neither carbon nanotubes nor carbon sheets were observed in image G. Though carbon nanotubes were formed in all the bimetallic Ni-Co catalysts as shown in images B – F, it was noted that for cobalt rich Ni-Co samples (images B

– D) that some of these carbon nanotubes started at particles that were isolated and detached from the support. The detachment of the isolated particles from the support was most likely caused by the formation of carbon as there were no isolated particles in the TEM images of the fresh catalyst. This wasn't the case for the nickel rich samples (images E and F) where the carbon nanotubes grew from clusters of particles which were still supported and not detached. It also should be noted that the main differences between the images obtained for the fresh catalyst and spent catalyst was the presence of carbon.

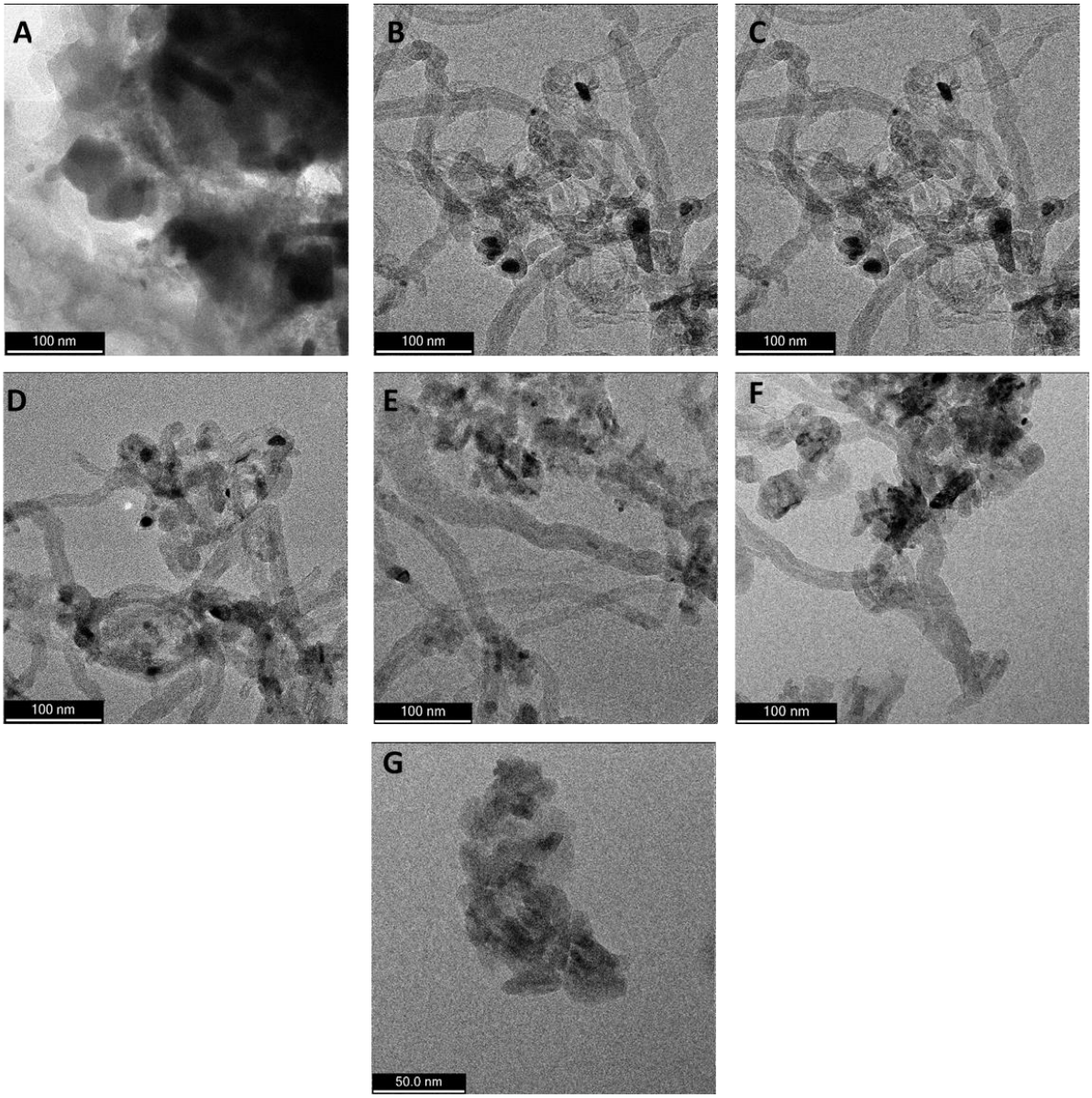

Figure 7.9: TEM images of catalysts recovered from DRM Runs 2.1 – 2.7: Co(100) – A, Ni-Co(10:90) – B, Ni-Co(30:70) – C, Ni-Co(50:50) – D, Ni-Co(70:30) – E, Ni-Co(90:10) – F and Ni(100) – G

7.5 Discussion linking physical characteristics of catalysts to performance

The characterisation of catalysts before and after catalyst testing is essential because it provides a way to link catalyst performance to the physical characteristics of the catalysts. From the final catalyst testing results (Section 6.2.2) in which the activity of all the catalysts in DRM was compared, the nickel rich Ni-Co catalysts (Ni-Co(70:30) and Ni-Co(90:10)) were found to be the most active catalysts. Post run characterisation of these catalysts using Raman (Section 7.2) and TGA (Section 7.3) showed that the carbon deposited on both these catalysts was different to the carbon deposited on the cobalt rich Ni-Co catalysts. The Raman results showed that the carbon deposits on the nickel rich Ni-Co catalysts were less graphitic in nature whilst the TGA results determined the carbon to be more stable. Additionally, TEM images (Section 7.4) of the cobalt rich Ni-Co catalysts showed that carbon formation on these catalysts in some cases caused Ni-Co particles to become detached from the support. Based on these findings, an argument can be made the difference in the carbon deposits between the nickel and cobalt rich Ni-Co catalysts were responsible for the different activities displayed by the catalysts.

The nickel rich Ni-Co catalysts were also found to be more stable than the cobalt rich Ni-Co catalysts as their relative losses in CO_2 and CH_4 conversions during catalyst testing were lower. A summary of these findings is available in Table 6.1. An argument can be made that the differences in stability were caused by the carbon deposits on the nickel rich and cobalt rich Ni-Co catalysts being different as was previously discussed. Additionally, it is also plausible that the detachment of Ni-Co particles from the support observed in TEM images (Section 7.4) of the cobalt rich Ni-Co catalysts also played a role in the catalysts being less stable. Overall, the impact of carbon deposition on the stability of the catalysts studied was less severe than had been anticipated. This is because carbon deposition has been found to significantly affect catalyst stability in previous studies. To illustrate this, Guo *et al.* (2004) reported that a 50% drop in CO_2 and CH_4 conversion in a period of 10 hours was observed for a nickel catalyst supported on γ-Al_2O_3 which had significant carbon deposits.

8 Conclusions

The objectives of the project were to investigate the suitability of nickel-cobalt (Ni-Co) alloy catalysts with different compositions as well as monometallic nickel and cobalt catalysts as dry reforming catalysts. In doing so, special emphasis was placed on understanding the effect of the Ni-Co composition on catalyst activity and stability.

For the study, seven catalysts with varying Ni-Co compositions were prepared namely: the Ni(100), Ni-Co(90:10), Ni-Co(70:30), Ni-Co(50:50), Ni-Co(30:70), Ni-Co(10:90) and Co(100) catalysts. When these catalysts were characterised using *in situ* PXRD, the reduction of the Co(100) and cobalt rich Ni-Co catalysts was found to go through the formation of an intermediate oxide phase. However, the Ni(100) and nickel rich Ni-Co catalysts did not follow this pattern as their reduction into the metallic phase did not involve the formation of an intermediate oxide phase. The results from the reduction studies carried out using H_2-TPR also provided further support for the notion that an intermediate oxide phase is formed during the reduction of the Co(100) and cobalt rich Ni-Co catalysts. This was because the main reduction peak for these catalysts during the H_2-TPR studies had a shoulder peak which indicated that two different phases were being reduced.

From the thermodynamic analysis that was carried at a pressure of 1.01325 bar and temperatures between 500 – 1000 °C, it was determined higher temperatures (preferably above 700 °C) were more favourable for the DRM reaction. This was because the side reactions that compete with the DRM reaction such as the methane cracking reaction and the RWGS reaction had a less pronounced impact on the observed thermodynamic behaviour at those temperatures. These findings were in line with those found in the literature.

Based on the findings from the thermodynamic analysis, preliminary catalyst testing was carried out at temperatures between 600 – 750 °C at atmospheric pressure. A CH_4:CO_2:Ar gas feed ratio of 1:1:2 at a space velocity of 160000 mL/g_{cat}-h was used. During preliminary catalyst testing, only the Ni-Co(90:10), Ni-Co(50:50) and Ni-Co(10:90) catalysts were used. The Ni-Co(90:10) and Ni-Co(50:50) catalysts showed great promise in terms of their long-term stability during catalyst testing at 750 °C and

700 °C. This was because they had minimal losses terms in activity after a total TOS of 36 hours between the two temperatures. The CO_2 conversion was also higher than the CH_4 conversion for all the catalysts tested during preliminary catalyst testing. This was attributed to the occurrence of the RWGS reaction.

Final catalyst testing was carried out at 700 °C and at atmospheric pressure for a TOS of 12 hours. A CH_4:CO_2:Ar gas feed ratio of 1:1:2 at a space velocity of 160000 mL/g_{cat}-h was used. The results from final catalyst testing determined that the Ni-Co(70:30) catalyst had the highest activity followed by the Ni-Co(90:10) catalyst. This led to the conclusion that the nickel rich Ni-Co catalysts were the most active catalysts prepared in the study. This finding showed that the Ni-Co composition had an influence on the catalyst activity attained during the dry reforming of methane. The Ni(100) catalyst had the lowest activity and was also the least stable during catalyst testing as it suffered significant losses in catalyst activity.

Post run catalyst characterisation using PXRD, Raman, TGA and TEM showed that there was carbon deposition during catalyst testing on all the catalysts tested except the Ni(100) catalyst. These results led to the conclusion that the lack of activity and stability displayed by the Ni(100) catalyst was not caused by carbon formation and must have been caused by a different catalyst deactivation mechanism. Since carbon formation played no role in the lack of activity by the catalyst, it is possible that the active metal could have been oxidised by the gas environment during reaction or that inactive metal support compounds such as nickel aluminate were formed during reaction as was the case in the studies carried out by Takanabe *et al.* (2005) and (Guo *et al.*, 2004). However, it is unlikely that nickel aluminate formed during the reaction because the $MgAl_2O_4$ support was chosen to prevent this from happening. With this in mind, the most plausible speculation was that the Ni(100) catalyst was deactivated through either sintering or the oxidation of the active metal caused by the gas environment during the reaction. However, both these speculations could not be verified based on the tests carried out during the study.

The activity and stability displayed by the rest of the catalysts during final catalyst testing showed that the impact of carbon formation on the activity of catalysts such as

the Ni-Co(70:30) and Ni-Co(90:10) was limited. However, the formation of carbon means that the catalysts would likely not be viable candidates for long-term use because it could cause reactor blockages as was experienced for the Ni-Co(10:90) during final catalyst testing. The detachment of metal particles from the support shown in the post-run TEM analysis of the cobalt rich Ni-Co catalysts was also worrying in this regard.

The Raman spectroscopy results showed that the Ni-Co composition of the catalysts influenced the type of carbon deposited on the catalysts during catalyst testing. This was because the carbon deposits on the cobalt rich catalysts were found to be more graphitic in nature compared to those on the nickel rich catalysts. However, the Ni-Co composition of the catalysts was found to have no influence on the amount of carbon deposited on the catalysts based on the results obtained from TGA analysis.

9 Recommendations for future work

Based on the work carried in this study, the following recommendations were made:

- The nickel rich bimetallic Ni-Co catalysts specifically the Ni-Co(70:30) and Ni-Co(90:10) were determined to be most active during catalyst testing. Therefore, it would be useful for future studies to concentrate on the nickel rich Ni-Co catalysts as that would help in determining the optimum Ni-Co composition for catalysts.
- Since there was carbon deposition on all the catalysts tested with the exception of the Ni(100) catalyst, alternate measures to combat the formation of carbon such as water co-feeding have to be explored. This is because limiting the formation of carbon would enhance the long-term stability of the catalysts during the dry reforming reaction.
- The use of the *in-situ* magnetometer to study the deactivation mechanisms of catalysts during the dry reforming of methane would help in providing additional insight especially in instances where the cause of deactivation cannot be determined through ex-situ characterisation techniques as was the case for the Ni(100) catalyst.

10 References

Abdullah, B., Abd Ghani, N.A. & Vo, D.-V.N. 2017. Recent advances in dry reforming of methane over Ni-based catalysts. *Journal of Cleaner Production.* 162:170-185. DOI:10.1016/j.jclepro.2017.05.176.

Abdulrasheed, A., Jalil, A.A., Gambo, Y., Ibrahim, M., Hambali, H.U. & Shahul Hamid, M.Y. 2019. A review on catalyst development for dry reforming of methane to syngas: Recent advances. *Renewable and Sustainable Energy Reviews.* 108:175-193. DOI:10.1016/j.rser.2019.03.054.

Aramouni, N.A.K., Zeaiter, J., Kwapinski, W. & Ahmad, M.N. 2017. Thermodynamic analysis of methane dry reforming: Effect of the catalyst particle size on carbon formation. *Energy Conversion and Management.* 150:614-622. DOI:10.1016/j.enconman.2017.08.056.

Aramouni, N.A.K., Touma, J.G., Tarboush, B.A., Zeaiter, J. & Ahmad, M.N. 2018. Catalyst design for dry reforming of methane: Analysis review. *Renewable and Sustainable Energy Reviews.* 82:2570-2585. DOI:10.1016/j.rser.2017.09.076.

Ay, H. & Üner, D. 2015. Dry reforming of methane over CeO_2 supported Ni, Co and Ni–Co catalysts. *Applied Catalysis B: Environmental.* 179:128-138. DOI:10.1016/j.apcatb.2015.05.013.

Bitter, J., Seshan, K. & Lercher, J. 1998. Mono and bifunctional pathways of CO_2/CH_4 reforming over Pt and Rh based catalysts. *Journal of Catalysis.* 176(1):93-101.

Bradford, M.C.J. & Vannice, M.A. 1999. CO_2 Reforming of CH_4. *Catalysis Reviews.* 41(1):1-42. DOI:10.1081/CR-100101948.

Budiman, A.W., Song, S.-H., Chang, T.-S., Shin, C.-H. & Choi, M.-J. 2012. Dry Reforming of Methane Over Cobalt Catalysts: A Literature Review of Catalyst Development. *Catalysis Surveys from Asia.* 16(4):183-197. DOI:10.1007/s10563-012-9143-2.

Claeys, M. & Fischer, N. 2013. *PCT Patent WO 2013/005180 A1.*

Claeys, M., Van Steen, E., Visagie, J. & Van de Loosdretch, J. 2010. *PCT Patent WO 2010/004419 A2.*

Claeys, M., Dry, M.E., van Steen, E., du Plessis, E., van Berge, P.J., Saib, A.M. & Moodley, D.J. 2014. In situ magnetometer study on the formation and stability of cobalt carbide in Fischer–Tropsch synthesis. *Journal of Catalysis.* 318:193-202. DOI:10.1016/j.jcat.2014.08.002.

Claeys, M., Dry, M.E., van Steen, E., van Berge, P.J., Booyens, S., Crous, R., van Helden, P., Labuschagne, J. et al. 2015. Impact of Process Conditions on the Sintering Behavior of an Alumina-Supported Cobalt Fischer–Tropsch Catalyst Studied with an in Situ Magnetometer. *ACS Catalysis.* 5(2):841-852. DOI:10.1021/cs501810y.

Clapham, B. 2012. The Development of an In-Situ X-Ray Diffraction Cell for Fischer-Tropsch Catalyst Characterisation. MSc Thesis University of Cape Town.

Dalmon, J.-A. 1994. Magnetic measurements and catalysis. In *Catalyst Characterization: Physical Techniques for Solid Materials.* B. Imelik and J.C. Vedrine, Eds. New York: Plenum Press. 585-609.

Das, S., Sengupta, M., Patel, J. & Bordoloi, A. 2017. A study of the synergy between support surface properties and catalyst deactivation for CO_2 reforming over supported Ni nanoparticles. *Applied Catalysis A: General.* 545:113-126. DOI:10.1016/j.apcata.2017.07.044.

Djinović, P., Batista, J. & Pintar, A. 2012. Efficient catalytic abatement of greenhouse gases: Methane reforming with CO_2 using a novel and thermally stable Rh–CeO_2 catalyst. *International Journal of Hydrogen Energy.* 37(3):2699-2707. DOI:10.1016/j.ijhydene.2011.10.107.

Elliott, J.R. & Lira, C.T. 2012. *Introductory chemical engineering thermodynamics.* Prentice Hall Upper Saddle River, NJ.

Fan, M.-S., Abdullah, A.Z. & Bhatia, S. 2009. Catalytic Technology for Carbon Dioxide Reforming of Methane to Synthesis Gas. *ChemCatChem.* 1(2):192-208. DOI:10.1002/cctc.200900025.

Ferreira-Aparicio, P., Rodrıguez-Ramos, I., Anderson, J. & Guerrero-Ruiz, A. 2000. Mechanistic aspects of the dry reforming of methane over ruthenium catalysts. *Applied Catalysis A: General.* 202(2):183-196.

Fischer, N., Clapham, B., Feltes, T., van Steen, E. & Claeys, M. 2014. Size-dependent phase transformation of catalytically active nanoparticles captured in situ. *Angew Chem Int Ed Engl.* 53(5):1342-1345. DOI:10.1002/anie.201306899.

Gao, X., Tan, Z., Hidajat, K. & Kawi, S. 2017. Highly reactive Ni-Co/SiO_2 bimetallic catalyst via complexation with oleylamine/oleic acid organic pair for dry reforming of methane. *Catalysis Today.* 281:250-258. DOI:10.1016/j.cattod.2016.07.013.

García-Diéguez, M., Pieta, I.S., Herrera, M.C., Larrubia, M.A. & Alemany, L.J. 2011. RhNi nanocatalysts for the CO_2 and CO_2+H_2O reforming of methane. *Catalysis Today.* 172(1):136-142. DOI:10.1016/j.cattod.2011.02.012.

Gerosa, M., Bottani, C.E., Caramella, L., Onida, G., Di Valentin, C. & Pacchioni, G. 2015. Defect calculations in semiconductors through a dielectric-dependent hybrid DFT functional: The case of oxygen vacancies in metal oxides. *J Chem Phys.* 143(13):134702. DOI:10.1063/1.4931805.

Guo, J., Lou, H., Zhao, H., Chai, D. & Zheng, X. 2004. Dry reforming of methane over nickel catalysts supported on magnesium aluminate spinels. *Applied Catalysis A: General.* 273(1-2):75-82. DOI:10.1016/j.apcata.2004.06.014.

Horlyck, J., Lawrey, C., Lovell, E.C., Amal, R. & Scott, J. 2018. Elucidating the impact of Ni and Co loading on the selectivity of bimetallic NiCo catalysts for dry reforming of

methane. *Chemical Engineering Journal.* 352:572-580. DOI:10.1016/j.cej.2018.07.009.

Hou, Z. & Yashima, T. 2003. Small amounts of Rh-promoted Ni catalysts for methane reforming with CO 2. *Catalysis Letters.* 89(3):193-197.

Hou, Z., Chen, P., Fang, H., Zheng, X. & Yashima, T. 2006. Production of synthesis gas via methane reforming with CO_2 on noble metals and small amount of noble-(Rh-) promoted Ni catalysts. *International Journal of Hydrogen Energy.* 31(5):555-561. DOI:10.1016/j.ijhydene.2005.06.010.

Istadi, I., Amin, N.A.S. & Aishah, N. 2005. Co-generation of C2 hydrocarbons and synthesis gases from methane and carbon dioxide: a thermodynamic analysis. *J. Nat. Gas Chem.* 14:140-150.

Jang, W.-J., Shim, J.-O., Kim, H.-M., Yoo, S.-Y. & Roh, H.-S. 2019. A review on dry reforming of methane in aspect of catalytic properties. *Catalysis Today.* 324:15-26. DOI:10.1016/j.cattod.2018.07.032.

Kittel, C. 2005. *Introduction to solid state physics.* 8th. Hoboken, NJ: Wiley.

Laosiripojana, N. & Assabumrungrat, S. 2005. Catalytic dry reforming of methane over high surface area ceria. *Applied Catalysis B: Environmental.* 60(1-2):107-116.

Leger, J.M., Loriers-Susse, C. & Vodar, B. 1972. Pressure Effect on the Curie Temperatures of Transition Metals and Alloys. *Physical Review B.* 6(11):4250-4261. DOI:10.1103/PhysRevB.6.4250.

Linde. 2019. *Synergized benefits of Linde DRYREF™ and BASF SYNSPIRE™*. Available: https://www.engineering.linde.com/l/310981/2020-01-29/j5nl5z/310981/94841/Linde_DRYREF_BASF_SYNSPIRE_brochure_2019.pdf [Available: https://www.engineering.linde.com/l/310981/2020-01-29/j5nl5z/310981/94841/Linde_DRYREF_BASF_SYNSPIRE_brochure_2019.pdf].

Luisetto, I., Tuti, S. & Di Bartolomeo, E. 2012. Co and Ni supported on CeO_2 as selective bimetallic catalyst for dry reforming of methane. *International Journal of Hydrogen Energy.* 37(21):15992-15999. DOI:10.1016/j.ijhydene.2012.08.006.

Maher, R.C., Duboviks, V., Offer, G.J., Kishimoto, M., Brandon, N.P. & Cohen, L.F. 2013. Raman Spectroscopy of Solid Oxide Fuel Cells: Technique Overview and Application to Carbon Deposition Analysis. *Fuel Cells.* 13(4):455-469. DOI:10.1002/fuce.201200173.

Mohn, P. & Wohlfarth, E. 1987. The Curie temperature of the ferromagnetic transition metals and their compounds. *Journal of Physics F: Metal Physics.* 17(12):2421-2430. DOI:10.1088/0305-4608/17/12/016.

Mortensen, P.M., Rautenbach, M. & Stenseng, M. 2020. *CO_2 reforming – the smart way Haldor Topsoe White paper.*

Moulijn, J.A., Van Diepen, A. & Kapteijn, F. 2001. Catalyst deactivation: is it predictable?: What to do? *Applied Catalysis A: General.* 212(1-2):3-16.

Nagaoka, K., Takanabe, K. & Aika, K. 2004. Modification of Co/TiO_2 for dry reforming of methane at 2MPa by Pt, Ru or Ni. *Applied Catalysis A: General.* 268(1-2):151-158. DOI:10.1016/j.apcata.2004.03.029.

Nematollahi, B., Rezaei, M., Lay, E.N. & Khajenoori, M. 2012. Thermodynamic analysis of combined reforming process using Gibbs energy minimization method: In view of solid carbon formation. *Journal of Natural Gas Chemistry.* 21(6):694-702. DOI:10.1016/s1003-9953(11)60421-0.

Nichizawa, T. & Ishida, K. 1983. The Co-Ni (Cobalt-Nickel) System. *Bulletin of Alloy Phase Diagrams.* 4(4):390-395.

Nikoo, M.K. & Amin, N.A.S. 2011. Thermodynamic analysis of carbon dioxide reforming of methane in view of solid carbon formation. *Fuel Processing Technology.* 92(3):678-691. DOI:10.1016/j.fuproc.2010.11.027.

Pakhare, D. & Spivey, J. 2014. A review of dry (CO_2) reforming of methane over noble metal catalysts. *Chem Soc Rev.* 43(22):7813-7837. DOI:10.1039/c3cs60395d.

Papadopoulou, C., Matralis, H. & Verykios, X. 2012. Utilization of biogas as a renewable carbon source: dry reforming of methane. In *Catalysis for alternative energy generation.* Springer. 57-127.

Pawelec, B., Damyanova, S., Arishtirova, K., Fierro, J.L.G. & Petrov, L. 2007. Structural and surface features of PtNi catalysts for reforming of methane with CO2. *Applied Catalysis A: General.* 323:188-201. DOI:10.1016/j.apcata.2007.02.017.

Phan, T.S., Sane, A.R., de Vasconcelos, B.R., Nzihou, A., Sharrock, P., Grouset, D. & Minh, D.P. 2018. Hydroxyapatite supported bimetallic cobalt and nickel catalysts for syngas production from dry reforming of methane. *Applied Catalysis B: Environmental.* 224:310-321.

Roh, H.-S., Jun, K.-W., Dong, W.-S., Park, S.-E. & Baek, Y.-S. 2001. Highly stable Ni catalyst supported on $Ce–ZrO_2$ for oxy-steam reforming of methane. *Catalysis Letters.* 74(1-2):31-36.

Rostrup-Nielsen, J. & Hansen, J.B. 1993. CO_2-reforming of methane over transition metals. *Journal of Catalysis.* 144(1):38-49.

San-José-Alonso, D., Juan-Juan, J., Illán-Gómez, M.J. & Román-Martínez, M.C. 2009. Ni, Co and bimetallic Ni–Co catalysts for the dry reforming of methane. *Applied Catalysis A: General.* 371(1-2):54-59. DOI:10.1016/j.apcata.2009.09.026.

Shamsi, A. & Johnson, C.D. 2003. Effect of pressure on the carbon deposition route in CO_2 reforming of $^{13}CH_4$. *Catalysis Today.* 84(1-2):17-25.

Steinhauer, B., Kasireddy, M.R., Radnik, J. & Martin, A. 2009. Development of Ni-Pd bimetallic catalysts for the utilization of carbon dioxide and methane by dry reforming. *Applied Catalysis A: General.* 366(2):333-341. DOI:10.1016/j.apcata.2009.07.021.

Sun, Y., Li, C., Djerdj, I., Khalid, O., Cop, P., Sann, J., Weber, T., Werner, S. et al. 2019. Oxygen storage capacity versus catalytic activity of ceria–zirconia solid

solutions in CO and HCl oxidation. *Catalysis Science & Technology.* 9(9):2163-2172. DOI:10.1039/c9cy00222g.

Takanabe, K., Nagaoka, K., Nariai, K. & Aika, K. 2005. Titania-supported cobalt and nickel bimetallic catalysts for carbon dioxide reforming of methane. *Journal of Catalysis.* 232(2):268-275. DOI:10.1016/j.jcat.2005.03.011.

Tuinstra, F. & Koenig, J.L. 1970. Raman Spectrum of Graphite. *The Journal of Chemical Physics.* 53(3):1126-1130. DOI:10.1063/1.1674108.

van Helden, P., Prinsloo, F., van den Berg, J.-A., Xaba, B., Erasmus, W., Claeys, M. & van de Loosdrecht, J. 2020. Cobalt-nickel bimetallic Fischer-Tropsch catalysts: A combined theoretical and experimental approach. *Catalysis Today.* 342:88-98. DOI:10.1016/j.cattod.2019.03.001.

Wang, F., Xu, L., Yang, J., Zhang, J., Zhang, L., Li, H., Zhao, Y., Li, H.X. et al. 2017. Enhanced catalytic performance of Ir catalysts supported on ceria-based solid solutions for methane dry reforming reaction. *Catalysis Today.* 281:295-303. DOI:10.1016/j.cattod.2016.03.055.

Wang, S., Lu, G. & Millar, G.J. 1996. Carbon dioxide reforming of methane to produce synthesis gas over metal-supported catalysts: state of the art. *Energy & fuels.* 10(4):896-904.

Wittich, K., Krämer, M., Bottke, N. & Schunk, S.A. 2020. Catalytic Dry Reforming of Methane: Insights from Model Systems. *ChemCatChem.* 10.1002/cctc.201902142. DOI:10.1002/cctc.201902142.

Zhang, J., Wang, H. & Dalai, A.K. 2007. Development of stable bimetallic catalysts for carbon dioxide reforming of methane. *Journal of Catalysis.* 249(2):300-310. DOI:10.1016/j.jcat.2007.05.004.

Zhang, R.-j., Xia, G.-f., Li, M.-f., Wu, Y., Nie, H. & Li, D.-d. 2015. Effect of support on the performance of Ni-based catalyst in methane dry reforming. *Journal of Fuel Chemistry and Technology.* 43(11):1359-1365. DOI:10.1016/s1872-5813(15)30040-2.

11 Appendices

11.1 Appendix A

Table 11.1: TCD calibration

Gas mixture component	Concentration (%)	Peak area 1	Peak area 2	Peak area 3	Average peak area	F_{Ar}
Ar	9.9	1221	1221	1222	1221	1.00
N_2	5.8					
CH_4	15.9	1339	1339	1339	1339	0.68
CO	18.5	1791	1789	1791	1790	0.78
CO_2	10.1	2140	2142	2141	2141	1.72
H_2	39.8	36736	36817	36813	36789	7.49

11.2 Appendix B

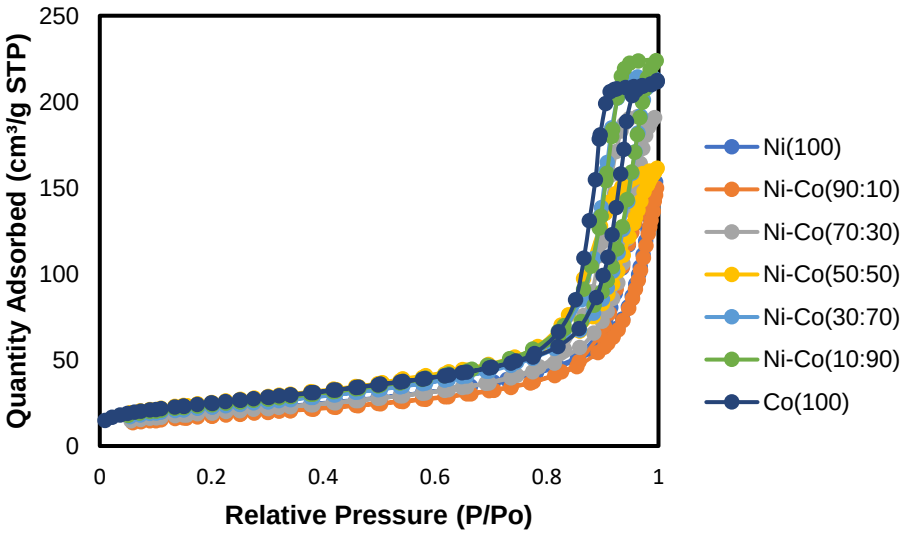

Figure 11.1: Nitrogen adsorption-desorption isotherms for the catalysts studied

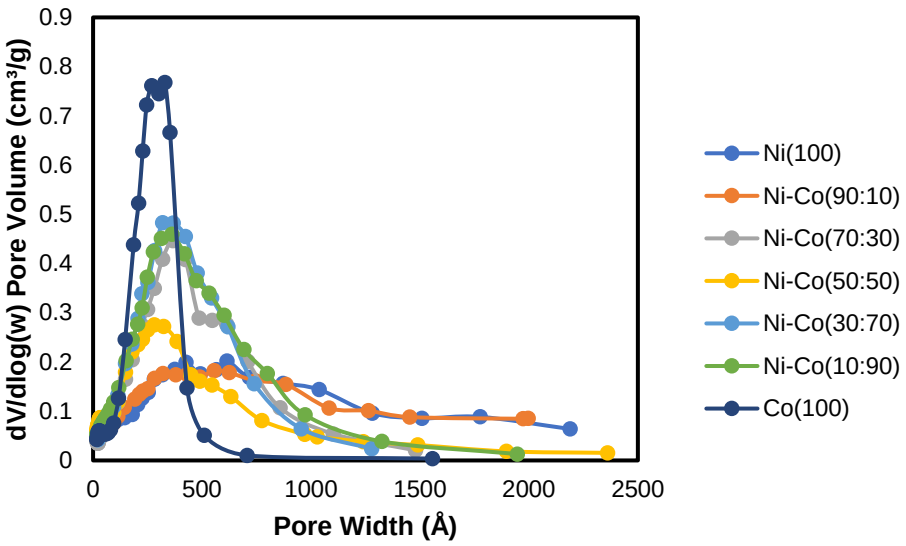

Figure 11.2: Pore size distribution for the catalysts studied

11.3 Appendix C

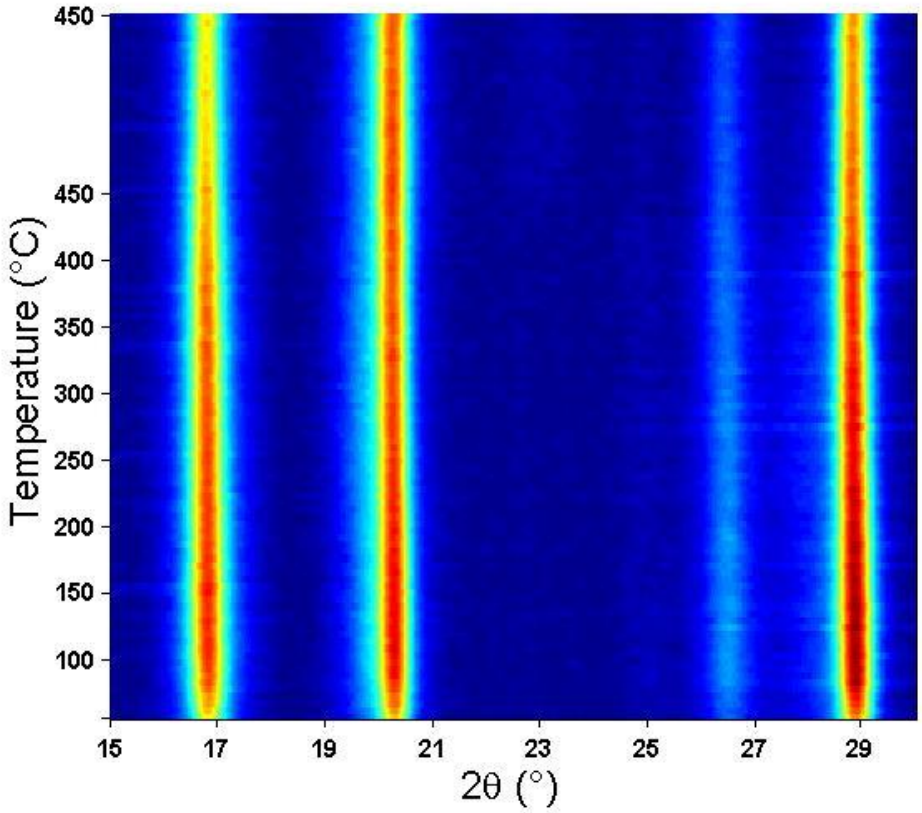

Figure 11.3: On top view of the in situ PXRD patterns obtained during the reduction of the Ni-Co(90:10) catalyst

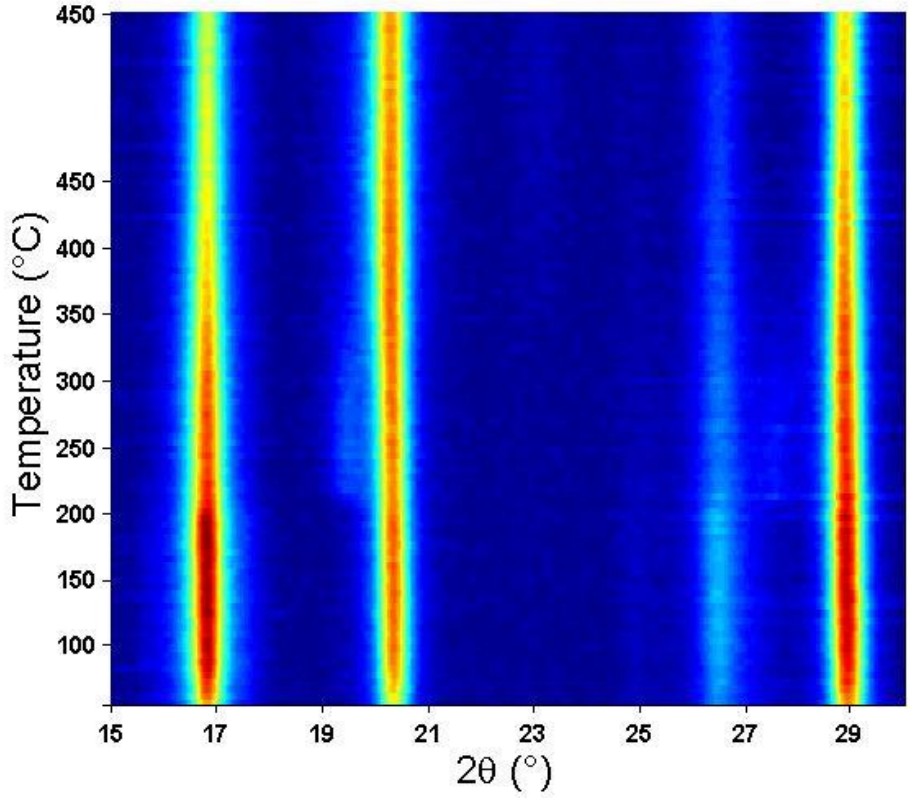

Figure 11.4: On top view of the in situ PXRD patterns obtained during the reduction of the Ni-Co(70:30) catalyst

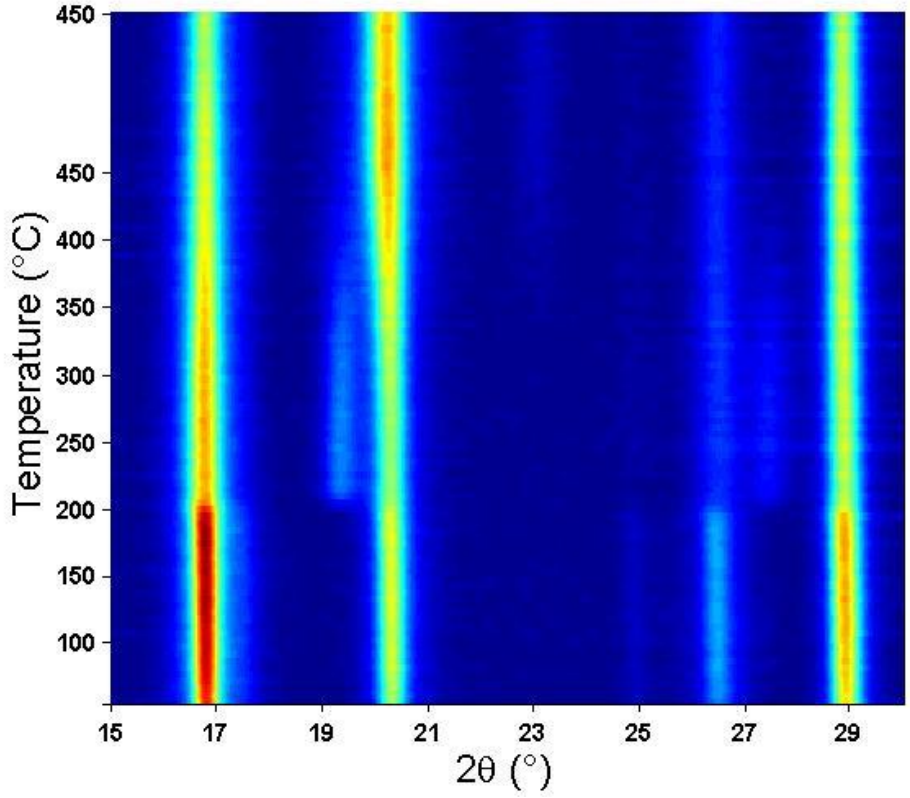

Figure 11.5: On top view of the in situ PXRD patterns obtained during the reduction of the Ni-Co(50:50) catalyst

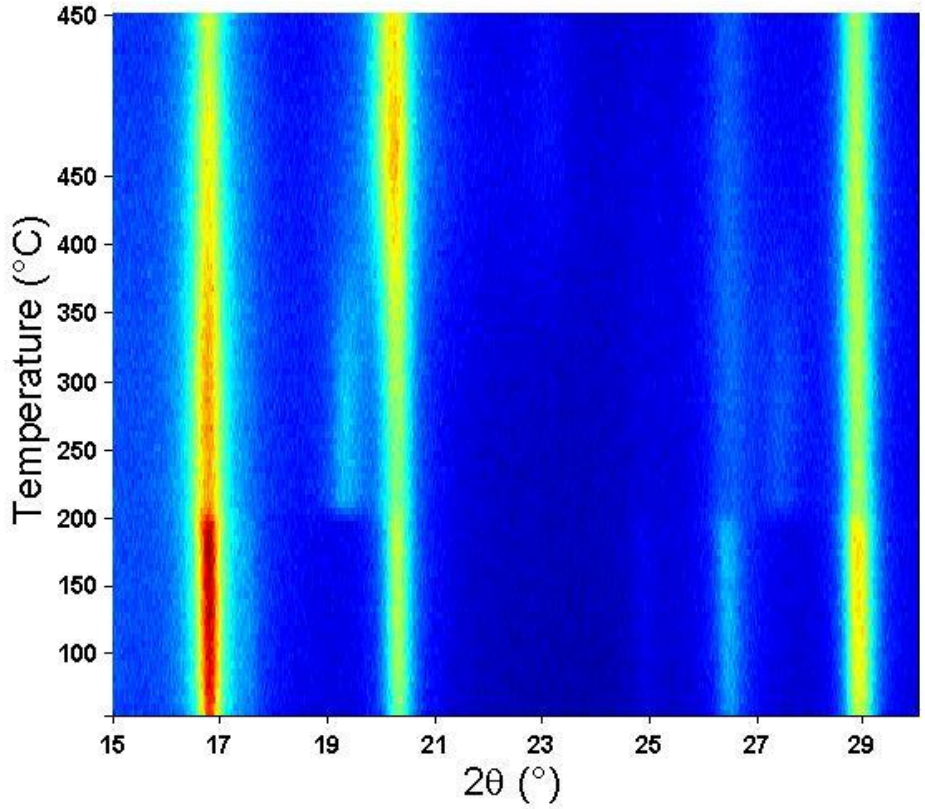

Figure 11.6: On top view of the in situ PXRD patterns obtained during the reduction of the Ni-Co(30:70) catalyst

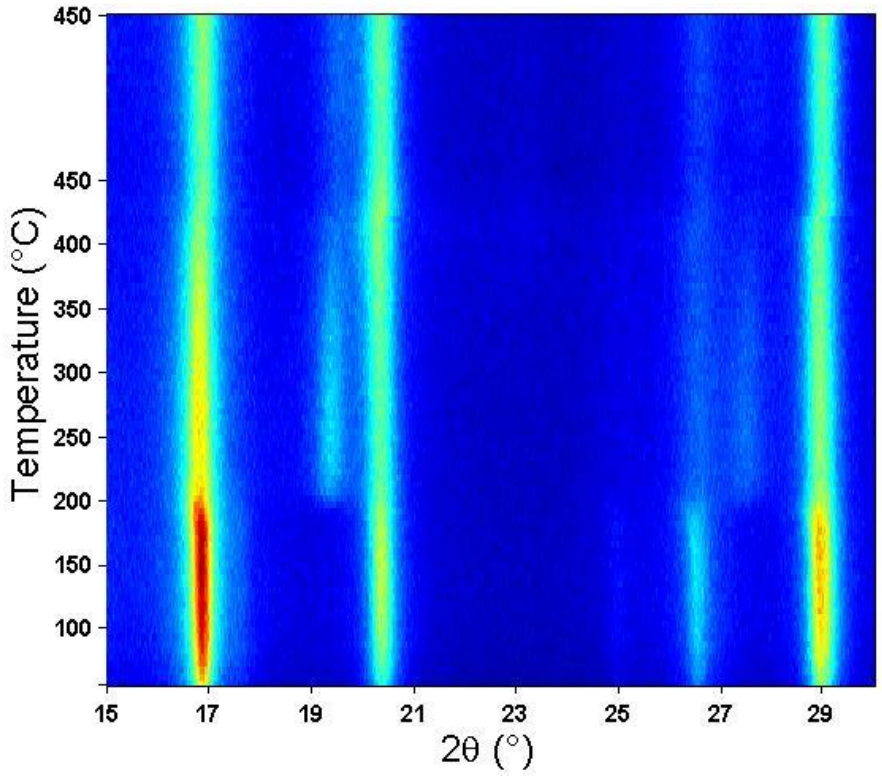

Figure 11.7: On top view of the in situ PXRD patterns obtained during the reduction of the Ni-Co(10:90) catalyst

11.4 Appendix D

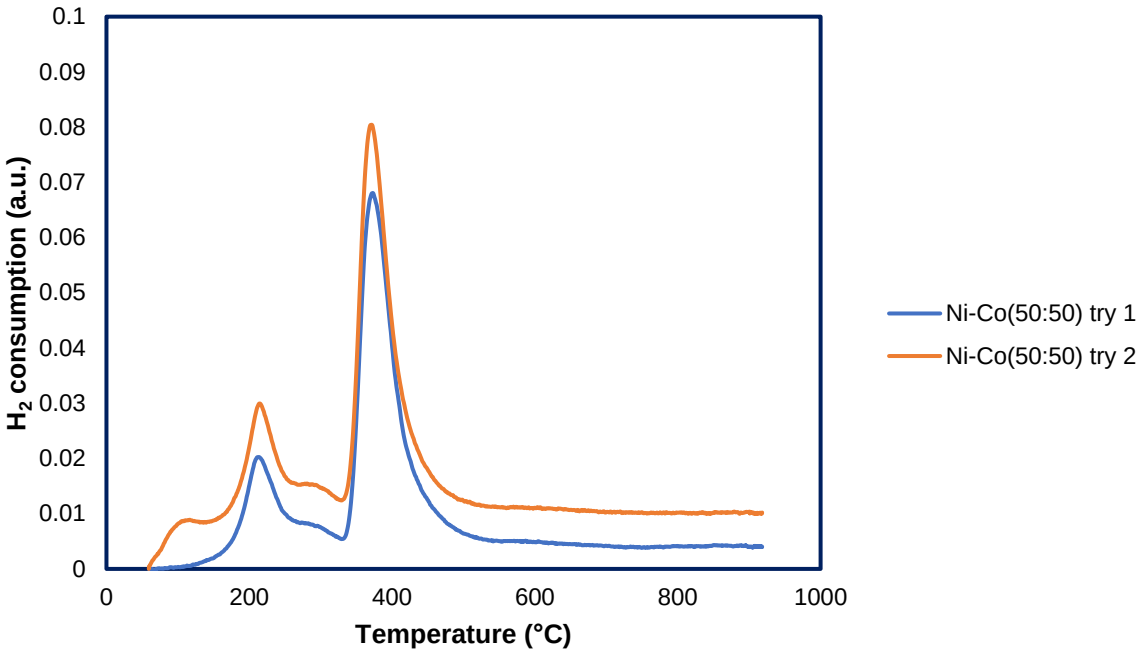

Figure 11.8: H_2-TPR results for the reduction for all the catalysts prepared